The Dynamics of Flocculated Dispersions

Thesis by

Yvette Valencia Baxter-Drayton

In Partial Fulfillment of the Requirements
for the Degree of
Doctor of Philosophy

California Institute of Technology
Pasadena California

1997
(Defended August 13, 1996)

To my mother, Gloria Baxter,

and

in loving memory of my father, Bertel Baxter.

ACKNOWLEDGEMENTS

For me this thesis is more than five years worth of work at Caltech. It is a milestone in my educational and personal development, and for this I am indebted to many people.

I was very fortunate to have an excellent teacher and academic advisor in Prof. John F. Brady. I am thankful for his encouragement and guidance as I found my way through my research. John's enthusiasm for science was often contagious, and our discussions have served to broaden my own thinking. Thanks to the members of my thesis committee, Professors George Gavalas, Julia Kornfield, and Zhen-Gang Wang for their interest in me and in my work. I also benefited from helpful discussions with Prof. Masao Doi. For financial support while at Caltech, I thank the National Science Foundation and the Kodak Corporation.

Along the way to Caltech I've had a succession of great teachers. Deserving special mention are Mrs. Kelly and Mrs. Royce at Wolmers High, who were instrumental in cultivating my early interest in math and science, and Prof. Edward Merrill and Deborah Savage at MIT, who inspired and encouraged me to pursue a graduate degree in Chemical Engineering.

My fellow Brady bunch members, past and present, Thanh, Phil, Jeff, Prabu, Merzhad, Douglas, Yevgeny, Mike, Dave, and Saud have helped pass numerous long days and occasional nights in the office. The current generation is thanked for weekly lunch time entertainment at the Athenaeum. I am grateful to Thanh for introducing me to simulation techniques, Prabu for help with making videos, Jeff for helpful

discussions on suspension dynamics, and Douglas for many helpful discussions on physics, differential equations, and life in general, not necessarily in that order.

Thanks to my friends who have enriched my life over the past five years in many ways; in particular, Neil for, among other things, bringing Paul up from down under and our RDC escapades, Pat, Dave, Moira, Lisa, and Mike for great dinners and conversation, my squash partner Edye, and Nancy for bringing a distinct and very welcome non-technical flavour to my Caltech experience. J.P's help in the first term at Caltech was invaluable.

I could write a million thanks to my parents and it would still not be enough; they have not only sacrificed a lot to put me through the best educational institutions, but have taught me how to truly get the most out of it. Their unfaltering love, support, and confidence in me have carried me a long way. I also thank my brother Desmond and sisters Prudence, Moveta, and Sophia for their continual encouragement, and for setting wonderful examples for me through their own achievements.

Finally, this thesis would not have been written if not for the love and constant support of my husband, Paul. I look forward to many happy adventures of the Drs. Drayton.

ABSTRACT

The rheological behavior of Brownian electrorheological (ER) fluids is studied as a model for flocculated colloidal dispersions. The ER fluid has the advantages that the interparticle potential energy can be varied by simply changing the applied field strength, and the microstructure consists of essentially linear chains of particles aligned with the field direction. Studies of the quiescent suspension structure find a dispersed region, an equilibrium flocculated region, and a kinetically flocculated region for low, moderate, and large attractive potential well depths, U_{min}/kT, respectively. Under simple shear flow, the suspension has a high-shear-rate Newtonian viscosity and a shear thinning viscosity at lower shear rates. For moderate attractive potential well depths the suspension has a low-shear viscosity that scales as $\exp(U_{min}/kT)$. Furthermore, the low-shear limiting behavior is seen at shear rates that scale as $\exp(-U_{min}/kT)$. The first normal stress difference is also presented. It was found that due to the electric field the suspension structure is anisotropic with respect to the compressional axis, and the first normal stress difference does not decay with the shear rate as it does for Brownian hard-spheres, but approaches a low-shear limiting value.

A theory is proposed that makes use of the time scale of diffusion for aggregated particles out of their mutual potential well, $\tau \sim (a^2/D)(kT/U_{min})\exp(U_{min}/kT)$, much in the spirit of the Eyring theory, to describe the rheology of the flocculated dispersion. Here a is the particle radius and D is the diffusivity of an isolated particle. When the shear rate is non-dimensionalized by τ, the reduced viscosity data for all

field strengths collapse onto a single universal curve. Although we use a relatively small monolayer suspension, our simulation results compare well to the limited experimental and theoretical work on Brownian ER suspensions. The scaling relationship for the low-shear viscosity has also been evidenced in other studies of flocculated dispersions.

The model is tested for its general applicability by a study of the rheology of a three-dimensional flocculated dispersion with an isotropic potential by molecular dynamics simulation and by analysis of experimental data obtained independently by Buscall, McGowan & Morton-Jones for a depletion flocculated dispersion. In both cases the suspension has a low-shear viscosity that scales exponentially with the pair potential well depth, and the low-shear limiting behavior was observed at a shear rate that scales inverse exponentially with the pair potential well depth, U_{min}/kT. The reduced viscosity data collapse onto a single curve when plotted as a function of the shear rate non-dimensionalized by the escape time scale, and the model was found to predict the reduced curves.

Contents

List of Figures

List of Tables

Chapter 1

Introduction

Aggregating colloidal suspensions exhibit a wide range of rheological behavior from thick gels to thin pastes. As with Brownian hard-sphere suspensions, the solids concentration plays an important role in the suspension dynamics, but in addition, the nature and strength of the particle interaction forces add a crucial dimension. Aggregation is generally referred to as a non-equilibrium process that converts individually dispersed particles into a disordered solid. The disordered solid can be either a flocculated suspension consisting of highly porous, weakly aggregated flocs, or a coagulant where the flocs are more closely packed (Russel, Saville & Schowalter 1989). Aggregated suspensions are also delineated according to the strength of the attractive interaction potential between particles (Buscall, McGowan & Morton-Jones 1993). For example, suspensions that have an attractive particle potential well depth, U_{min}, greater than $5 - 10kT$ are said to be flocculated, while suspensions with $U_{min} \sim 1$ - $5kT$ undergo an equilibrium phase separation where the suspended particles rearrange by diffusion into the structure of lowest energy and are not classified as flocculated. This is not a clear distinction, however, since given enough time all suspensions should tend toward equilibrium. In this work, a flocculated or aggregated suspension is taken to be a suspension of particles that form a connected volume spanning network and includes so-called equilibrium phases as long as the resulting structure spans the suspension volume.

There are a wide variety of ways to induce flocculation. For example, depletion flocculation is achieved by adding a non-adsorbing polymer to a suspension of hard spheres. Polymer molecules are excluded from the region between a pair of particles by

steric effects. Generally, the osmotic pressure increases with polymer concentration, and integration of this normal force over the surface of a particle yields the net force on the particle. The associated decrease of polymer in the gap between two particles produces a lower osmotic pressure and an attractive force that can be represented as an interparticle potential (Russel, Saville & Schowalter 1989).

Regardless of the flocculation method, however, suspensions with similar particle interaction potentials behave similarly. Weakly aggregating suspensions ($5kT < U_{min} < 20kT$) exhibit non-Newtonian behavior; they typically have low- and high-shear-rate viscosities, and shear thin at intermediate shear rates (Buscall et al. 1993; Melrose & Heyes 1993). Suspensions with U_{min} well above $20kT$ also shear thin and have a high-shear-rate viscosity, but do not show a low-shear viscosity, at least over experimentally accessible scales (Buscall et al. 1982); they are Bingham plastics with an apparent dynamic yield stress. The rheology literature abounds with models for flocculated suspensions. Most are phenomenological and offer little insight into the underlying physics of the suspension dynamics (Tanner 1985). For example, the Bingham and Casson models often used to fit data for fluids that show an apparent yield stress are not predictive and do not apply to all flocculated suspensions. A basic microstructural approach incorporating the physics of particle interactions and dynamics is needed and is the focus of this work.

Since the dynamics of the flocculated dispersion are complex, study of idealized situations facilitates understanding key factors. In Chapter 2, the rheological behavior of Brownian Electrorheological fluids is studied as a model for flocculated colloidal

dispersions. The ER fluid has the advantages that the interparticle potential energy can be varied by simply changing the applied field strength, and the microstructure consists of essentially linear chains of particles aligned with the field direction. With this idealized model, the suspension dynamics can be studied as a function of the three forces at work in the ER suspension: polarization forces due to the applied electric field, Brownian forces due to thermal effects, and viscous forces due to the applied shear. Under simple shear flow, the suspension has a high-shear-rate Newtonian viscosity and a shear thinning viscosity at lower shear rates. For moderate attractive potential well depths, U_{min}/kT, the suspension has a low-shear viscosity that scales as $\exp(U_{min}/kT)$. Furthermore, the low-shear limiting behavior is seen at shear rates that scale as $\exp(-U_{min}/kT)$. A simple scaling argument is used to explain the low-shear-rate viscosity scaling. An escape time, first developed by Kramers (1940), is introduced that gives the time scale of escape from a potential well of depth U_{min}/kT with $U_{min} \gg kT$. A new dimensionless shear rate can be defined as the ratio of the escape time and the time scale of shear, and when the viscosity data obtained is re-plotted as a function of the new reduced shear rate, a single universal curve is obtained. Although there have been previous discussions on the escape time as it relates to weakly aggregated suspension dynamics (De Rooij et al. 1993, Potanin et al. 1995), this is the first work to scale the shear rate with the escape time to produce a universal curve for Electrorheological fluids and weakly flocculated suspensions in general.

In Chapter 3, a model is proposed that makes use of the time scale of diffusion

for aggregated particles out of their mutual potential well, $\tau \sim (a^2/D)(kT/U_{min})$ $\exp(U_{min}/kT)$, much in the spirit of the Eyring theory. Here a is the particle radius and D is the diffusivity of an isolated particle. The model not only predicts the low-shear-rate viscosity but also the suspension viscosity over a wide range of shear rates. The predicted equation for the suspension viscosity is seen to fit the universal curve found in Chapter 2 for ER fluids with one adjustable parameter.

In Chapter 4, the model is tested for its general applicability, first by using simulations with an isotropic attractive potential, and second by using experimental data from Buscall et al. (1993) for depletion flocculated suspensions at moderate concentrations. Again, the viscosity data can be reduced to a single curve by using the shear rate reduced by the escape time, and the predicted viscosity relation from the model presented in Chapter 3 holds.

Chapter 5 briefly summarizes the main points and suggests further areas to explore on this topic.

Chapter 2

Brownian Electrorheological fluids as a model for flocculated dispersions

2.1 Introduction

A wide variety of ways to induce flocculation are detailed in Russel, Saville & Schowalter's (1989) *Colloidal Dispersions*. Regardless of the flocculation method, however, suspensions with similar particle interaction potentials behave similarly. For this work we use a suspension of polarizable particles in a non-conducting dielectric liquid forming an Electrorheological (ER) fluid. Winslow (1949) first noted that an electric field across a suspension of cornstarch in water thickens the fluid and that the viscosity of the fluid scaled with the square of the applied electric field. Potential applications for these tunable viscosity fluids range from liquid shocks for magnetically levitated trains (Technology Edge 1992), to dampeners for buildings to protect against earthquakes (R. C. Ehrgott & S. F. Masri 1994). The key to the ER effect is the difference in the polarizability of the particles and the suspending fluid. Applying an electric field across the suspension induces particle dipoles, and there is a net attraction between particles whose surfaces are oppositely charged and a net repulsion between particles whose surfaces are similarly charged, resulting in particle chaining along the field direction. (A difference in electrical conductivity between particles and fluid can have an analogous effect in AC electric fields). This electrically induced structure is responsible for the increased viscosities noted in ER fluids. A completely analogous situation occurs in magnetorheological (MR) fluids, where the magnetic permeability mismatch between particles and fluid leads to the same phenomena (Bossis et al. 1990).

In its simplest form, the ER pair potential is the sum of the attractive electrostatic

potential and a hard-sphere repulsion:

$$\frac{u(r,\theta)}{kT} = \left\{ \begin{array}{ll} \infty & \text{if } r < 2a \\ -\lambda \left(\frac{2a}{r}\right)^3 \frac{3\ \cos^2\theta - 1}{2} & \text{if } r > 2a \end{array} \right\},$$

where $\lambda \equiv \pi\epsilon a^3(\beta\mathcal{E})^2/kT$. Here θ is the angle between the electric field vector and the vector connecting two particle centers, $r = 2a$ is contact between the particles of radii a, and ϵ is the dielectric constant of the fluid, $\mathcal{E}$ is the magnitude of the electric field, and $\beta \equiv (\epsilon_p - \epsilon)/(\epsilon_p + 2\epsilon)$ measures the dielectric mismatch between fluid and particle. For point dipoles aligned along the field direction λ gives the potential well depth, U_{min}/kT.

The ER fluid structure and dynamics are governed by the interplay of polarization, thermal, and viscous forces due separately to the applied field, fluctuations of the solvent particles, and the imposed flow, respectively. The characteristic interparticle interaction forces for an ER fluid are:

Force	Scale
Thermal	kT/a
Polarization	$12\pi\epsilon a^2(\beta\mathcal{E})^2$
Viscous	$6\pi\eta a^2\dot{\gamma}$

where k is the Boltzmann constant, T is the temperature, η is the solvent viscosity, and $\dot{\gamma}$ is the magnitude of the shear rate. The relative importance of these forces are given by the dimensionless groups:

Group	Ratio	Scale
λ	polarization/thermal	$\pi\epsilon a^3(\beta\mathcal{E})^2/kT$
Pe	viscous/thermal	$6\pi\eta a^3\dot{\gamma}/kT$
Ma	viscous/polarization	$\eta\dot{\gamma}/2\epsilon\,(\beta\mathcal{E})^2$

defining the Peclet, Pe, and Mason, Ma, numbers. Note that the Peclet and Mason numbers are not independent; their ratio is simply 12λ. We shall discuss the suspension behavior primarily in terms of Ma and λ.

The nature of the static, non-sheared, structure of an ER fluid varies with λ, the relative strengths of the polarization and Brownian forces. Brownian forces tend to disrupt the chaining effect of the electric field, and when dominant, disperse the suspended particles. As Brownian motion becomes less important – as λ increases – the attractive electrostatic forces form chains aligned along the electric field direction. Thus, by simply changing the applied field strength, an ER fluid can be a disordered suspension, a flocculated suspension, or a solid. In short, the relatively simple structure and the ease with which its pair potential can be manipulated makes the ER fluid an ideal model for studies on flocculated suspensions.

The interplay of polarization, viscous, and Brownian forces gives rise to a wide variety of rheological behavior in ER fluids. At moderate volume fraction and at large λ, shear forces gradually degrade the cell spanning network resulting in shear thinning (Marshall, Zukoski & Goodwin 1989; Bonnecaze & Brady 1992a). At low shear rates the suspension viscosity scales inversely with shear rate, which is consistent with the existence of a dynamic yield stress. Although Bonnecaze & Brady (1992b) showed

that in the limit of no Brownian forces ($1/\lambda \equiv 0$) the suspension has a dynamic yield stress, there has not been a similar study for large but finite λ, and it has simply been assumed that these ER suspensions have a dynamic yield stress. At high shear rates, the particle network is completely destroyed and the suspension viscosity approaches that of the bare suspension with no field applied. Marshall et al. (1989) found that the Mason number collapses the viscosity data for different temperatures, shear rates, and field strengths onto a single curve, i.e., at high field strengths the suspension rheology is described by only Ma and ϕ, the suspension volume fraction.

Efforts to make neutrally buoyant ER fluids have turned the focus to smaller particles and thus smaller λ, but there is limited rheological data in this regime. Studies for $30 < \lambda < 2000$ (Halsey, Martin & Adolf 1992; Melrose 1992) indicate no yield stress; at low shear rates the suspension shear thins with its viscosity scaling as $\dot{\gamma}^{-\alpha}$ where α is less than 1. On the other hand, simulations on a 0.16 volume fraction suspension (Sun & Tao 1995) showed a low-shear viscosity for $\lambda < 90$ and a yield stress for $\lambda = 90$, their maximum λ. Rheological studies for $\lambda < 30$ were done only at low volume fractions, $\phi = 0.16$ (Sun & Tao 1995), where the suspension is not flocculated. Contrary to the behavior at high λ, for finite λ the Mason number is not sufficient to collapse the rheological response onto a single curve as it does not include thermal effects.

There is still no clear picture of the low-shear-rate behavior of ER fluids, particularly when flocculated at moderate but finite λ. It remains to be seen if they have a dynamic yield stress as for $1/\lambda \equiv 0$ suspensions (Bonnecaze & Brady 1992b), or if

they have a low shear viscosity similar to Brownian hard-sphere suspensions, $\lambda \equiv 0$ (Phung 1993), or dispersed ER suspensions, $\lambda \sim$ O(1) (Sun & Tao 1995). This is a crucial issue for ER fluids and the answer will have far reaching consequences. The yield stress is often an important design parameter for several potential applications. The ER valve, for example, designed to control flow, is required to sustain a stress. In addition, this question – whether there is a yield stress or a low-shear viscosity – is of generic importance as it will aid in understanding the flow behavior of flocculated suspensions generally.

Clearly, additional rheological data for smaller λ and a wider range of Mason numbers are needed. To this end, Stokesian Dynamics simulations have been used to calculate the suspension viscosity for a wide range of λ and Ma, with area fraction ϕ_A, the ratio of the projected area of the particles to the area of the cell, of 0.4. By the two-thirds rule, an area fraction of 0.4 is equivalent to a volume fraction of 0.27, and is above the minimum volume fraction necessary for an aggregated network to form. Simulations in the absence of shear show that flocculation occurs at $\lambda \approx 4$. We note that all values of λ defining the boundary between regions of different behavior are approximate; a more accurate determination requires large system sizes. For smaller λ, the suspension forms particle chains that align along the field direction but do not span the cell; here we find a low-shear viscosity that can be predicted by considering a regular perturbation to the equilibrium structure. For $4 < \lambda < 10$ the chains span the cell and aggregate to form thicker clusters with a hexagonal lattice structure. Here we find a low-shear viscosity that scales exponentially with the pair potential well depth.

A simple argument based on viscoelastic theory is used to explain this scaling. In addition, the low shear limiting behavior is observed when $\dot{\gamma} < (D/a^2)\lambda e^{-\lambda}$, where $D = kT/6\pi\eta a$ is the diffusivity of an isolated Brownian particle. Above $\lambda \sim 10$, the suspension consists of a network of flocs made up of strands aligned along the field direction. The flocculated structures formed also have a hexagonal order but there are vacancies within the lattice. Over the shear rate range accessible in our simulations, $2 \cdot 10^{-5} < Ma < 10^{-3}$, we find neither a dynamic yield stress nor a low shear viscosity; instead the viscosity scales approximately as $Ma^{-\alpha}$, where α varies from 0.9 to 1. It is argued, however, based on theoretical considerations, that these suspensions should also show a low-shear viscosity when $\dot{\gamma} < (D/a^2)\lambda e^{-\lambda}$.

The first normal stress difference, antisymmetric sress, and the short- and long-time diffusivities are also studied to complete the dynamical picture for ER suspensions. Here again the results are discussed in term of the delineated regimes. The results for the first normal stress difference are unusual in that due to the anisotropy of ER suspensions with respect to the compressional and extensional axes, the first normal stress difference does not vanish as the shear rate vanishes. Also, the suspension stress is antisymmetric due to the electrostatic force and $\Sigma_{xy} \neq \Sigma_{yx}$. The results for the polarization contribution to Σ_{xy} are also presented. The short- and long- time diffusivities collaborate the structural findings.

2.2 Simulation Method

The Stokesian Dynamics method with Brownian motion is detailed elsewhere (Bossis & Brady 1987, 1989; Phung 1993; Phung, Brady & Bossis 1996), so only the important features will be discussed here. For N rigid, neutrally buoyant particles suspended in an incompressible fluid of density ρ and viscosity η, the motion of the particles is governed by the coupled N-body Langevin equation:

$$\mathbf{m} \cdot \frac{d\mathbf{U}}{dt} = \mathbf{F}^H + \mathbf{F}^B + \mathbf{F}^P, \tag{2.1}$$

where $\mathbf{U}$ is the particle's translational/rotational velocity vector, $\mathbf{m}$ is its mass/moment of inertia tensor, $\mathbf{F}^H$ is the hydrodynamic force, $\mathbf{F}^B$ is the Brownian force, and $\mathbf{F}^P$ is the interparticle force. For colloidal particles the viscous forces dominate the inertial forces ($Re = \rho\dot{\gamma}a^2/\eta \ll 1$) such that the fluid dynamics is described by Stokes equations; thus the hydrodynamic force is given by

$$\mathbf{F}^H = -\mathbf{R}_{FU} \cdot (\mathbf{U} - \langle \mathbf{U} \rangle) + \mathbf{R}_{FE} : \langle \mathbf{E} \rangle, \tag{2.2}$$

where $\langle \mathbf{U} \rangle$ is the imposed flow at infinity evaluated at the particle centers and $\langle \mathbf{E} \rangle$ is the symmetric part of the velocity gradient tensor. The tensors $\mathbf{R}_{FU}$ and $\mathbf{R}_{FE}$ are the particle configuration-dependent hydrodynamic resistance tensors that relate the hydrodynamic force and torque on the particles to their motion relative to the fluid and to the imposed shear flow, respectively.

The Brownian force comes from the thermal fluctuations in the fluid and is characterized by

$$\langle \mathbf{F}^B \rangle = 0 \quad \text{and} \quad \langle \mathbf{F}^B(0)\, \mathbf{F}^B(t) \rangle = 2kT\mathbf{R}_{FU}\delta(t), \tag{2.3}$$

where the angle brackets denote an ensemble average. The amplitude of the correlation of $\mathbf{F}^B$ at time 0 and time t comes from the fluctuation-dissipation theorem for the N-body system.

The electrostatic interparticle force is calculated by the method of Bonnecaze & Brady (1992a). Starting with the electrostatic energy density, $\mathcal{U}$, for a system of non-charged polarizable particles in an electric field, the force on each particle is given as the derivative of the energy with respect to position:

$$\mathbf{F}^{\alpha} = -\frac{\partial \mathcal{U}(\mathbf{x})}{\partial \mathbf{x}_{\alpha}} = -\frac{1}{2}\left(\frac{\partial}{\partial \mathbf{x}_{\alpha}}\mathbf{S}_E \cdot \mathcal{E}\right). \tag{2.4}$$

Here $\mathcal{U}(\mathbf{x})$ is the electrostatic energy density, $\mathbf{x}_{\alpha}$ is the position vector of particle α, $\mathbf{S}_E$ the induced particle dipole, and $\mathcal{E}$ is the applied electric field times a unit vector of length N, where N is the number of particles. There is the linear relationship between the charge and induced dipole, and the potential and electric field:

$$\begin{pmatrix} \mathbf{q} \\ \mathbf{S}_E \end{pmatrix} = \mathbf{C}(\mathbf{x}) \cdot \begin{pmatrix} \Phi \\ \mathcal{E} \end{pmatrix} = \begin{pmatrix} \mathbf{C}_{q\Phi} & \mathbf{C}_{q\mathcal{E}} \\ \mathbf{C}_{S\Phi} & \mathbf{C}_{S\mathcal{E}} \end{pmatrix} \cdot \begin{pmatrix} \Phi \\ \mathcal{E} \end{pmatrix}, \tag{2.5}$$

which defines the grand capacitance tensor $\mathbf{C}(\mathbf{x})$, that couples the charge and dipole to the potential and electric field in the same manner that the resistance tensor couples the force to the velocity for Stokes flow. The subscripts on the tensors $\mathbf{C}$ relate the charge $\mathbf{q}$ or dipole $\mathbf{S}_E$ to the electrostatic potential Φ or the electric field $\mathcal{E}$. For charge free particles forming an ER fluid,

$$\mathbf{S}_E = \hat{\mathbf{C}}(\mathbf{x}) \cdot \mathcal{E} = (\mathbf{C}_{S\Phi} \cdot \mathbf{C}_{q\Phi}^{-1} \cdot \mathbf{C}_{q\mathcal{E}} - \mathbf{C}_{S\mathcal{E}}) \cdot \mathcal{E}. \tag{2.6}$$

The grand capacitance tensor is purely geometric, depending only on the particle configuration and the particle to fluid dielectric ratio. Combining equations (2.4) and

(2.5), the interparticle force is given by the quadratic form

$$\mathbf{F}^{\alpha} = -\frac{1}{2}\mathcal{E} \cdot \frac{\partial \hat{\mathbf{C}}(x)}{\partial \mathbf{x}_{\alpha}} \cdot \mathcal{E}. \tag{2.7}$$

Finally, combining Equations (2.2) through (2.7), and the condition that the inertial forces are negligible, Equation (2.1) is integrated to obtain the evolution equation for the particle positions,

$$\Delta\mathbf{x} = Pe\ \left(\langle \mathbf{U} \rangle + \mathbf{R}_{FU}^{-1} \cdot \left[\mathbf{R}_{FE} : \langle \mathbf{E} \rangle + Ma^{-1}\mathbf{F}^{P}\right]\right)\ \Delta t + \nabla \cdot \mathbf{R}_{FU}^{-1}\ \Delta t + \mathbf{X}(\Delta t), \tag{2.8}$$

where $\Delta\mathbf{x}$ is the change in particle position over a time step of Δt. The last term, $\mathbf{X}(\Delta t)$, is a random displacement due to Brownian motion that has zero mean and covariance given by the inverse of the resistance tensor:

$$\langle \mathbf{X} \rangle = 0 \quad \text{and} \quad \langle \mathbf{X}(\Delta t)\mathbf{X}(\Delta t) \rangle = 2\,\mathbf{R}_{FU}^{-1}\Delta t. \tag{2.9}$$

Here, $\mathbf{x}$ has been made non dimensional by a, t by a^2/D, the hydrodynamic forces by $6\pi\eta a^2\dot{\gamma}$ and the electrostatic force by $12\pi\epsilon a^2(\beta\mathcal{E})^2$. The parameters Ma and Pe are the dimensionless ratio of the viscous to polarization forces and the viscous to thermal forces, respectively, as discussed in the introduction. Both can be expressed as ratios of time scales: $Ma = \tau_{ER}/\tau_V$ and $Pe = \tau_B/\tau_V$, where $\tau_{ER} = \eta/(2\epsilon(\beta\mathcal{E})^2)$ gives the time of aggregation due to the polarization forces, $\tau_V = 1/\dot{\gamma}$ gives the time scale of the shear flow, and $\tau_B = a^2/D$, gives the time scale of diffusion of an isolated Brownian particle.

Equation (2.8) is the core of the simulation and is used to follow the motion of N particles given their initial configuration. The dependence on Pe and Ma in Equation

(2.8) can be replaced with either Pe and λ, or Ma and λ, as $\lambda = Pe/(12Ma)$. We shall generally present results in terms of Ma and λ, although any two dimensionless groups could be used. In addition to Ma and λ, the dynamics depends on the volume fraction ϕ and the relative dielectric constant ratio ϵ_p/ϵ_f.

For rheology, the suspension bulk stress is needed, and is given by

$$\langle\sigma\rangle = -\langle p\rangle \mathbf{I} + 2\eta\langle\mathbf{E}\rangle - nkT\mathbf{I} + n[\langle\mathbf{S}^H\rangle + \langle\mathbf{S}^B\rangle + \langle\mathbf{S}^P\rangle]. \tag{2.10}$$

Here, $\langle\sigma\rangle$ is the macroscopic average stress tensor, $\langle p\rangle$ is a constant denoting the pressure in the incompressible medium, $2\eta\langle\mathbf{E}\rangle$ is the deviatoric stress contribution from the fluid, $-nkT\mathbf{I}$ is the isotropic stress associated with the thermal energy of the Brownian particles; $\mathbf{I}$ is the isotropic tensor, and n is the number density of particles. The stresses $\langle\mathbf{S}^H\rangle, \langle\mathbf{S}^B\rangle$, and $\langle\mathbf{S}^P\rangle$ are associated with hydrodynamics, Brownian motion, and the electrostatic interparticle interactions, respectively, and in dimensional form are

$$\langle\mathbf{S}^H\rangle = -\langle\mathbf{R}_{SU}\cdot\mathbf{R}_{FU}^{-1}\cdot\mathbf{R}_{FE} - \mathbf{R}_{SE}\rangle : \langle\mathbf{E}\rangle, \tag{2.11}$$

$$\langle\mathbf{S}^B\rangle = -kT\nabla\cdot\langle\mathbf{R}_{SU}\cdot\mathbf{R}_{FU}^{-1}\rangle, \tag{2.12}$$

$$\langle\mathbf{S}^P\rangle = -\langle(\mathbf{R}_{SU}\cdot\mathbf{R}_{FU}^{-1} + \mathbf{x}\mathbf{I})\cdot\mathbf{F}^P\rangle. \tag{2.13}$$

The hydrodynamic stress is the added mechanical or contact stress due to the resistance of the rigid particles to local deformation of the fluid. The Brownian stress is a thermodynamic stress that results from the deformation of the equilibrium structure. The interparticle stress has two components. The first component, $\mathbf{R}_{SU}\cdot\mathbf{R}_{FU}^{-1}\cdot\mathbf{F}^P$, comes from the velocity field generated by particle motion arising from the

interparticle forces, and is hydrodynamic in origin. The second term, $\mathbf{xI} \cdot \mathbf{F}^P$, is the direct contribution to the bulk stress from interparticle forces; it is of the same form as occurs in molecular systems. Note that the interparticle stress may be antisymmetric for ER fluids due to the anisotropic potential.

The hydrodynamic stress is always positive and scales with the largest length cubed. In contrast, the Brownian and interparticle stresses can be positive or negative depending on the microstructure. When the polarization forces dominate, particles form chains or clusters along the field direction that tilt, strain, and eventually break under shear. The imposed shear flow pulls the chained particles apart along the extensional axis, while the polarization force opposes the fluid and keeps the particles aggregated, resulting in a positive contribution to the stress. The Brownian force, on the other hand, pushes particles apart along the extensional axis resulting in a negative Brownian stress. When the Brownian or viscous force dominates, the interparticle and Brownian stresses are opposite in sign to those in the previous case. Shearing clusters particles along the compressive axis, which is opposed by Brownian forces resulting in a positive Brownian contribution to the stress. In contrast, the polarization force acts with the fluid to push particles together resulting in a negative contribution to the bulk stress.

The relative viscosity of the suspension is defined by the ratio of the yx component of the bulk stress to the yx component of the bulk rate of strain, with the imposed linear shear flow $\langle U_x \rangle = \dot{\gamma} y$. In dimensionless form,

$$\eta_r = 1 + \eta_r^H + \eta_r^{SP} + \eta_r^{xF} + \eta_r^B, \tag{2.14}$$

where the superscripts H and B indicate the hydrodynamic and Brownian contributions, respectively. The superscripts SP and xF indicate contributions from the first and second terms in the interparticle stress (Eq. (2.13)), respectively.

The hydrodynamic resistance and electrostatic capacitance tensors are constructed by incorporating both near-field lubrication and far-field many-body interactions as outlined in Phung, Brady & Bossis (1996) and Bonnecaze & Brady (1992a).

2.3 Results and Discussion

The method outlined above was applied to an unbounded monolayer of monodisperse dielectric particles with an electric field in the y-direction and shearing in the x-direction, as illustrated in figure 2.1. We used a monolayer because this reduces the simulation time but still captures the essential physics of an ER suspension. Indeed, Bonnecaze & Brady's (1992a) Stokesian Dynamics monolayer simulations in the non-Brownian limit compared quantitatively to experiments. An unbounded suspension is simulated by periodically replicated 25 identical spherical particles in a square cell forming a 0.4 area fraction suspension. The dielectric constant ratio was $\epsilon_p/\epsilon = 4$, giving $\beta = 1/2$. The time step used varied from 0.001 to $2 \cdot 10^{-5}$. The equilibrium structure formation for $0 < \lambda < \infty$ was studied, monitoring the electrostatic energy to assure steady state. The suspension viscosity was studied for $0 < \lambda \leq 10^{12}$ and $5 \cdot 10^{-6} \leq Ma \leq \infty$. In this case, steady state was determined by monitoring the time average viscosity and ensuring that the cell completed at least one strain.

2.3.1 The Suspension Structure

The suspension energy, $\mathcal{U}(x)$ (see Eq. 2.4), at steady state is plotted as a function of λ in figure 2.2. The energy of the initial dispersed configuration generated by Monte Carlo methods is arbitrarily set to 0. The plot shows that the suspension energy approaches an asymptope at $\lambda = 5.8$, where the particles have ordered into a single cluster with an hexagonal lattice order as seen in figure 2.3(b). For $\lambda > 5.8$, the suspension energy is slightly lower; in this case the lattice formed is incomplete with vacancies, and continued simulations did not anneal the open structures (figure 2.3(c)). (figure 2.3(c)).

To quantify the orientational and positional order of the suspension, we use the order parameters

$$p_{1,2} = \frac{1}{N} \sum_{j}^{N} e^{i\mathbf{b}_{1,2} \cdot \mathbf{r}_j}, \tag{2.15}$$

where $\mathbf{b}_{1,2}$ are unit vectors along and 60^o relative to the field direction, respectively, and the sum is over all particle pairs. Therefore p_1 measures formation of chains along the field direction and p_2 measures aggregation of these chains into a hexagonal lattice structure. A hexagonal lattice has $p_1 = p_2 = 1$, while a dispersed random suspension has vanishing order parameters. Thus, p_1 provides a measure of particles in contact aligned with the field, and p_2 measures the aggregation of chains.

Figure 2.4 shows $p_{1,2}$ as functions of λ. Note that p_1 is non-zero for $\lambda \geq 0.8$; regardless of the magnitude, an applied field introduces anisotropy into the suspension structure. For $\lambda = 0.8$, the pair-distribution function at contact parallel and perpendicular to the applied field are $g_{\parallel}(2) = 5.7$ and $g_{\perp}(2) = 1.9$, respectively, which

should be compared with $g(2) = 3.2$ in the absence of the applied field, indicating that there is a preference for particles in contact to align with the field and a deficit of particles in contact perpendicular to the field. The resulting structure is reminiscent of the weakly anisotropic structures predicted by Hayter & Pynn (1982) and more recently by Xu & Hass (1993). Treating the particles as point dipoles, Hayter & Pynn used the mean spherical approximation to express the equilibrium pair distribution as a series of Legendre polynomials with non-zero even terms. They used only the first two terms to calculate the pair-distribution function for small λ. Xu & Hass improved on this method by retaining an additional term in the expansion for the pair-distribution function. Both groups found a small repulsion at contact perpendicular to the field direction – $g_\perp(2) < 1$ – for a comparable volume fraction of 0.2 for Hayter & Pynn's work (as detailed in Adriani & Gast 1988) and 0.25 for Xu & Hass's work, which is not seen in these simulations. This difference may be a result of the point-dipole approximation used in their theories, which overestimates particle repulsion near contact as compared with our multipolar interactions.

From figure 2.4 two critical equilibrium transitions can be identified. The first occurs at $\lambda \approx 1.6$ where p_1 increases rapidly, indicating chaining along the field direction. The second transition occurs at $\lambda \approx 4$ where p_2 increases, indicating aggregation of chains. At $\lambda = 5.8$, the particles are roughly ordered into a single cluster with a hexagonal lattice structure (figure 2.3b). Note that p_1 and p_2 are not identically 1 because the particles continue to fluctuate within the lattice structure. Also note that the periodic boundary conditions preclude addition of more particles

to the cluster so we cannot determine the characteristic width of these structures. Indeed, that they form a single cell-spanning cluster is likely to be an artifact of the simulation box size and/or number of particles. Simulations with 50 particles at the same area fraction formed two separate cell-spanning clusters, each two to three particles thick and each with a hexagonal lattice structure as seen in figure 2.5.

For $\lambda > 10$, the suspension forms a cell spanning network with a hexagonal order but with vacancies within the lattice, defining a third, kinetic, transition. This "kinetically" frozen state has also been observed experimentally (Klingenberg et al. 1991) and with simulations at large to infinite λ (Bonnecaze & Brady 1992a; Melrose 1992). Rearrangement within the structure requires particles to overcome their mutual attractive potential wells, which occurs with a frequency that scales as $(D/a^2)\lambda e^{-\lambda}$ (Kramers 1940, Chandrasekhar 1943), such that the open structures may anneal given sufficient time. However, the simulations indicated no change in the microstructure or order after a dimensionless time of 2, corresponding to approximately 12 seconds, using typical values for a, T, and η. For most applications the microstructure set-up time is a few seconds, and for all practical purposes the suspension does not achieve its maximum order.

Similar phase behavior has been observed in magnetorheological systems both experimentally (Liu et al. 1993; Hwang & Wu 1993) and numerically (Tao 1993). Using simulated annealing methods, Tao found that a 3D, 0.15 volume fraction suspension remained relatively disordered for $\lambda \leq 3$. For $3 < \lambda < 7$ the particles formed randomly distributed chains and remained separated at steady state. For $\lambda > 7$

the particles formed randomly distributed chains that subsequently aggregated into a BCT lattice cluster. He did not find a kinetically arrested structure since the Monte Carlo method he used assumes equilibrium. Liu et al.[1] performed experiments with monodisperse ferrofluid emulsion droplets $0.55\mu m$ in diameter in an aqueous solution forming volume fractions from 0.03 to 0.13. Structure formation was probed with optical microscopy and light scattering. They found that the particles first ordered into chains at $\lambda = 1.5$, and, depending on the volume fraction, the chains either remained separated or aggregated to form columns upon a further increase in λ. For $\lambda \geq 10$, the suspension aggregated kinetically and formed an open structure.

Hwang & Wu (1993) used small angle light scattering to study structure formation in an aqueous suspension of $1\mu m$ diameter magnetic particles for volume fractions up to 10% subjected to a magnetic field. They identified two transition field strengths, H_{C1} and H_{C2}. Below H_{C1} the suspension was a disordered liquid, for $H_{C1} < H < H_{C2}$, the particles assembled into randomly spaced chains along the field direction, and for $H > H_{C2}$ these chains aggregated into ordered structures. They also found a kinetically aggregated region for $H \gg H_{C2}$ where the particles formed a gel with no long-range order. Both transition fields were found to be volume fraction dependent; H_{C1} decayed with the volume fraction to the $-\frac{1}{4}$ power, while H_{C2} decayed as the volume fraction to the $-\frac{1}{2}$ power. At the highest volume fraction studied, $\phi = 0.1$, the single chain regime was vanishingly small. From Hwang & Wu's reported field strengths, we estimate that the suspension formed aggregated columns at $\lambda \approx 1$ and

[1]Liu et al. defined λ as the ratio of the dipole energy at contact along the field direction to the thermal energy, which is the same definition used here.

a kinetic gel at $\lambda \approx 58$.

In summary, from simulations we find that flocculation occurs above $\lambda \approx 4$. Within the flocculated region, there is an equilibrium flocculated regime, $4 < \lambda < 10$, where particles order into an hexagonal structure, and a kinetically aggregated regime for λ above 10 where the suspension forms a hexagonal lattice structure with vacancies within the lattice.

2.3.2 The Suspension Dynamics: Self Diffusivities

Although not a general consideration for ER fluids, the short- and long-time self diffusivities are presented here for completeness. The short- and long-time diffusivities are calculated for the suspension without flow. Both generally differ from the isolated diffusivity, D_0, because the random path a particle takes is hindered by its interactions with neighboring particles.

The short-time self-diffusivity, D_0^s, measures the average instantaneous mobility of a particle and is given by an average over all configurations as

$$D_0^s = \langle \mathbf{D}_{ii} \rangle \text{ no sum on } i, \tag{2.16}$$

where the N-particle diffusivity tensor is $\mathbf{D} \equiv kT\mathbf{R}_{FU}^{-1}$ in dimensional form. Due to lubrication forces, a pair of particles closely spaced move for short times as a single larger particle resulting in a decrease in their mobility, and thus D_0^s reflects changes in the local microstructure.

In figure 2.6 the short-time self-diffusivities in the $\mathbf{x}$ and $\mathbf{y}$ directions are plotted for $0.8 \leq \lambda < 1000$. Corresponding data for $0.8 \leq \lambda \leq 8.3 \cdot 10^{12}$ are given in table 2.1.

The short-time self-diffusivity decreases with λ and is anisotropic in the dispersed and equilibrium flocculated regimes. In the dispersed regime, $\lambda < 4$, D_0^s varies very little with λ, decreasing from 0.567 to 0.489. Here, the mobility is anisotropic with D_{yy} up to 30% smaller than D_{xx}. This is consistent with the findings discussed in the previous section; small pairs of particles aligned along the field direction are formed and move at short times as a single rod-like particle in the **y** direction, resulting in a decreased mobility in the field or **y** direction.

In the equilibrium flocculated regime, $4 < \lambda < 10$, the mobility is also anisotropic, D_{yy} is up to 26% smaller than D_{xx}, but somewhat less so than in the dispersed regime. As the chains begin to aggregate to form thicker clusters, the diffusivity in the **x** direction begins to decrease and the short-time self-diffusivity becomes less anisotopic. As discussed in the previous section, although flocculated, particles continue to fluctuate within a structured hexagonal lattice. Due to the lubrication forces, the cell spanning chains move along the field direction as a single rod-like particle with a smaller diffusivity. Since the clusters are not tightly packed along the **x** direction, particles are free to move at short times as single particles along the transverse direction. On the other hand, in the kinetically flocculated regime, the mobility is only slightly anisotropic. Here, although the structure is kinetically arrested and does not form a hexagonal lattice, the particles are more tightly packed in the transverse or **x** direction (compared to the equilibrium flocculated regime) and have limited mobility in both the **x** and **y** directions.

The short-time rotational diffusivities are plotted in figure 2.7 and show trends

similar to the averaged translational short-time diffusivity.

On a large time scale, particles must move past their surrounding neighbors, deforming the local microstructure. At sufficiently long times a steady state is reached and the mean square particle displacement again grows linearly in time, i.e., $\langle y^2(t)\rangle = 2D^s_\infty t$; $\langle x^2(t)\rangle = 2D^s_\infty t$, and the long-time self-diffusivity can be determined from the average of the mean square displacement in the **x** and **y** directions. Due to the exponentially large escape time scale for flocculated ER fluids, however, determination of the long-time self-diffusivity is statistically difficult for any but the weakest potential, i.e., $\lambda < 4$ the dispersed regime, and so only these results are presented.

In figure 2.8 the long-time self-diffusivity is plotted as a function of λ for $\lambda < 4$. The corresponding data can be found in table 2.2. Since a particle has to deform its local surroundings to diffuse at long times, the long-time self diffusivity is smaller than its short-time counterpart. Brady (1994) predicted a long-time self-diffusivity that scales inversely with the pair potential at contact. This scaling is in agreement with our results as the long-time self-diffusivity scales inversely with $g(2)$ for $\lambda < 4$.

2.3.3 The Suspension Dynamics: Viscosities

Figure 2.9 shows the simulation results for the relative suspension viscosity as a function of Ma for λ from 0.8 to 10^{12}; Bonnecaze and Brady's (1992) results for $\lambda = \infty$ are included for comparison. The corresponding data are given in tables 2.3 to 2.6. The individual contributions (cf. Eq. (2.14)) are given in tables B.1 through B.3 in Appendix B. At large λ the interparticle force contribution dominates, while at large Ma the hydrodynamic contribution dominates. The Brownian and interparticle con-

tributions oppose each other as discussed in section II. When viscous forces dominate, $Ma \gg 1$, the suspension has a shear viscosity equal to the bare suspension viscosity, regardless of λ. Thus as $Ma \to \infty$ hydrodynamics alone determine the suspension behavior. As the shear rate or Ma decreases, the suspension viscosity increases, as both polarization and thermal forces become important; the viscosity now depends on λ as well as Ma.

Dispersed regime: $\lambda < 4$

In the dispersed regime, $\lambda < 4$, the suspension viscosity shear thins, as one would expect from the analogous behavior of hard-sphere suspensions (Van der Werff & de Kruif 1989; Phung, Brady & Bossis 1996). The low-shear viscosity is found to scale exponentially with the pair potential well depth and can be estimated by regular perturbation theory, similar to that for hard spheres by Brady (1993), for a square well fluid by Bergenholtz & Wagner (1994), or for dilute suspensions of "sticky" spheres (Russel 1984; Cichocki & Felderhof 1990). The method, detailed in Appendix A, models the particle distribution as Boltzmann and neglects all anisotropy in the suspension structure. Also, hydrodynamics are ignored and only the interparticle force contribution to the stress is calculated. A more rigorous analysis can be employed (Brady 1993), but this approximate method suffices to show the source of the exponential relationship between the low-shear viscosity and the pair potential well depth. The low-shear viscosity scales as the equilibrium pair-distribution function at contact times the perturbation to the structure caused by flow. The equilibrium

pair-distribution in turn behaves as $g \approx g_{HS}\, e^{\lambda}$, where g_{HS} is the hard-sphere value; hence the exponential scaling of the viscosity with λ comes directly from the change in the equilibrium pair-distribution with the electric field. A plot of η_0 as a function of λ (figure 2.10) shows that the simple approximate theory predicts that $\eta_0 \sim e^{\lambda}$ due to $g(2)$ increasing as e^{λ}.

Equilibrium flocculated regime: $4 < \lambda < 10$

In the equilibrium flocculated regime, $4 < \lambda < 10$, a low-shear viscosity is seen in figure 2.9 as $Ma \rightarrow 0$ whose magnitude also scales exponentially with λ as shown in figure 2.11. The exponential relationship between the low-shear viscosity and the pair potential is remarkably similar to Buscall et al.'s (1993) observation in concentrated, depletion flocculated, dispersions (as detailed in Chapter 4). Buscall et al.'s suspension consisted of a non aqueous polymer latex in a low-aromatic white spirit flocculated by adding a soluble non-adsorbing polymer, and the apparent pair potential well depth was varied by changing the soluble polymer concentration. They found that the low-shear viscosity increased exponentially with the potential well depth for well depths from $2kT$ to $25kT$.

We also see that the shear rate at which shear thinning first occurs scales *inversely* with the exponential of λ as shown in figure 2.12, i.e., the low-shear-rate asymptote is reached for shear rates that decrease exponentially as $e^{-1.88\lambda}$. The critical Mason number, Ma_c, that marks the transition from shear thinning to the low-shear viscosity plateau for $4 < \lambda < 10$ was determined from the intercept of the lines $\eta_r = \eta_0$ and

$\eta_r \sim Ma^{-1}$ in the shear thinning region. In reality, the transition occurs over a range of Mason numbers and the viscosity was not seen to shear thin as Ma^{-1} for $\lambda < 10$. Since we were unable to distinguish between the transition and the true shear thinning regions, we assumed a scaling similar to the scaling for very large to infinite λ. The ratio of the diffusion time out of a potential well τ to the shear time $1/\dot{\gamma}$ yields a new dimensionless shear rate $(\dot{\gamma}a^2/D\lambda)\, e^{\lambda}$. When $(\dot{\gamma}a^2/D\lambda)\, e^{\lambda} < 1$, the suspension dynamics are diffusion limited in the same manner that $\dot{\gamma}a^2/D < 1$ marks the diffusion limited dynamics for Brownian hard-spheres.

The perturbation method used to estimate the low-shear viscosity for $\lambda < 4$ will not suffice for larger λ because the suspension structure cannot be described in a simple pair-wise manner. To illustrate this, the pair-distribution function at contact, g(2), is plotted as a function of λ in figure 2.13 and clearly shows that g(2) scales exponentially with λ only for $\lambda < 4$. Above $\lambda \approx 4$, g(2) approaches a constant asymptote as the suspension has formed a cell-spanning network.

To predict the low-shear viscosity in this region of λ, we note from linear viscoelastic theory that for a solid-like structure η_0 is given by the product of the shear modulus and a time scale of relaxation, τ (Ferry 1980):

$$\eta_0 = G_0\tau. \tag{2.17}$$

The shear modulus can be estimated by applying a small strain, γ, to the suspension, and is given by the ratio of the stress, Σ_{yx}, to the strain in the limit γ approaches zero:

$$G_0 = \lim_{\gamma \to 0} \frac{\Sigma_{yx}}{\gamma}. \tag{2.18}$$

Since we are simply interested in the scaling behavior of the stress, we represent the network as a single chain of particles aligned along the field direction (see figure 2.14) to which a small strain is applied. The major contribution to the stress is from the electrostatic restoring force attempting to realign the strained structure with the electric field. The stress is antisymmetric in ER fluids because of the noncentral polarization forces, and the modulus is properly a tensor. Here we use the restoring force associated with the straining chain to estimate the modulus (Klingenberg & Zukoski 1990; Kraynik, Bonnecaze & Brady 1991).

The stress is dominated by electrostatic forces,

$$\mathbf{\Sigma} \approx -\frac{1}{2V} \sum_{\alpha=1}^{N} \sum_{\beta=1}^{N} (\mathbf{x}_\alpha - \mathbf{x}_\beta) \mathbf{F}^P_{\alpha\beta}, \tag{2.19}$$

where $\mathbf{F}^P_{\alpha\beta}$ is the electrostatic force on particle α due to particle β. We approximate the stress in a pairwise manner from nearest neighbors only, yielding

$$\mathbf{\Sigma} = -n\, \mathbf{r}_{12}\, \mathbf{F}^P_{12}. \tag{2.20}$$

From the interparticle force as the derivative of the pair potential evaluated for two particles contacting each other oriented at an angle θ relative to the field direction, we have

$$\Sigma_{yx} = -\frac{kT}{a^3} \phi\lambda \frac{9}{8\pi} \sin\theta \cos\theta \left(1 - 5\cos^2\theta\right). \tag{2.21}$$

For small strains $\gamma = \theta \ll 1$ and the modulus is given by

$$\frac{G_0 a^3}{kT} = \frac{9}{2\pi} \phi\lambda. \tag{2.22}$$

To estimate the relaxation time, τ, we note that the strained structure relaxes when particles diffuse out of their mutual potential wells. This diffusive time is much slower than the isolated particle diffusion time, a^2/D, as a particle must overcome the high potential barrier. Kramers (1940) showed (see also Hänggi et al. 1990, Potanin et al. 1995) that two particles in a mutual potential well of depth $U_{min}/kT \gg 1$ will escape on a time of order $(a^2/D)(kT/U_{min})e^{U_{min}/kT}$, where we have estimated the second derivative of the potential energy at equilibrium and barrier points as simply U_{min}/a^2; it is this time scale that will determine the low-shear viscosity for ER and other flocculated dispersions. Thus, with $U_{min}/kT \approx \lambda$ in the prefactor, we have

$$\eta_0 \sim \eta\phi e^{U_{min}/kT}. \tag{2.23}$$

The potential well depth U_{min}/kT characterizing the escape time differs from λ because of two factors. First, the dimensionless ratio λ gives the pair potential well depth along the field direction assuming isolated point dipoles, and is a good approximation for dilute suspensions with weak interactions. However, for the volume fraction and field strengths of interest here, the particles cannot be treated simply as isolated point dipoles. As evidenced by the equilibrium structure studies, the suspension consists of particle aggregates, and since the induced particle dipole is proportional to the local electric field rather than the applied external electric field, neighboring particles will affect the pair potential. The potential well depth between two particles in contact can be estimated from the suspension energy, $u(r, \theta)$ discussed in the introduction, with the induced particle dipole $\mathbf{S}_E$ defined in section II replacing

the isolated point dipole

$$\mathcal{U}_{dipole} = \mathbf{S}_E \cdot \mathbf{T} \cdot \mathbf{S}_E, \tag{2.24}$$

where $\mathbf{T}$ is the dipole-dipole interaction:

$$\mathbf{T} = \frac{1}{r^3}\left(\delta - \frac{3\mathbf{rr}}{r^2}\right). \tag{2.25}$$

The average potential minimum is obtained by averaging $\mathcal{U}_{dipole}$ over all the particle pairs in the suspension, and is depicted as a function of λ in figure 2.15. Note that $\mathcal{U}_{dipole}/kT$ is indeed proportional to λ, but is enhanced due to the presence of other particles. Below the flocculation point, λ gives a good estimate of the potential well depth. When flocculated, however, neighboring particles further enhance the pair potential and $\mathcal{U}_{dipole}/kT$ scales as 4.5λ.

The second factor influencing the potential well depth is the dependence of the interparticle potential on the relative orientation of the particle pair to the applied electric field. A particle is more likely to escape from its potential well if it is oriented relative to its neighbor with a significant component perpendicular to the applied field where the potential is actually repulsive. This angular dependence leads to a decrease in the value of the potential barrier over the enhanced dipole value $\mathcal{U}_{dipole}/kT$. Further, the network structure itself influences the detailed form of the potential well. Thus, while U_{min}/kT must be proportional to λ, it is not precisely equal to λ, and should depend on the detailed network structure formed. Hence we write

$$\frac{U_{min}}{kT} = \beta(\phi)\lambda, \tag{2.26}$$

and find the coefficient β by fitting (2.23) to the experimental data. The data for

the low-shear viscosity yields $\eta_0/\eta = 0.16\ e^{1.57\lambda}$, as shown in figure (2.11). Thus, $\beta \approx 1.57$, and the difference between the prefactor, 0.16, and the modulus estimate, shows that the characteristic escape time is quantitatively estimated by $0.42\ e^{1.57\lambda}$. The difference between the 1.57 factor in the exponent for the low-shear viscosity and the 1.88 factor for the transition shear rate for the low shear thinning behavior is a result of the approximate method used to estimate Ma_c.

The ratio of the diffusion time out of a potential well τ to the shear time $1/\dot{\gamma}$ yields a new dimensionless shear rate $(\dot{\gamma}a^2/D\lambda)\ e^{\lambda}$. The reduced viscosity defined as $(\eta-\eta_\infty)/(\eta_0-\eta_\infty)$ is plotted as a function of the new reduced shear rate $(a^2/D\lambda)e^{\lambda}$ in figure 2.16. When the shear rate is rescaled with the escape time, τ, the data collapse onto a single curve. The data for $\lambda = 2.5$ and 3.3 also fit the curve as the low-shear viscosity here was also seen to scale exponentially with λ. When $(\dot{\gamma}a^2/D\lambda)\ e^{\lambda} < 1$, the suspension dynamics are diffusion limited in the same manner that $\dot{\gamma}a^2/D < 1$ marks the diffusion limited dynamics for Brownian hard-spheres, and the low-shear viscosity is seen.

Note that the low-shear viscosity scales as e^{λ} in both the dispersed and equilibrium flocculated regime, but for different reasons. At small λ the low-shear viscosity increase with λ comes from the pair-distribution function at contact which scales as e^{λ}; the relaxation time is still the bare diffusion time a^2/D, however. Once the flocculated network has formed, the pair distribution function at contact is independent of λ, the relaxation time is the escape time $(a^2/D\lambda)\,e^{\lambda}$, and the viscosity is now set by this escape time.

Kinetically aggregated regime: $\lambda > 10$

In the kinetically aggregated regime, $\lambda > 10$, there is a gradual transition from the high-shear-rate Newtonian behavior to shear thinning as Ma decreases. For $2{\cdot}10^{-5} \leq Ma \leq 10^{-3}$, the suspension viscosity behaves as $Ma^{-\alpha}$, where α varies from 0.9 for $\lambda = 100$, to 1 when $\lambda = 10^{12}$ as shown in table 3. Although for $\lambda \gg 1$ Brownian forces are small compared to polarization forces, Ma is not sufficient to collapse the data over the entire range of shear rate (see figure 2.9). Instead, the viscosity increases with λ at any given Ma below 0.1. At low Ma, neither a low-shear viscosity nor a dynamic yield stress is evident; the low Ma limit has not yet been reached. As discussed above, the low shear limiting behavior occurs when $(\dot{\gamma}a^2/D\lambda)\ e^{U_{min}/kT} < 1$, a very strict requirement for large λ. At present, simulations for smaller Mason numbers are computationally prohibitive, but these suspensions should show a low-shear viscosity.

Comparison to other work

Our simulation results compare well to those of other investigators. Melrose (1992) examined the rheology of an idealized 0.3 volume fraction suspension in the Brownian regime using Brownian dynamics. He neglected all hydrodynamic interactions and modeled the interactions between spheres as a summation of electric point dipoles with a soft core repulsive interaction that scales as r^{-36}, where r is the center to center separation between particles. These simplifications enabled him to model a 3D system. Although this is an advantage since it allows observation of structural

variations along all three spatial directions, the method is accurate only in the dilute limit, at low shear rates, and for low field strengths. In the range studied, $10^{-3} < Ma < 10^{-1}$, Melrose found a shear thinning viscosity that scales as $Ma^{-\alpha}$ where $\alpha < 1$, and that the Mason number does not collapse the data onto a single curve. By the two-thirds rule, our 0.4 area fraction is equivalent to a 0.27 volume fraction and allows comparison to his 0.31 volume fraction studies. figure 2.17 shows that the results compare qualitatively well. Quantitatively, however, Melrose's viscosities are slightly lower in the region of Ma he studied. Note that Melrose's simulations do not explore the low Ma limit and therefore one cannot conclude from his work whether or not there is a low-shear limiting viscosity.

Halsey et al. (1992) studied experimentally a monodisperse 0.1 volume fraction suspension of silica spheres 0.75 micrometers in diameter. They estimated their Mason number ($\equiv 4\pi Ma$) by assigning 1 to the shear rate where a suspension with an applied field of 4000 V/cm has a suspension viscosity equal to the bare suspension viscosity. Here, we estimate Ma from their reported particle size, shear rates, and field strengths. They did not report values for the dielectric constants of the solvent methyl-cyclohexanol and silica spheres, so we use 15 for the solvent (cyclohexanol has a dielectric constant of 15 at 25^oC (CRC handbook of Chemistry and Physics 1993)) and 4 for the silica spheres. It is estimated that Ma varies from 0.01 for a shear rate of $0.1s^{-1}$ to 1.0 for a shear rate of $10s^{-1}$. Halsey et al. found a power law dependence of the viscosity with the shear rate, $\eta \sim \dot{\gamma}^{-\alpha}$, where α ranged from 0.93 to 0.68 for fields from 10^3 V/cm to $4 \cdot 10^3$ V/cm, respectively, or in dimensionless terms, λ on the order

of 10^2 to 10^3. Figure 2.18 compares their $\lambda = 10^2$ results with our $\lambda = 83$ results. Note that Halsey et al.'s experiments were done at Mason numbers larger than those we used to determine the scaling of the low-shear viscosity, accounting for the higher than expected -0.68 slope they reported. Nonetheless, the good comparison between our simulations and Halsey et al.'s experimental results is encouraging.

Unfortunately, there are no data for $\lambda < 30$ with which to compare our results. Sun & Tao's (1995) 0.16 volume fraction simulations do not allow a quantitative comparison. The transition λ for flocculation is a function of volume fraction and Sun & Tao's suspension remained dispersed for $\lambda \leq 30$. Qualitatively, however, they also noted a low-shear viscosity when the suspension remained dispersed that scaled exponentially with λ in agreement with our results for $\lambda < 4$.

2.3.4 The Suspension Dynamics: First Normal Stress Difference

For anisotropic fluids like ER fluids, the suspension viscosity is insufficient to completely characterize the suspension rheology, and the normal stress differences,

$$N_1 \equiv \langle \Sigma_{xx} \rangle - \langle \Sigma_{yy} \rangle \tag{2.27}$$

$$N_2 \equiv \langle \Sigma_{yy} \rangle - \langle \Sigma_{zz} \rangle \,, \tag{2.28}$$

are also needed. Since the normal stresses are not usually design parameters for ER fluids, they are rarely reported. Liang & Xu (1994) reported negative first normal stress difference for fluids with $\lambda \sim O(10^6)$ and Mason numbers from approximately 0.1 to 10^{-5}. Within the shear rates studied, they found that N_1 is independent of

both the shear rate and particle size, and that it scales as the square of the field strength. In short, $N_1/2\epsilon(\beta E)^2$ is constant for $\lambda \sim O(10^6)$ and $10^{-5} < Ma < 0.1$. Bonnecaze (1991) using Stokesian Dynamics also found negative first normal stress differences for the non-Brownian limit, $1/\lambda \equiv 0$, with $N_1/2\epsilon(\beta E)^2$ independent of Ma for $10^{-4} < Ma < 1$.

A negative first normal stress difference represents a compressive stress along the streamlines of a shear flow and a tendency to pull the rheometer plates together, and have been found in lyotropic liquid crystals and certain liquid crystal polymers (Chaffey & Porter 1985). On the other hand, concentrated Brownian hard-sphere suspensions are shown to have a positive first normal stress difference by theoretical considerations (Brady & Vicic 1995) and supported by simulations (Phung et al. 1996). Simulations of Brownian hard-sphere suspensions at modest volume fractions $\phi \sim 0.4$ show a positive first normal stress difference at low shear rates that decays as $\dot{\gamma}^2$ as $\dot{\gamma} \to 0$. As the shear rate increases, N_1 becomes negative and decreases to a constant negative value as $\dot{\gamma} \to \infty$. The sign change is attributed to the hydrodynamic contribution to the stress.

Next, our simulations results for N_1 are presented. Note that the Σ_{zz} component of the stress is not calculated for a monolayer suspension so N_2 cannot be computed. We find that for the dispersed suspension, $\lambda < 4$, $N_1/2\epsilon(\beta E)^2$ is positive and independent of Ma for $10^{-3} < Ma < 0.1$. For the equilibrium flocculated suspension, $4 < \lambda < 10$, $N_1/2\epsilon(\beta E)^2$ is positive and independent of Ma for $5 \cdot 10^{-6} < Ma < 0.1$. The results for the kinetically aggregated regime, $\lambda > 10$, are difficult to interpret.

Generally, computational determination of N_1 is difficult due to large fluctuations in the suspension structure. The results at large λ are particularly sensitive. Nonetheless, we find that N_1 is negative for $\lambda = 8.3 \cdot 10^{12}$ and $Ma < 0.01$, which is consistent with both Liang and Xu (1994) and Bonnecaze (1991) results. For $\lambda = 8.3 \cdot 10^{12}$, N_1 is negative mainly because it is dominated by the negative contribution from the rate of strain or hydrodynamic stress. This is contrary to the dispersed and equilibrium flocculated cases, where at low and moderate shear rate, N_1 is dominated by the interparticle and Brownian stresses.

Results and Discussion

Figure 2.19 shows the first normal stress difference non-dimensionalized by $\eta\dot{\gamma}$ as a function of Ma for λ from 0.8 to $8.3 \cdot 10^{12}$. The corresponding data are given in tables 2.8 to 2.10. Data for the individual components can be found in tables B.4 to B.6 in Appendix B. For $Ma > 1.0$, where viscous forces dominate, $N_1/\eta\dot{\gamma}$ appears to be negative for all λ (tables 2.8 to 2.10), similar to the behavior of Brownian hard-spheres. However, due to the large statistical uncertainties in $N_1/\eta\dot{\gamma}$ for $Ma > 0.1$ as seen in tables 2.8 to 2.10, these results are not conclusive. As Ma decreases, $N_1/\eta\dot{\gamma}$ becomes increasingly positive and appears to be a function of λ.

Of primary interest is the low-shear-rate limiting behavior. A non-zero first normal stress difference results from an asymmetry along the compressive and extensional axes. For Brownian hard-spheres, the asymmetry is induced by shear, and only when the shear rate or Pe is non-zero is the symmetry along the compressive axis broken.

On the other hand, for ER suspensions, even without shear, there is an asymmetry with respect to the compressive axis. The particles form chains aligned along the field direction, and this gives rise to a non-zero first normal stress difference. An ER suspension is expected to have a non-zero first normal stress difference as $\dot{\gamma} \to 0$ and this is borne out by our simulations.

At low shear rates $N_1/\eta\dot{\gamma}$ scales as $1/Ma$, perhaps more clearly seen in figure 2.20 where N_1 is non-dimensionalized electrostatically by $2\epsilon(\beta E)^2$; $N_1/2\epsilon(\beta E)^2$ approaches a constant as $Ma \to 0$ for $\lambda < 10$. The low-shear first normal stress difference depends on λ and will be discussed next within the delineated regimes.

The Dispersed regime: $\lambda < 4$

For $Ma < 0.1$, $N_1/\eta\dot{\gamma}$ scales as $1/Ma$, or conversely, $N_1/2\epsilon(\beta E)^2$ is independent of Ma. This behavior is markedly different from that of Brownian hard-spheres where N_1 scales as $\dot{\gamma}^2$ as $\dot{\gamma} \to 0$. In addition, the simulations indicate that the low-shear limit of the first nomal stress difference is independent of λ, and does not approach 0 as $\lambda \to 0$. A look at the individual contributions from Brownian motion, hydrodynamics, and electrostatics offers more insight into the overall behavior of N_1.

Figure 2.21 shows that the **xF** contribution is negative for all λ studied, its magnitude increases as Ma decreases, and it approaches a low-shear asymptote as $Ma \to 0$, i.e., as $Ma \to 0$, $N_1/2\epsilon(\beta E)^2$ is a constant. The low-shear value of N_1^{xF} scales *exponentially* with λ (figure 2.22) and with the pair potential well depth. This result should not be surprising. As discussed in Appendix A, the **xF** stress scales as the pair

distribution function at contact, $g(2)$, which in turn scales as e^{λ}. The **xF** contribution is negative because the Σ_{yy} stress dominates at low-shear rates due to the attraction along the field direction of the electrostatic force.

Both the Brownian and **SP** contributions oppose the **xF** contribution, acting similar to an interparticle repulsive force. Their sum is plotted in figure 2.21 and their contribution exactly mirrors the **xF** stress. The magnitude of the low-shear limiting value of N_1^{SP+B} also scales exponentially with λ due to the scaling with $g(2)$. The sum of the **SP** and Brownian contributions is positive as the repulsive interaction acts opposite to the attractive electrostatic force to push particles apart.

The hydrodynamic stress is negative for all Ma studied. It is much smaller than the sum of the **xF, B, SP** contributions at low Ma but dominates at large Ma.

Equilibrium flocculated regime: $4 < \lambda < 10$

In the equilibrium flocculated regime, $4 < \lambda < 10$, $N_1/2\epsilon(\beta E)^2$ is constant for $Ma < 10^{-4}$ (figure 2.20). As shown in figure 2.24, the **xF** contribution is negative for all Ma and approaches a low-shear limiting value as $Ma \to 0$. Unlike in the dispersed regime, however, the low-shear value is independent of λ (see figure 2.22).

To predict the low-shear N_1^{xF} for $4 < \lambda < 10$, the particle network is again represented as a single chain of particles aligned along the field direction to which a small strain is applied. The **xF** contribution to the first normal stress difference is simply

$$N_1^{xF} = -n \sum_{\alpha,\beta}^{N} (x_{\alpha\beta} F_x - y_{\alpha\beta} F_y) \,. \tag{2.29}$$

From the interparticle force as the derivative of the pair potential evaluated for two particles contacting each other oriented at an angle θ relative to the field direction, we have

$$N_1^{xF} = -\frac{kT}{a^3}\phi\lambda\frac{9}{8\pi}\left(\sin^2\theta\left(1-5\cos^2\theta\right)-\cos^2\theta\left(3-5\cos^2\theta\right)\right), \tag{2.30}$$

which for small strains, $\lim\theta \to 0$, becomes

$$N_1^{xF} = -\frac{kT}{a^3}\phi\lambda\frac{9}{4}, \tag{2.31}$$

or

$$\frac{N_1^{xF}}{2\epsilon(\beta E)^2} = -\frac{9}{8\pi}\phi. \tag{2.32}$$

Thus we estimate that $N_1^{xF}/2\epsilon(\beta E)^2 \sim \phi$ as $\dot{\gamma} \to 0$ and does not depend on $\dot{\gamma}$ or λ, assuming the particles remain chained. This is supported by our simulation results.

The **xF** contribution to N_1 is balanced by the sum of the **SP** and the Brownian contributions. Similar to the behavior in the dispersed regime, Brownian forces act to oppose the attractive polarization force resulting in a positive contribution to the first normal stress difference. Note also that the low-shear limiting N_1^{SP+B} is independent of λ.

Figure 2.25 shows $N_1^H/\eta\dot{\gamma}$ as a function of Ma. The hydrodynamic contribution is negative for all Ma, decreases as Ma decreases and reaches a minimum at intermediate shear rates. It finally increases for $Ma < 10^{-4}$. A minimum in N_1^H is not seen in the dispersed regime and in Brownian hard-sphere suspensions and can be explained qualitatively by looking at the behavior in the two extremes of shear. Recall that N_1^H measures the hydrodynamic contribution for the rate of strain of the fluid on the

particles. At low shear rates when the suspension is flocculated, we can consider the suspension as a strained chain along the extensional axis. As the shear flow pulls the particles in the chain apart, fluid has to be sucked into the gap between the particles, i.e., the pressure decreases in the gap between the particles resulting in an attractive "force" and a negative first normal stress difference, in a manner similar to depletion flocculation when the soluble dissolved polymer is forced from the gap between two particles. Thus the magnitude of $N_1^H/\eta\dot{\gamma}$ will increase with the osmotic pressure in the gap and should scale as λMa as $\dot{\gamma} \to 0$ (Jeffrey, Morris & Brady 1993). At the other extreme, at high shear rates when the suspension is dispersed, the first normal stress difference scales as $\eta\dot{\gamma}$, or $N_1/\eta\dot{\gamma}$ is a constant. Theoretically, the first normal stress difference for Brownian hard spheres should be zero at very large shear rates as the structure is isotropic with respect to the compressional and extensional axes. For particles with a repulsive force, the first normal stress difference is non-zero but small at very large shear rates since there is some residual anisotropy with respect to the compressional and extensional axes due to the shear (Morris 1996). The behavior for particles with an attractive force is unclear. Calculations of the first normal stress difference at very high shear rates require proper resolution of the hydrodynamic forces in a very thin boundary layer around the particle (Morris 1996). The large errors for N_1 at high shear rates (table 2.9) suggest that it may not be possible to accurately determine N_1 as $Ma \to \infty$ under the simulation conditions employed in this study.

Our physical picture so far shows $-N_1/\eta\dot{\gamma} \sim \lambda\eta\dot{\gamma}$ at low shear rates and $-N_1/\eta\dot{\gamma} \sim$ *constant* at high shear rates. As the suspension moves between these two extremes,

a minimum is produced.

For low to moderate shear rates, $Ma < 0.1$, the Brownian and **SP** stress dominate and the total first normal stress difference is positive. When Ma is very large, the hydrodynamic contribution dominates. To illustrate this, the contributions from the interparticle and Brownian forces as well as the hydrodynamic contribution are plotted for $\lambda = 8.3$ in figure 2.26.

Kinetically aggregated regime: $\lambda > 10$

Determination of N_1 is computationally difficult due to the large fluctuations in the suspension structure, particularly at low shear rates and large λ. In the kinetic regime, $\lambda > 10$, it is statistically difficult to extract a low-shear limiting normal stress from our data. As shown in figure 2.27, there is no apparent plateau, neither at small nor large Ma, especially when the large statistical errors are taken into account (see table 2.10). For $\lambda = 8.3 \cdot 10^{12}$, N_1 is negative for all Ma studied, and for $\lambda = 8.3 \cdot 10^5$, N_1 appears to oscillate from positive to negative over the entire range of Ma. The **xF** contribution is very similar to that for $4 < \lambda < 10$, the equilibrium flocculated regime, and in fact, the scaling analysis presented in the previous section should apply here as well. As shown in figure 2.28, $N_1^{xF}/2\epsilon(\beta E)^2$ has a low-shear plateau that is approximately independent of λ for $10 < \lambda < 8.3 \cdot 10^{12}$. The sum of the **SP** and Brownian contributions, N_1^{SP+B}, (figure 2.28) balances the **xF** contribution. The hydrodynamic contribution, however, is proportionally larger for $\lambda = 8.3 \cdot 10^{12}$ resulting in a negative N_1 for all Mason numbers studied (figure 2.29).

Although the large uncertainties in the results makes quantitative comparisons to experiments unfeasible, qualitatively, the negative first normal stress difference at very large λ agrees with Liang and Xu's (1993) experimental results. Liang and Xu studied a suspension of polyacrylonitrile (PAN) spheres of average diameter $5\mu m$ in a silicone oil forming volume fractions of $0.19, 0.3$, and 0.4. They did not report dielectric constants for the PAN or the silicone oil so corresponding λ and Ma cannot be determined with any certainty. However, using typical values for ϵ_p and ϵ of 2 and 10 respectively (Gast & Zukoski 1989), we estimate that λ is of order 10^6 and that Ma varies from 0.1 to $O(10^{-4})$. Our simulations find a negative first normal stress difference for $\lambda = 8.3 \cdot 10^{12}$ and $Ma < 0.01$ which is consistent with Liang and Xu's results.

2.3.5 The Suspension Dynamics: Antisymmetric Stress

The stress is antisymmetric in ER fluids because of the non-central polarization forces, and generally, $\Sigma_{xy} \neq \Sigma_{yx}$. In this section, the results for Σ_{xy}^{xF} are presented for completeness. Figures 2.30 through 2.32 give plots of $\Sigma_{xy}^{xF}/2\epsilon(\beta E)^2$ as a function of Ma. Corresponding data can be found in tables 2.11 through 2.13.

We find that at high shear rates, $Ma \geq 1$, Σ_{xy}^{xF} is negative for all λ studied. The antisymmetric stress corresponds to a net torque exerted on the material. There is no torque on an individual spherical particle, but there is a net torque on a strained chain of particles. To understand the behavior, we take a simple pair-wise approach and calculate the xy component of the stress as a function of the angle of orientation of a particle pair. From the interparticle force as the derivative of the pair potential

evaluated for two particles contacting each other oriented at an angle θ relative to the field direction, we have

$$\frac{\Sigma_{xy}^{xF}}{2\epsilon(\beta E)^2} \propto \phi \sin\theta \cos\theta \left(3 - 5\cos^2\theta\right). \tag{2.33}$$

Figure 2.33 shows a schematic of the regions of orientation where Σ_{xy}^{xF} changes sign from positive to negative. The contribution from pairs in sections $2, 3, 6$, and 7 are larger than pairs in sections $1, 4, 5$, and 8.

For all λ, at high shear rates when the suspension is dispersed, the shear flow tends to align the particles along the compressional axis, and results in a negative contribution to the xy stress. As an example, a plot of $g(2, \theta)$, averaged over the entire simulation, as a function of θ is shown in figure 2.34, and shows a preference of pairs aligned in section 8 where the Σ_{xy}^{xF} is negative.

As the shear rate decreases, Σ_{xy}^{xF} is a strong function of λ. In the dispersed regime, $\lambda < 3.3$, Σ_{xy}^{xF} is negative and approaches an asymptote at low shear rates. Unfortunately, a plot of $g(2, \theta)$ offers very little explanation in this case (figure 2.35). The structure seems symmetric about the electric field direction which would yield zero xy stress. However, a slight asymmetry due to the shear could result in a negative contribution to Σ_{xy}^{xF}. In contrast to the negative Σ_{xy}^{xF} for $\lambda < 3.3$, for $\lambda = 3.3$, Σ_{xy}^{xF} is positive at intermediate shear rates. The small chains formed at $\lambda = 3.3$ rotate in a clockwise direction due to the shear flow and so a typical particle pair lies in section 1 yielding a positive Σ_{xy}^{xF} (similar to the behavior seen for the equilibrium flocculated regime at moderate shear rates described below.)

In the flocculated regimes, Σ_{xy}^{xF} is positive at moderate shear rates, $5 \cdot 10^{-5} <$

$Ma < 1$, as shown in figures 2.31 and 2.32. To understand the behavior of Σ_{xy}^{xF} in these regimes, we again turn to figure 2.33 that gives a schematic of the sign changes for a particle pair as a function of orientation relative to the electric field. Under flow, the particle chains become strained and tend to lie mainly in the first quadrant, resulting in a positive contribution to Σ_{xy}^{xF} (figure 2.36). For $\lambda = 4.2, 5,$ and5.8, the xy component of the stress becomes negative at low shear rates. Again, unfortunately the $g(2, \theta)$ plots shed little light on this phenomenon; as seen in figure 2.37, the structure is roughly hexagonal (note the four small peaks at $60^o, 120^o, 210^o$, and 330^o), and symmetric about the electric field direction, which should result in Σ_{xy}^{xF} identically 0. However, small a asymmetry due to the flow, not easily discernible in figure 2.37, can result in a negative Σ_{xy}^{xF}.

2.4 Conclusions

In this chapter, we presented the results of a study of the dynamics and structure of dielectrically interacting particles forming an ER fluid. The nature of the static, non-sheared structure is governed by λ, the ratio of the polarization to Brownian forces, which equals the pair potential well-depth for point dipoles in contact aligned along the field. We found that a 0.4 area fraction suspension remains dispersed when $\lambda < 4$. Here the short-time diffusivity was found to be anisotropic with D_{yy} smaller than D_{xx}. This is due to the formation of pairs of particles along the field direction that translate for short times in the **y** direction as a single rod decreasing the mobility in the **y** direction. The long-time diffusivity was found to scale inversely with the pair

distribution function at contact in agreement with the predictions by Brady (1994). For $4 < \lambda < 10$, there is an equilibrium flocculated regime where particles order into a hexagonal structure. Here the short-time diffusivity is smaller than that for the dispersed regime due to the formation of larger clusters. The diffusivity is slightly less anisotropic than in the dispersed regime since clusters are now formed in the **x** direction as well as along the field or **y** direction. For $\lambda > 10$, the suspension is kinetically flocculated. The short-time diffusivity here is only slightly anisotropic as the close packed structure severely decreases mobilities in both the **x** and **y** directions. The long relaxation times for the flocculated regimes, $\lambda > 4$, precluded determination of a long-time diffusivity.

The suspension viscosity was described in terms of λ and the Mason number, Ma, that gives the ratio of the viscous to polarization forces. Both the dispersed and weakly flocculated suspensions, $\lambda < 10$, have a low-shear viscosity that scales exponentially with λ but for different reasons. In the dispersed regime, $\lambda < 4$, the scaling can be predicted from a regular perturbation analysis of the equilibrium structure. The low-shear viscosity scales with the equilibrium pair-distribution function at contact, which in turn scales as $g_{HS}\, e^{\lambda}$, where g_{HS} is the hard-sphere value.

In the equilibrium flocculated regime, $4 < \lambda < 10$, a simple model based on linear viscoelastic theory shows that the low-shear viscosity is given as the product of the shear modulus and a relaxation time. The major contribution to the stress comes from the polarization forces and thus the shear modulus scales as λ. It is the relaxation time scale that is responsible for the exponential scaling of the low-

shear viscosity; since the particles are aggregated, the time scale for escape from their mutual potential wells is the time scale $(a^2/D\lambda)e^{U_{min}/kT}$. The attractive potential well depth, U_{min}/kT, scales with but is not precisely λ for two reasons. Firstly, the induced particle dipole has contributions from neighboring particles, an effect that is accounted for in the simulation but is not captured with the isolated point dipole model. Secondly, the electrostatic potential is orientation dependent. Particle pairs at an angle to the electric field have a lower potential well depth compared to particle pairs aligned along the field, and will escape preferentially. Thus we found that the low-shear viscosity obeys the curve $\eta_0/\eta = 0.16\ e^{1.57\lambda}$ in the equilibrium flocculated regime.

The ratio of the escape time and the shear time scale gives a new dimensionless number, $(\dot{\gamma}a^2/D\lambda)e^{\lambda}$, and the low-shear viscosity is observed when $\dot{\gamma} \ll (D/a^2)\lambda e^{-1.88\lambda}$. When the reduced viscosity is plotted as a function of the new shear rate, a single universal curve is obtained. For $\lambda > 10$, we did not see a low-shear viscosity, but the shear rates we were able to achieve were not low enough to observe the low-shear limiting behavior.

Results for the first normal stress difference and xy stress were also presented. Due to the anisotropy of the ER suspension, the first normal stress difference does not decay with the shear rate. In the dispersed regime, $\lambda < 4$, the first normal stress difference is positive and independent of the Mason number for $10^{-3} < Ma < 0.1$. For the equilibrium flocculated suspension, $4 < \lambda < 10$, the first normal stress difference is also positive and approaches a non-zero low-shear limit that is independent of λ. For

both the dispersed and equilibrium flocculated suspensions, there is a hydrodynamic dominated regime for $Ma > 0.1$ where N_1 appears to be negative. For the kinetically aggregated regime, $\lambda > 10$, large fluctuations in the suspension structure precludes quantitative analysis of the results. We do, however, find that the first normal stress difference is negative for $\lambda = 8.3 \cdot 10^{12}$ and $Ma < 0.01$, which is consistent with the experimental results of Liang and Xu (1994) and the simulation results of Bonnecaze (1991).

2.5 Tables

Table 2.1: The short-time and rotational diffusivities for $0.8 \leq \lambda \leq 8.3 \cdot 10^{12}$.

λ	D_{xx}	D_{yy}	D_0^s	D_0^r
0.8	0.580 ± 0.017	0.554 ± 0.022	0.567 ± 0.022	0.795 ± 0.029
1.7	0.583 ± 0.021	0.532 ± 0.023	0.558 ± 0.019	0.773 ± 0.029
2.5	0.564 ± 0.022	0.475 ± 0.023	0.519 ± 0.02	0.713 ± 0.033
3.3	0.551 ± 0.033	0.427 ± 0.028	0.489 ± 0.028	0.672 ± 0.038
4.2	0.519 ± 0.054	0.366 ± 0.044	0.442 ± 0.048	0.600 ± 0.057
5.0	0.497 ± 0.028	0.361 ± 0.0287	0.429 ± 0.027	0.569 ± 0.045
5.8	0.321 ± 0.062	0.246 ± 0.02	0.283 ± 0.041	0.324 ± 0.036
8.3	0.362 ± 0.035	0.267 ± 0.022	0.314 ± 0.028	0.441 ± 0.038
17.0	0.341 ± 0.012	0.258 ± 0.008	0.299 ± 0.01	0.393 ± 0.021
83.0	0.321 ± 0.062	0.246 ± 0.02	0.283 ± 0.041	0.324 ± 0.036
830	0.264 ± 0.068	0.231 ± 0.020	0.247 ± 0.044	0.240 ± 0.035
$8.3 \cdot 10^5$	0.237 ± 0.060	0.226 ± 0.020	0.231 ± 0.040	0.141 ± 0.029
$8.3 \cdot 10^{12}$	0.228 ± 0.042	0.216 ± 0.003	0.222 ± 0.022	0.118 ± 0.021

Table 2.2: The long-time diffusivity for the dispersed regime, $\lambda < 4$.

λ	D^s_∞
0.8	0.583 ± 0.055
1.7	0.540 ± 0.220
2.5	0.367 ± 0.157
3.3	0.348 ± 0.126

Table 2.3: The suspension viscosity for the dispersed regime, $\lambda < 4.0$. Statistical information is omitted where sampling is insufficient to produce meaningful standard deviations.

Ma	λ			
	0.8	1.7	2.5	3.3
10^{-4}				20.4
0.0002		3.75 ± 0.1	5.5	15.7 ± 13.5
0.001	2.55	3.27	5.9 ± 2.6	18.6 ± 7.9
0.005			4.4 ± 1.1	7.0 ± 4.3
0.01	2.60 ± 2.3	2.3 ± 1.5	3.6 ± 1.5	4.4 ± 1.7
0.1	2.4 ± 0.2	2.6 ± 0.5	2.6 ± 0.2	2.5 ± 0.2
1.0	2.3 ± 0.1	2.3 ± 0.1	2.3 ± 0.1	2.3 ± 0.2

Table 2.4: The suspension viscosity for the equilibrium flocculated regime $4 < \lambda < 10$. Statistical information is omitted where sampling is insufficient to produce meaningful standard deviations.

Ma	λ			
	4.2	5.0	5.8	8.3
$5 \cdot 10^{-6}$			1870	
$2 \cdot 10^{-5}$	211 ± 12.0	359 ± 144	1250 ± 136	1310 ± 342
10^{-4}	127 ± 21.9	250 ± 48.8	292 ± 17.0	353 ± 20.9
0.0002	72.1 ± 9.3	134 ± 18.6	155 ± 42.4	
0.001	30.2 ± 3.8	37.0 ± 2.2	45.6 ± 9.3	46.6 ± 4.9
0.01	4.2 ± 1.6	5.9 ± 2.1	7.2 ± 2.1	10.2 ± 0.3
0.1	2.5 ± 0.3	2.5 ± 0.3	2.5 ± 0.2	2.6 ± 0.4
1.0	2.3 ± 0.1	2.3 ± 0.1	2.3 ± 0.1	2.3 ± 0.1
10	2.3 ± 0.1	2.3 ± 0.1	2.3 ± 0.1	2.3 ± 0.1
100	2.3 ± 0.1	2.3 ± 0.1	2.3 ± 0.1	2.3 ± 0.1

Table 2.5: The suspension viscosity for the kinetically flocculated regime, $\lambda > 10$.

Ma	λ				
	17	83.0	830	$8.3 \cdot 10^5$	$8.3 \cdot 10^{12}$
$2 \cdot 10^{-5}$	1487 ± 108	1990 ± 123	2620 ± 173	2500 ± 747	7260 ± 2430
10^{-4}	389 ± 154	594 ± 70.1	582 ± 27.6	696 ± 92.7	1160 ± 122
0.0005	92.6				
0.001	44.9 ± 16.7	83.4 ± 1.2	91.2 ± 1.1	125 ± 31.9	195 ± 63.5
0.005	23.1 ± 6.7				
0.01		14.4 ± 0.3	18.9 ± 2.1	20.4 ± 1.9	23.9 ± 3.5
0.05	3.6 ± 0.5				
0.1		3.0 ± 0.6	3.4 ± 0.1	3.5 ± 0.3	3.8 ± 0.1
0.5	2.3 ± 0.1				
1.0	2.3 ± 0.114	2.3 ± 0.1	2.3 ± 0.1	2.3 ± 0.1	2.4 ± 0.1

Table 2.6: The suspension viscosity for $\lambda = \infty$ (Bonnecaze and Brady (1992a)).

Ma	$\lambda = \infty$
10^{-4}	1250 ± 60.8
0.0002	544 ± 29.8
0.001	120 ± 20.1
0.01	22.1 ± 1.1
0.1	3.43 ± 0.1
1.0	2.4 ± 0.1

Table 2.7: Exponents for the viscosity dependence for $2 \cdot 10^{-5} \leq Ma \leq 10^{-3}$.

λ	Δ
∞	1.0
$8.3 \cdot 10^{12}$	1.0
$8.3 \cdot 10^{5}$	0.9
830	0.9
83	0.9
8.3	0.9

Table 2.8: The suspension first normal stress difference for the dispersed regime, $\lambda < 4$. Statistical information is omitted where sampling is insufficient to produce meaningful standard deviations.

Ma	λ			
	0.8	1.7	2.5	3.3
10^{-4}				300
0.0002		175 ± 18.0	156	150 ± 19.5
0.001	39.1	28.9	29.0 ± 16.6	34 ± 5.58
0.005			7.21 ± 1.4	5.15 ± 10.4
0.01	2.55 ± 0.525	3.30 ± 0.045	2.28 ± 5.0	3.84 ± 4.74
0.1	0.369 ± 0.020	0.261 ± 0.360	0.228 ± 0.437	0.083 ± 0.414
1.0	-0.047 ± 0.230	-0.015 ± 0.150	0.020 ± 0.210	0.024 ± 0.250
10			-0.029 ± 0.199	-0.092 ± 0.237
100			-0.076 ± 0.248	-0.072 ± 0.237

Table 2.9: The suspension first normal stress difference for the equilirium flocculated regime, $4 < \lambda < 10$. Statistical information is omitted where sampling is insufficient to produce meaningful standard deviations.

Ma	λ			
	4.2	5.0	5.8	8.3
$5 \cdot 10^{-6}$			20800	
$2 \cdot 10^{-5}$	2100 ± 313	4200 ± 134	4700 ± 381	4800 ± 105
10^{-4}	551 ± 2.9	998 ± 106	1010 ± 125	371 ± 78.5
0.0002	359 ± 49.0	278 ± 53.2	297 ± 162	
0.001	43.7 ± 28.6	17.3 ± 13.0	21.5 ± 12.5	47.2 ± 15.2
0.01	2.78 ± 5.08	1.66 ± 5.58	1.31 ± 4.8	2.09 ± 0.18
0.1	-0.06 ± 0.567	-0.045 ± 0.630	-0.069 ± 0.490	-0.155 ± 0.343
1.0	0.024 ± 0.294	0.018 ± 0.370	0.011 ± 0.278	-0.012 ± 0.27
10	-0.054 ± 0.243	-0.06 ± 0.244	-0.065 ± 0.245	-0.073 ± 0.246
100	-0.072 ± 0.237	-0.072 ± 0.237	-0.071 ± 0.237	-0.071 ± 0.237

Table 2.10: The suspension first normal stress difference for the kinetically flocculated regime $\lambda > 10$. Statistical information is omitted where sampling is insufficient to produce meaningful standard deviations.

Ma	λ				
	17	83.0	830	$8.3 \cdot 10^{-5}$	$8.3 \cdot 10^{12}$
$2 \cdot 10^{-5}$	6750 $\pm$3160	4490 $\pm$2100	3420 $\pm$2570	-2761 $\pm$2430	-6550 $\pm$4640
10^{-4}	402 ± 377	718 ± 421	239 ± 993	543 ± 318	-450 ± 110
0.0005	2.3				
0.001	29.1 ± 18.7	36.6 ± 22.7	59.0 ± 14.1	-26.1 ± 12.7	-232 ± 204
0.005	11.5 ± 5.74				
0.01		2.63 ± 1.08	3.79 ± 0.100	1.39 ± 1.02	0.810 ± 6.97
0.05	0.589 $\pm$0.726				
0.1		0.169 $\pm$0.069	0.329 $\pm$0.517	-0.071 $\pm$0.222	-0.986 $\pm$0.420
0.5	-0.056 $\pm$0.305				
1.0	-0.062 ± 0.31	-0.139 $\pm$0.100	-0.149 $\pm$0.011	-0.170 $\pm$0.221	-0.536 $\pm$0.151

Table 2.11: The **xF** contribution to σ_{12} normalized by $\eta\dot{\gamma}$ for the dispersed regime $\lambda < 4$. Statistical information is omitted where sampling is insufficient to produce meaningful standard deviations.

Ma	λ			
	0.8	1.7	2.5	3.3
10^{-4}				-136
0.0002		-67.5 ± 0.025	-79.3	-62.7 ± 28.9
0.001	-10.5	-11.0	-12.6 ± 3.00	9.17 ± 9.40
0.005			-1.36 ± 5.62	6.51 ± 6.8
0.01	-1.50 ± 0.019	-2.20 ± 0.024	-0.400 ± 1.00	1.53 ± 2.90
0.1	-0.180 ± 0.021	-0.143 ± 0.021	0.002 ± 0.22	-0.071 ± 0.170
1.0	-0.001 ± 0.024	-0.019 ± 0.021	-0.020 ± 0.023	-0.020 ± 0.030

Table 2.12: The **xF** contribution to σ_{12} normalized by $\eta\dot{\gamma}$ for the equilibrium flocculated regime $4 < \lambda < 10$. Statistical information is omitted where sampling is insufficient to produce meaningful standard deviations.

Ma	λ			
	4.2	5.0	5.8	8.3
$5 \cdot 10^{-6}$			-26700	
$2 \cdot 10^{-5}$	-580 ± 89.8	-619 ± 110	1540 ± 275	1390 ± 129
10^{-4}	77.1 ± 35.8	348 ± 167	581 ± 18.6	611 ± 112
0.0002	61.3 ± 9.3	101 ± 79.9	223 ± 106	
0.001	55.4 ± 2.70	46.7 ± 9.6	63.5 ± 22.8	73.7 ± 11.6
0.01	-0.730 ± 3.40	5.12 ± 2.40	0.130 ± 0.200	9.61 ± 0.12
0.1	-0.021 ± 0.300	0.006 ± 0.23	0.359 ± 2.89	0.381 ± 0.010
1.0	-0.021 ± 0.033	-0.020 ± 0.030	-0.022 ± 0.030	-0.017 ± 0.030

Table 2.13: The **xF** contribution to σ_{12} normalized by $\eta\dot{\gamma}$ for the kinetically flocculated regime $\lambda > 10$. Statistical information is omitted where sampling is insufficient to produce meaningful standard deviations.

Ma	λ				
	17.0	83.0	830	$8.3 \cdot 10^5$	$8.3 \cdot 10^{12}$
$2 \cdot 10^{-5}$	3520 ± 871	3490 ± 93.4	5250 ± 87.9	3290 ± 993	2390 ± 366
10^{-4}	664 ± 101	1060 ± 377	989 ± 110	994 ± 111	458 ± 57.7
0.0005	156				
0.001	53.3 ± 4.9	125 ± 38.9	125 ± 56.2	126 ± 27.7	49.3 ± 4.90
0.005	23.8 ± 10.1				
0.01		15.1 ± 5.9	17.7 ± 2.4	17.2 ± 2.9	8.07 ± 2.0
0.05	1.45 ± 0.53				
0.1		0.382 ± 0.38	0.403 ± 0.1	0.322 ± 0.07	0.990 ± 0.34
0.5	-0.025 ± 0.06				
1.0	-0.018	-0.01	0.012	0.002	0.015
1.0	± 0.04	± 0.42	± 0.003	± 0.013	± 0.023

2.6 Figures

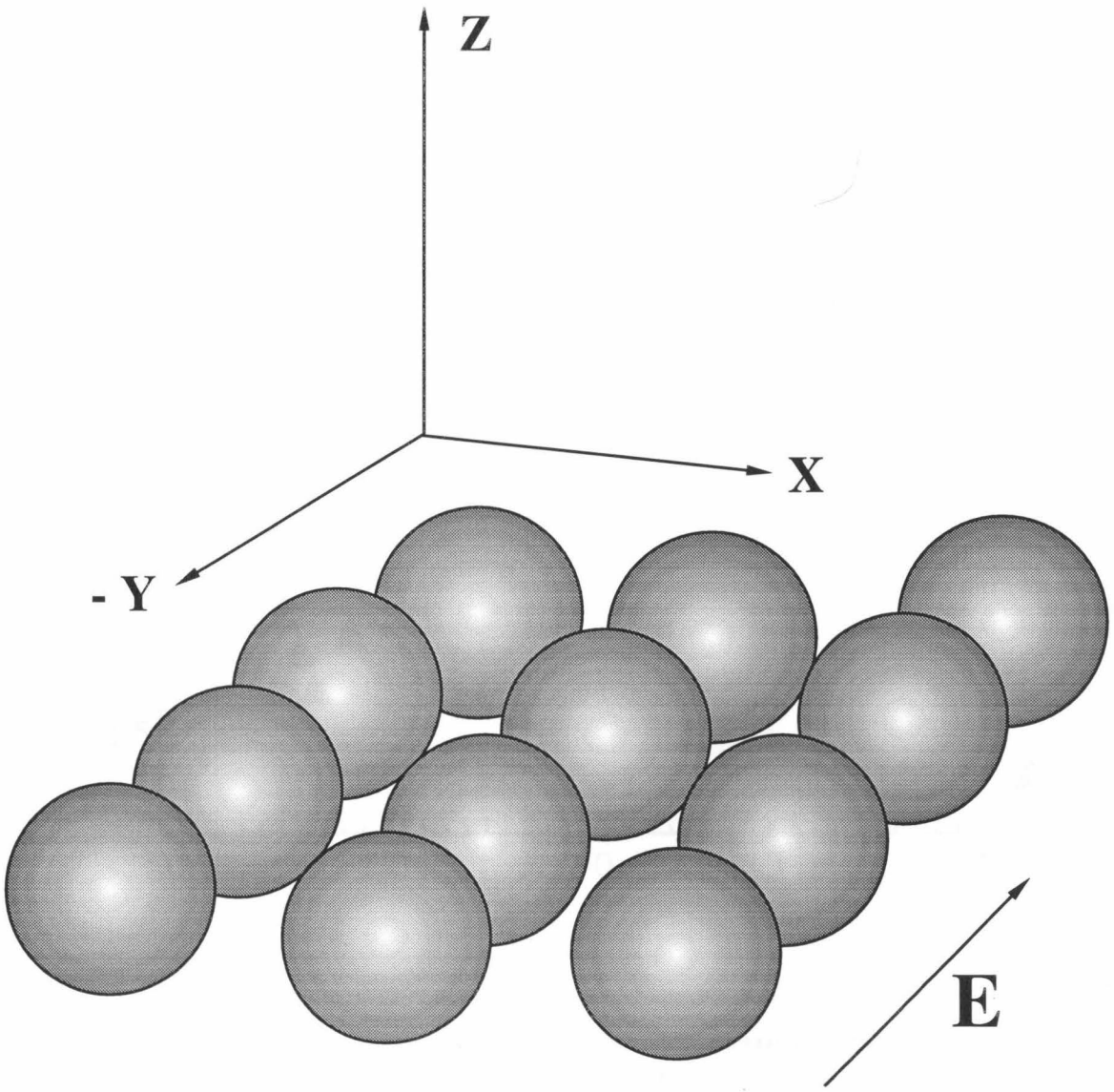

Figure 2.1: Illustration of the monolayer used for the simulations. The electric field is in the y-direction, while the velocity is in the x-direction with gradient in the y-direction.

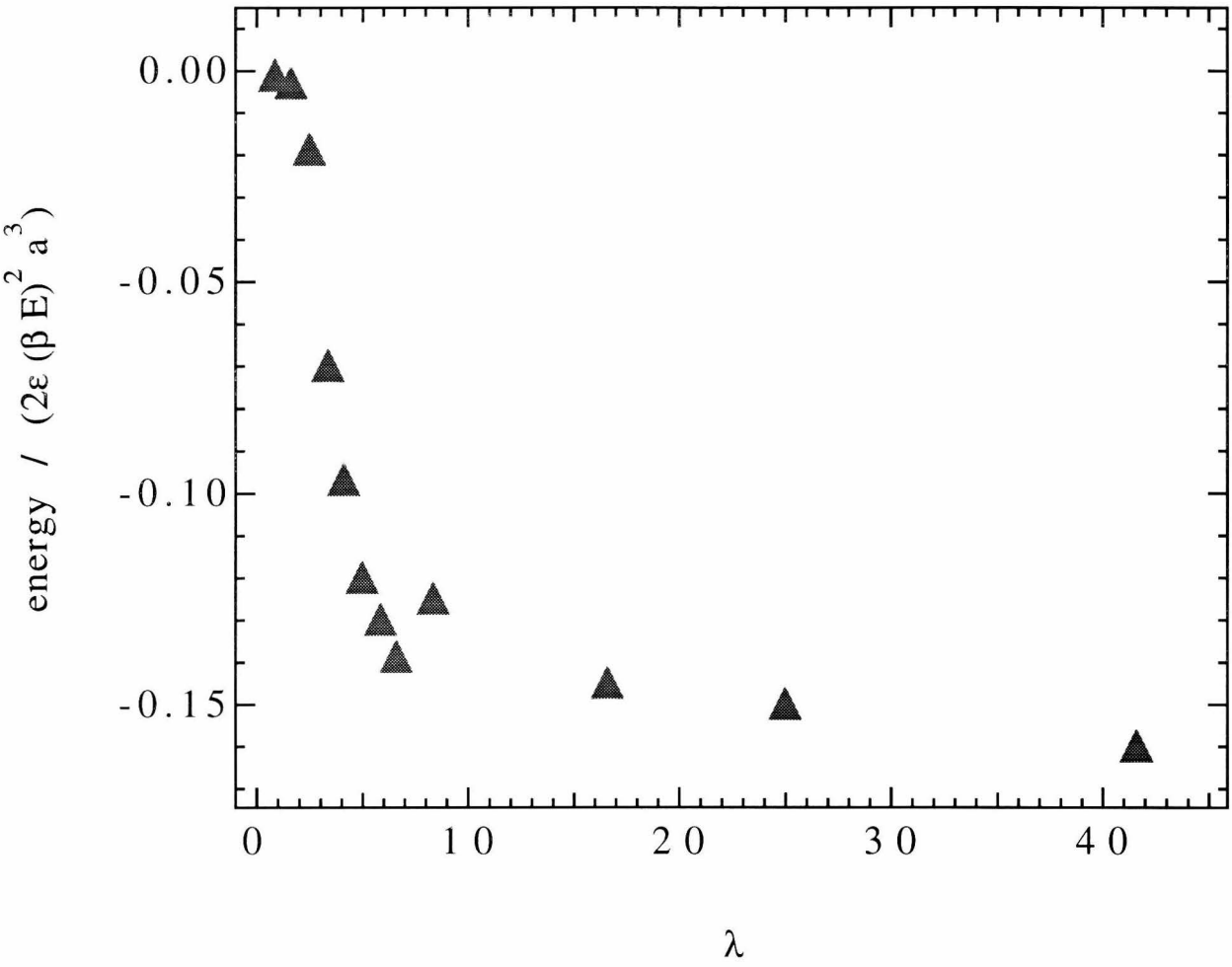

Figure 2.2: The electrostatic energy of the suspension at steady state as a function of the ratio of polarization to thermal forces, λ. As the suspension forms chains aligned with the field, the energy decreases. There is an asymptote above $\lambda = 5.8$ where the particles have aggregated into a single structure with a hexagonal lattice order. For $\lambda > 5.8$, the hexagonal structure has vacancies in the lattice.

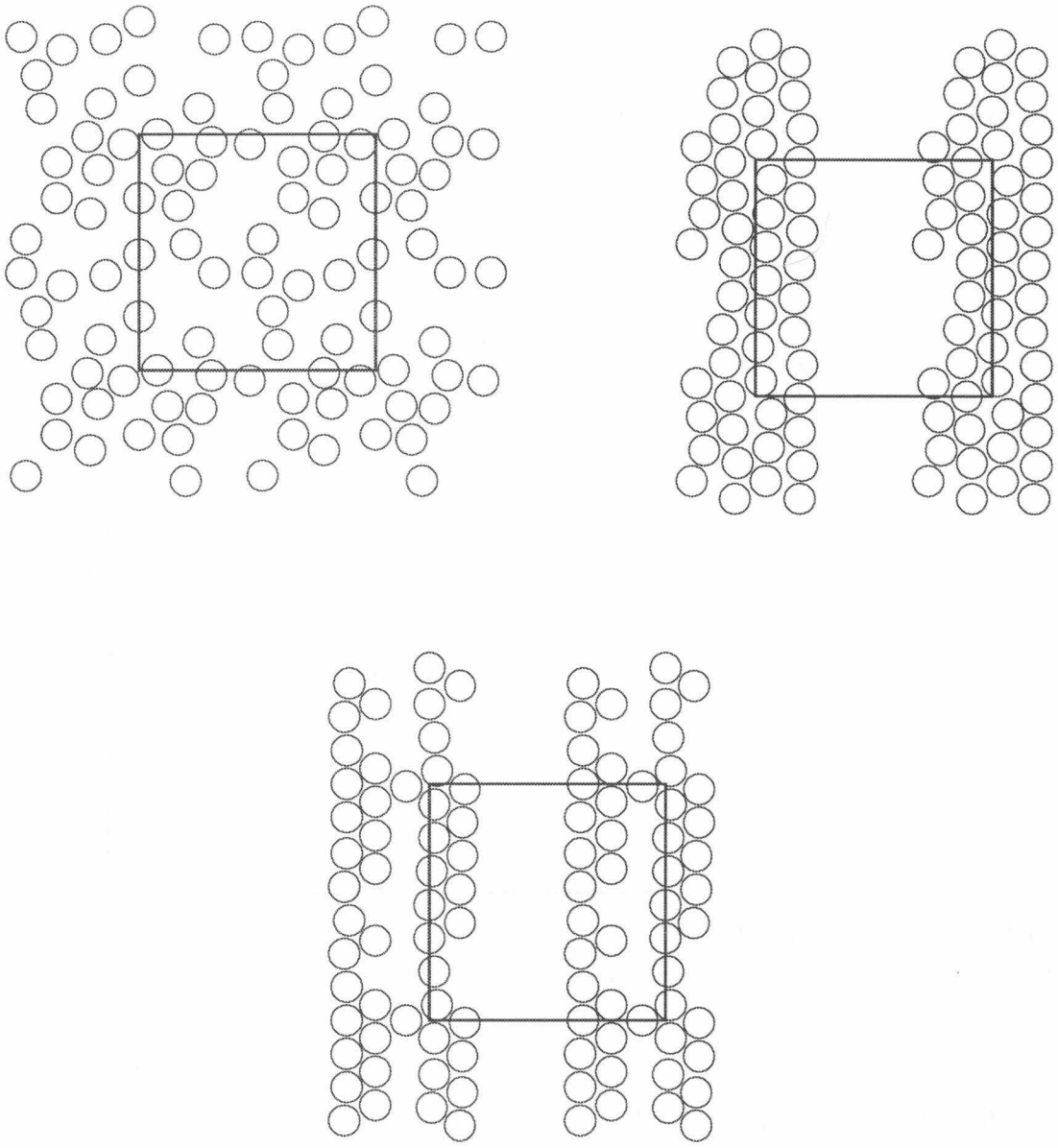

Figure 2.3: Clockwise from top left: instantaneous snapshots of the structure for $\lambda = 0$, 5.8, and 17. At $\lambda = 0.8$ few particles aggregate temporarily and align along the field direction. At $\lambda = 5.8$ all particles have aggregated into a single column with a hexagonal lattice order but particles still fluctuate within the lattice. A further increase in λ results in the kinetically aggregated open structure.

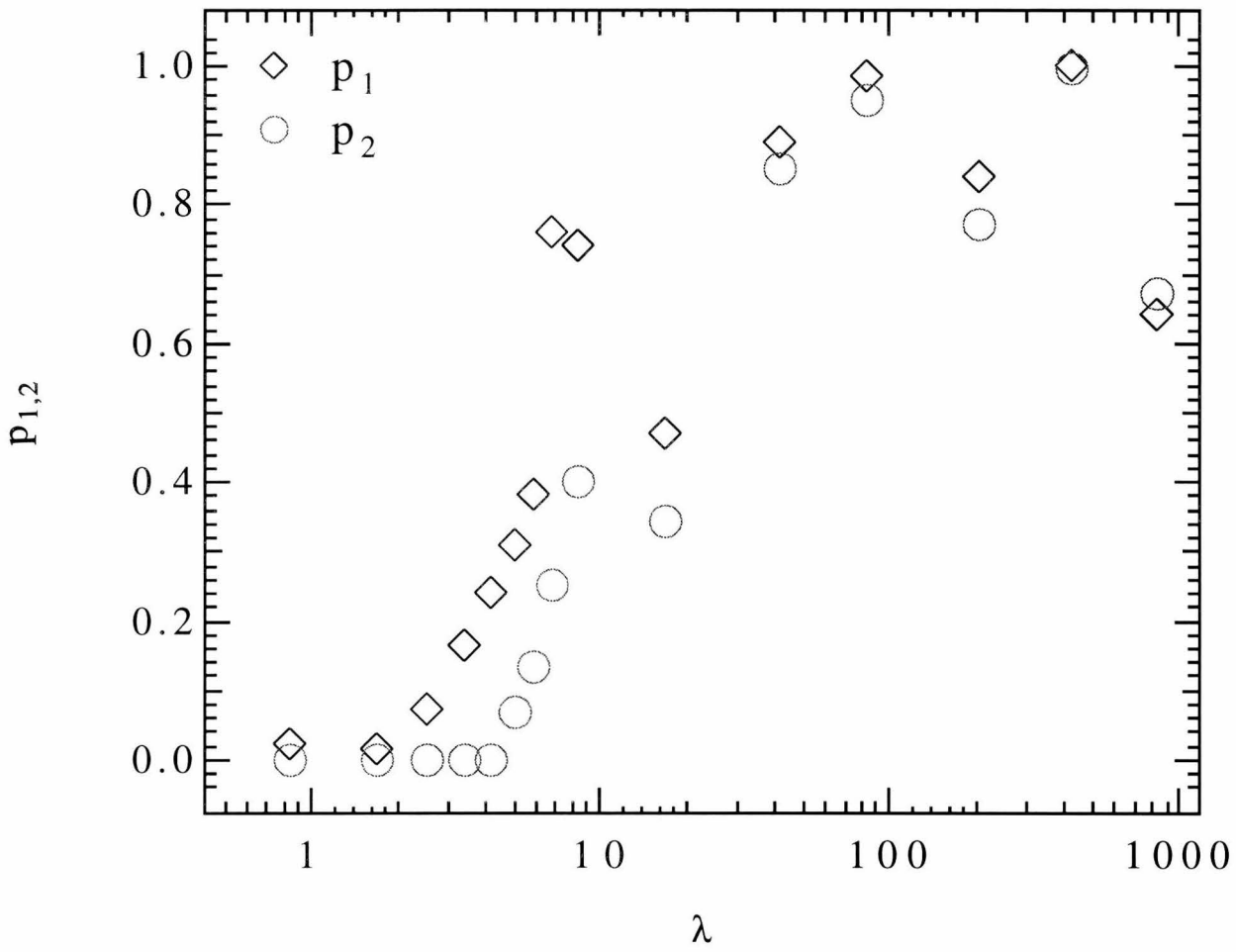

Figure 2.4: The order parameters p_1 and p_2 versus λ; $p_1 = p_2 = 1$ for a hexagonal lattice and zero for a random dispersion. For $\lambda > 0.8$, p_1 is greater then 0 indicating a preference for particle pairs to align along the field direction. An increase in p_2 indicates coalescence of chains. For $\lambda > 10$ both order parameters are approaching, but less than, 1 because the structure is arrested in a kinetically controlled open network.

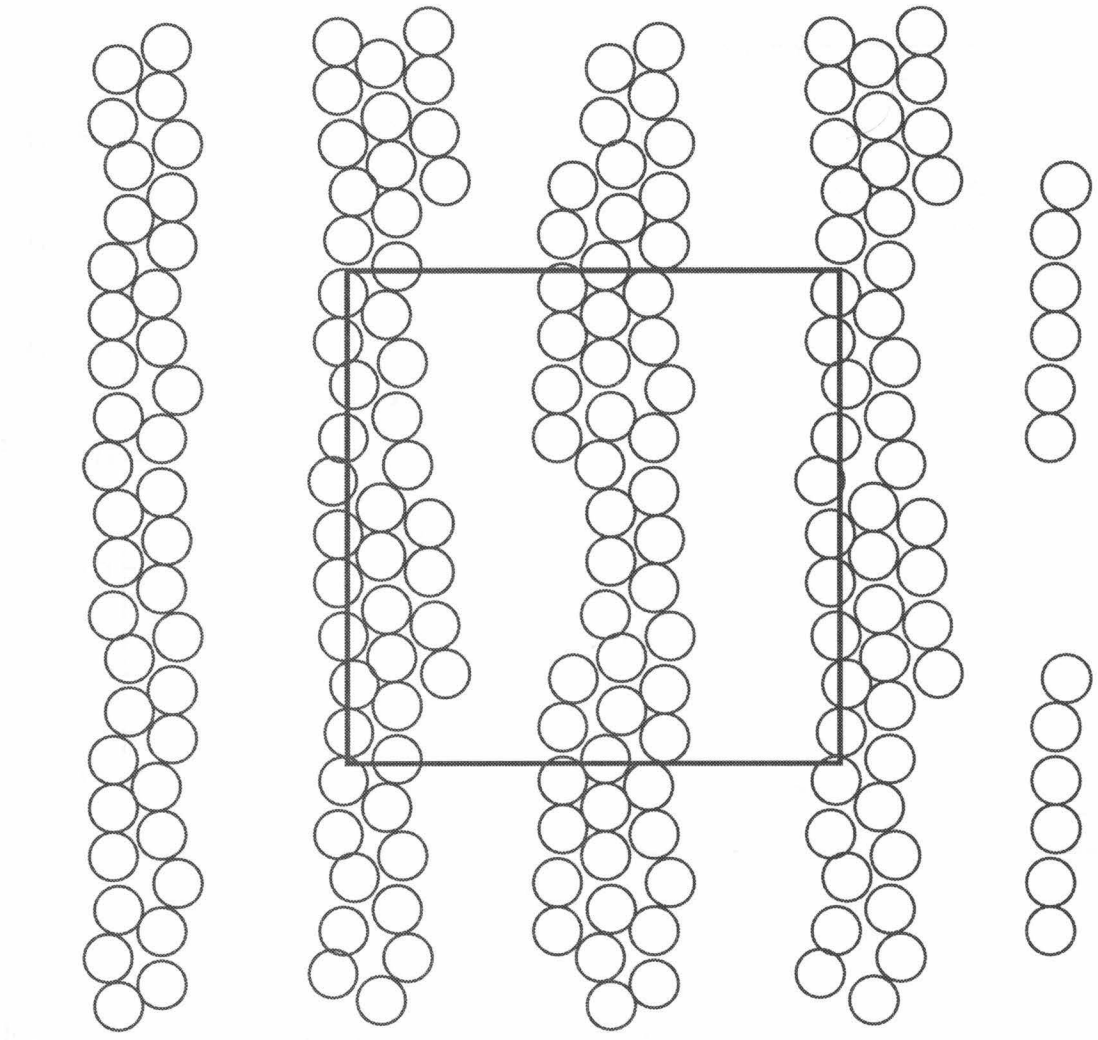

Figure 2.5: The steady state structure for $\lambda = 5.8$ with 50 particles. The columns have a hexagonal structure but have not coalesced into a single column.

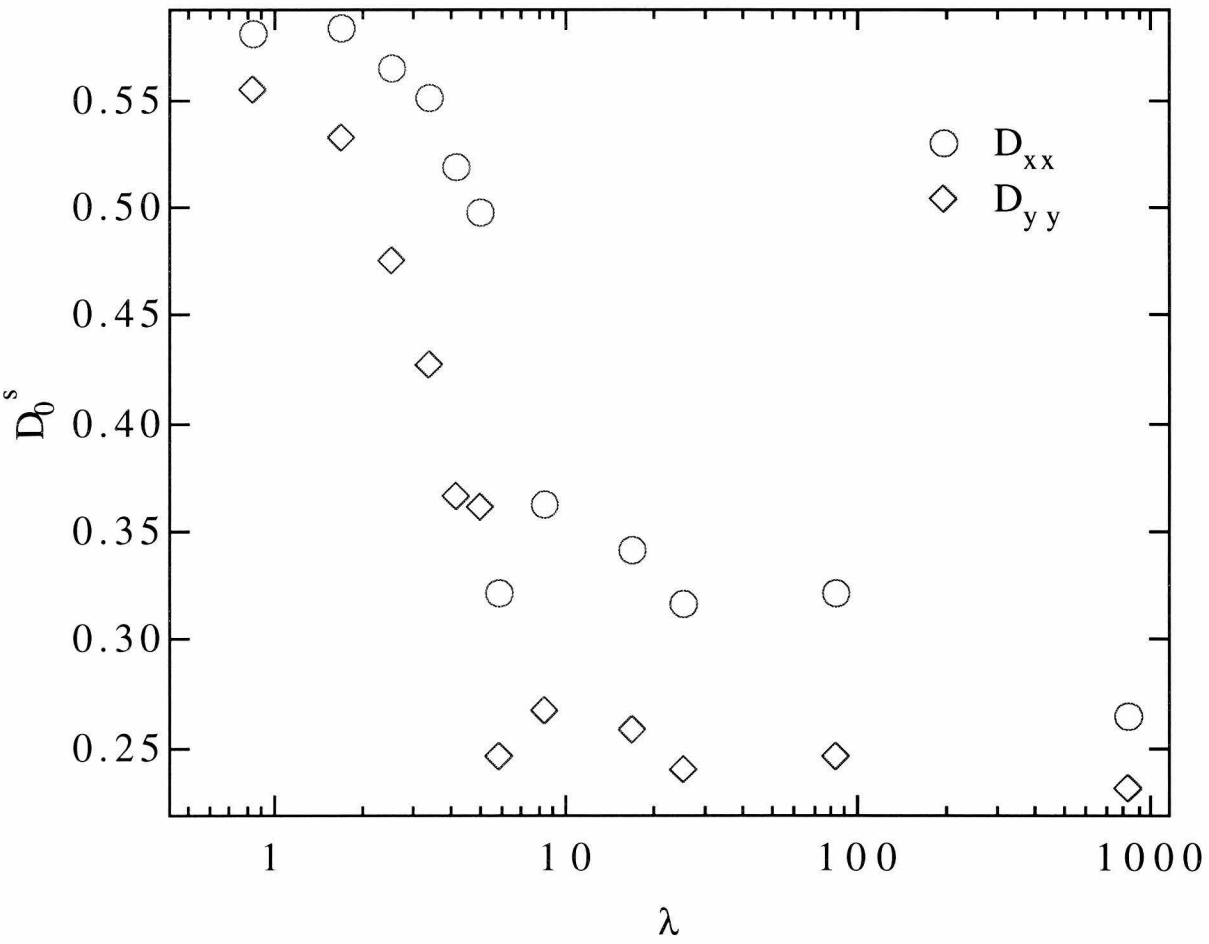

Figure 2.6: The **xx** and **yy** components of the short-time self diffusivity for $0.8 \leq \lambda < 1000$. The short-time self diffusivity decreases with an increase in λ, and is anisotropic in the dispersed and equilibrium flocculated regimes.

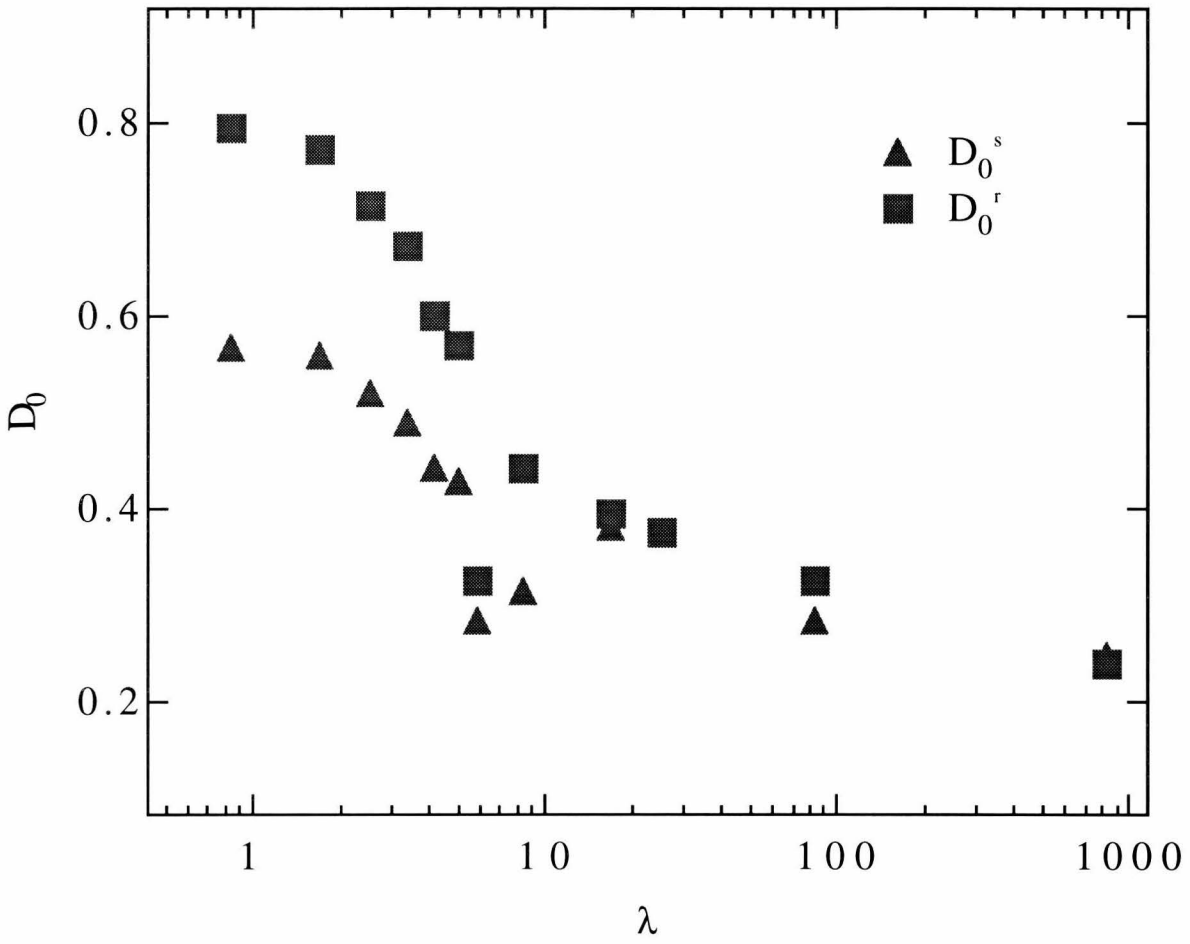

Figure 2.7: The short-time and rotational diffusivities $D_0^{s,r}$ as a function of λ. D_0^s is an average of the **xx** and **yy** components. In the dispersed regime, $\lambda < 4$, D_0^r varies very little with λ, decreasing from 0.57 to 0.51. As λ increases and the suspension becomes flocculated, the short time diffusivity drops dramatically and approaches a constant for $\lambda > 100$ as the clusters become more tightly packed.

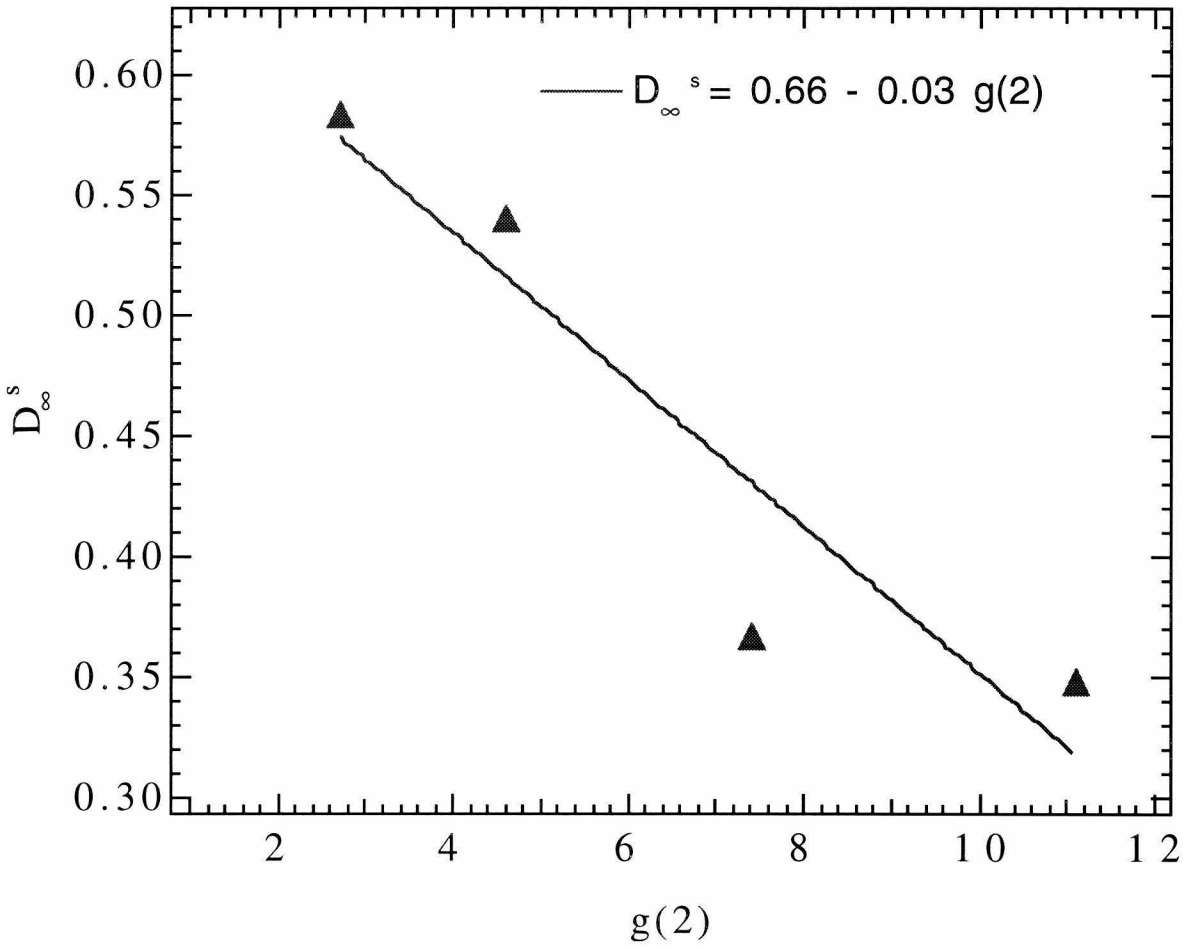

Figure 2.8: The long-time diffusivity, D^s_∞, as a function of λ for the dispersed regime. D^s_∞ is an average of the **xx** and **yy** components. The long-time diffusivity scales inversely with the pair distribution function at contact in agreement with the predictions by Brady (1994).

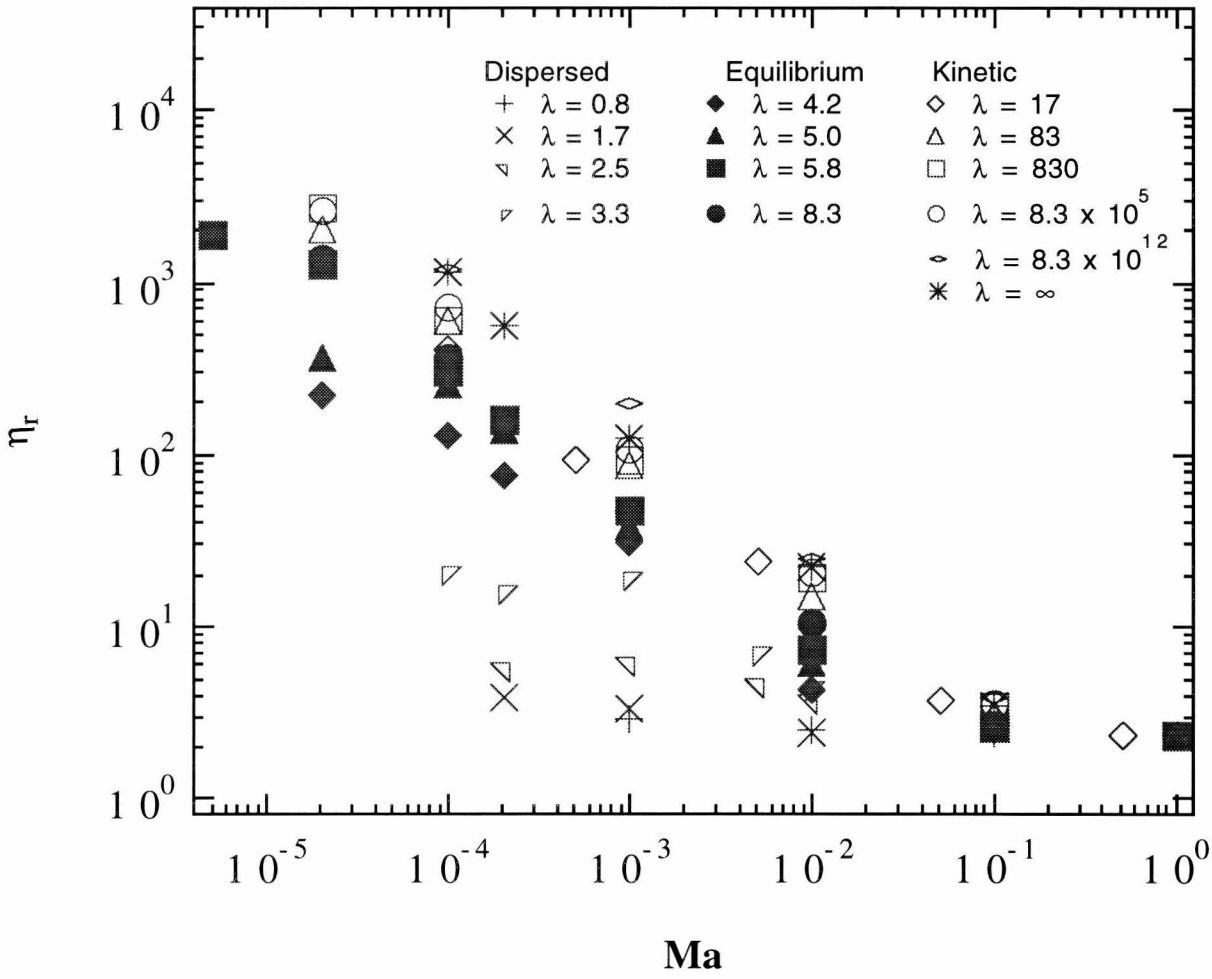

Figure 2.9: The suspension viscosity relative to the solvent viscosity as a function of Ma for $0.8 \leq \lambda \leq \infty$. The Mason number collapses the data only at very high shear rates.

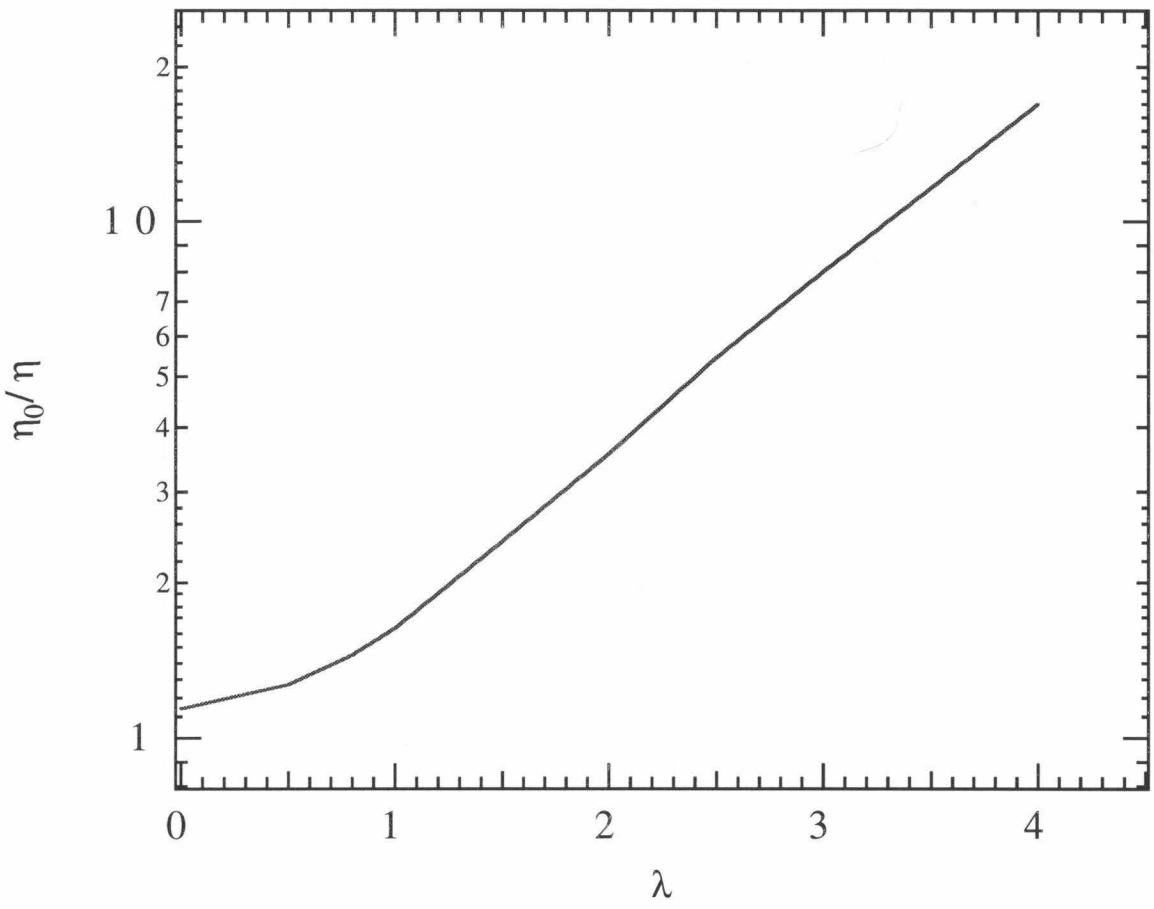

Figure 2.10: The low-shear viscosity, $\eta_0 = 1 + \eta_H + \eta_{HS} + \eta_{ER}$, estimated from a regular perturbation analysis of the equilibrium structure detailed in Appendix A, evaluated for $\phi = 0.27$. The polarization and hard-sphere viscosities are given by equations (A.11) and (A.12), respectively, while the hydrodynamic viscosity is the Einstein result $\eta_H = \frac{5}{2}\phi$. The exponential scaling of the low-shear viscosity for $\lambda < 4$ comes from the change in the equilibrium pair-distribution with the electric field.

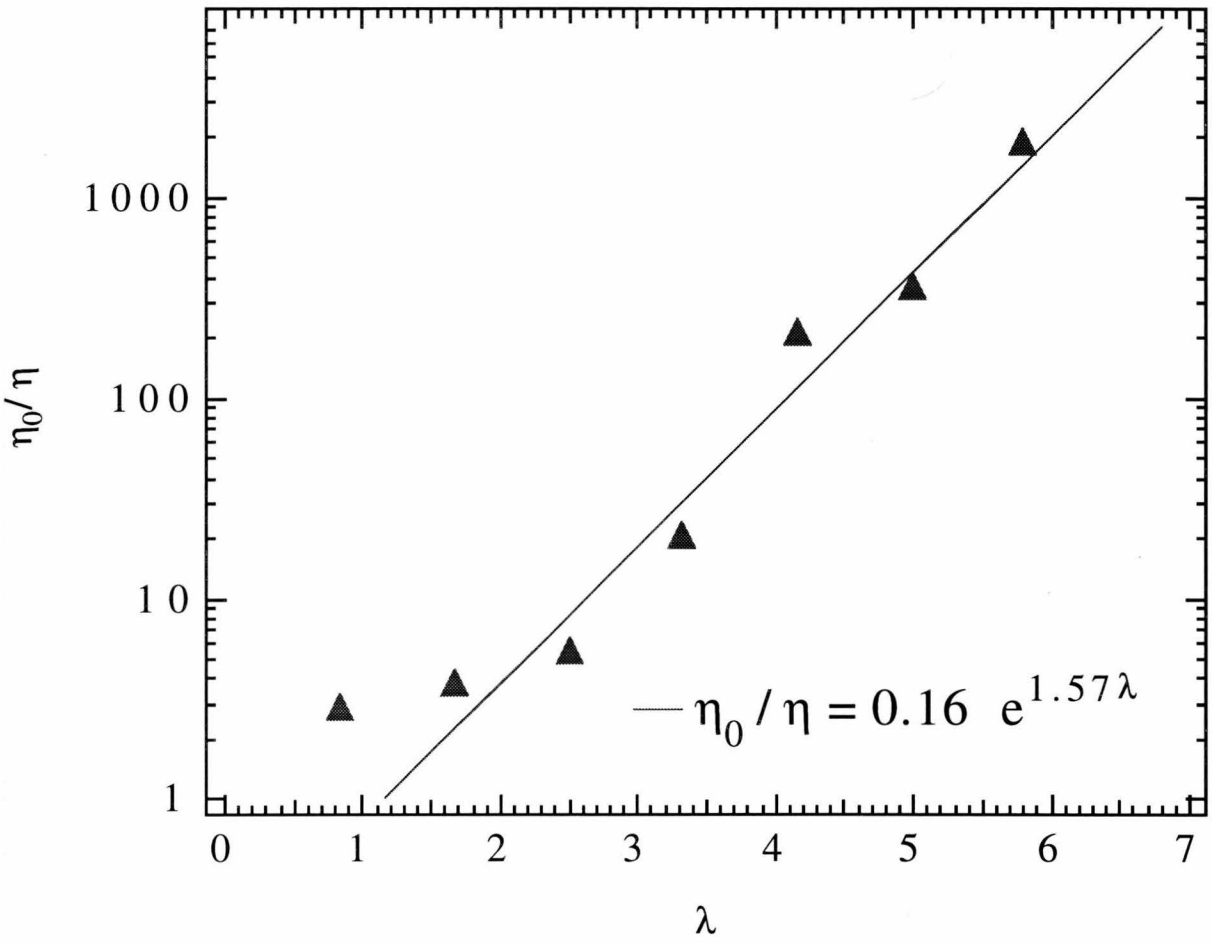

Figure 2.11: The low-shear viscosity ($Ma \to 0$) as a function of λ for $\lambda < 10$. The magnitude of the low-shear viscosity scales exponentially with λ. The line is the fit for $4 < \lambda < 6$ and also fits $\lambda = 2.5$ and 3.3.

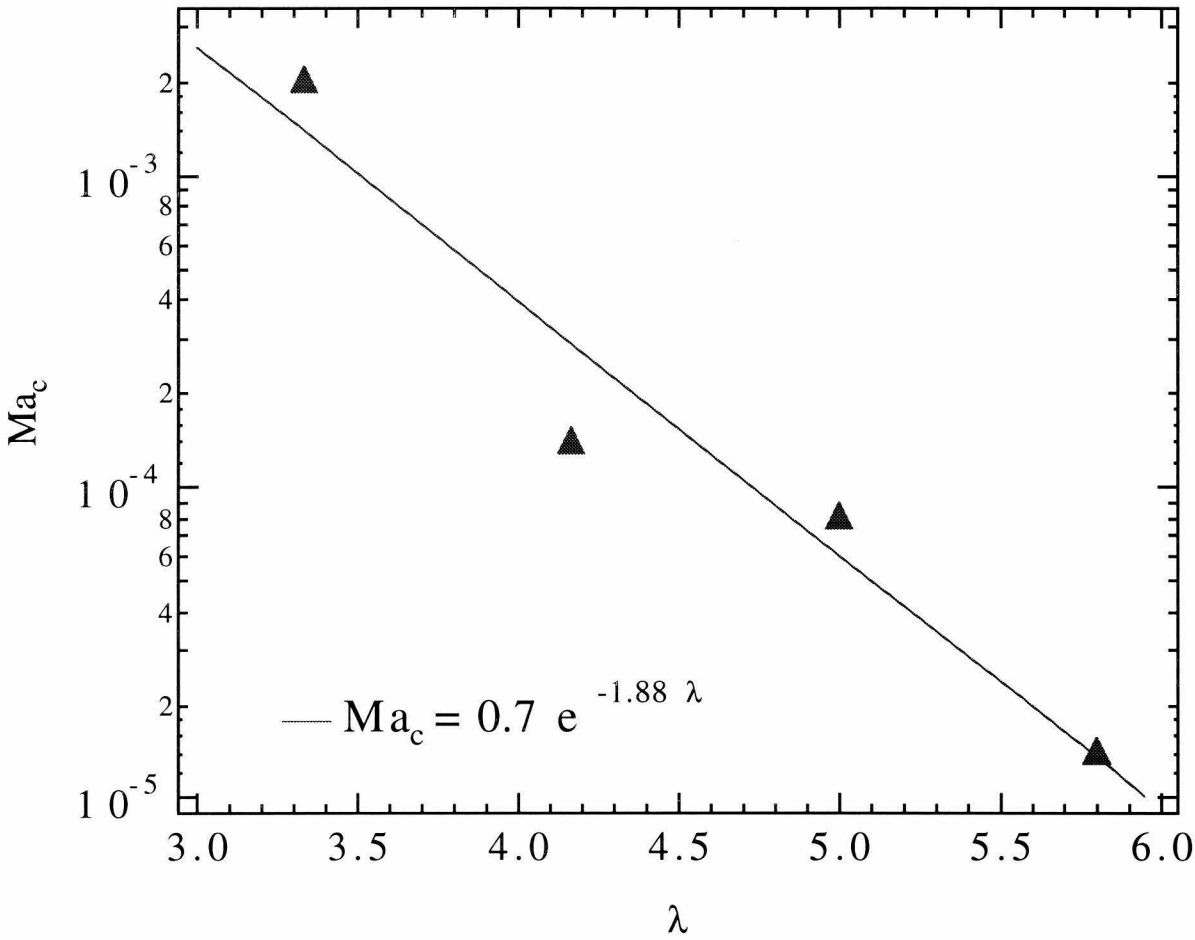

Figure 2.12: The critical Mason number, Ma_c, that marks the transition from shear thinning to the low-shear viscosity plateau for $3 < \lambda < 10$ as a function of λ. Ma_c was determined from the intercept of the lines $\eta_r = \eta_0$ and $\eta_r \sim Ma^{-1}$ in the shear thinning region. In reality, the transition occurs over a range of Mason numbers and the viscosity was not seen to shear thin as Ma^{-1} for $\lambda < 10$. Since we were unable to distinguish between the transition and the true shear thinning regions, we assumed a scaling similar to the scaling for very large to infinite λ.

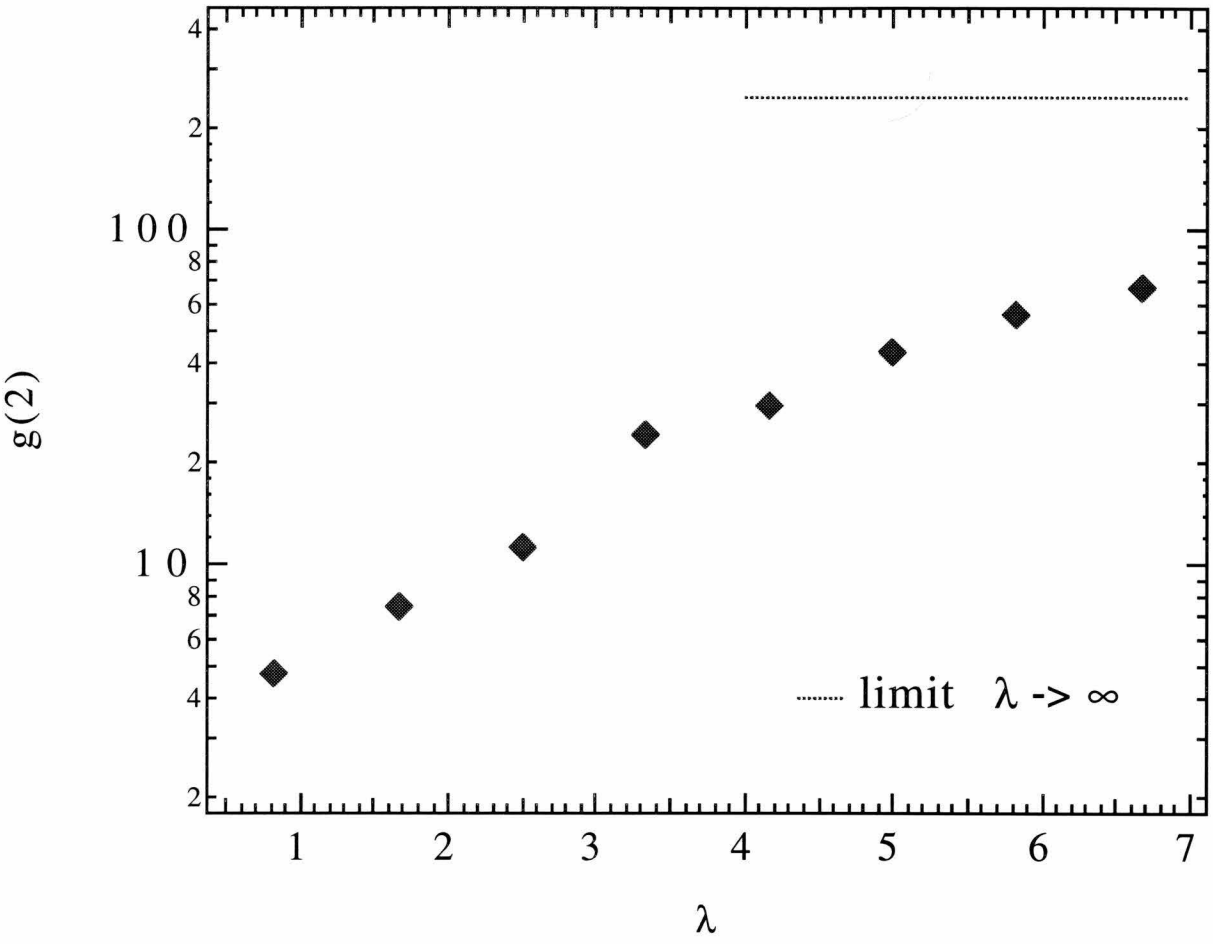

Figure 2.13: The pair-distribution function at contact versus the pair potential well depth. For $\lambda < 4$, $g(2)$ scales exponentially with λ indicating that the suspension has not flocculated. Above this λ, however, $g(2)$ saturates as the suspension becomes flocculated. The dashed line gives the $\lambda = \infty$ asymptote.

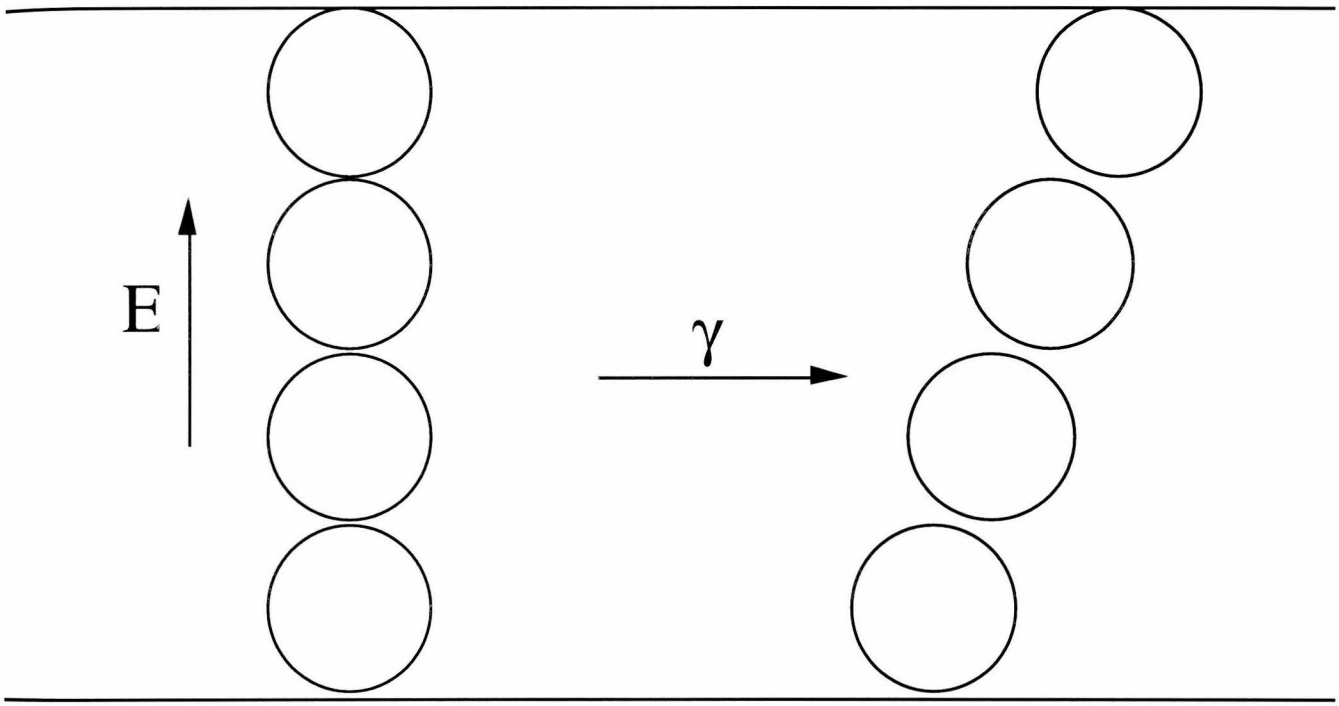

Figure 2.14: Illustration of a strained chain. The electrostatic forces attempt to realign the strained chain to its preferred orientation along the electric field direction.

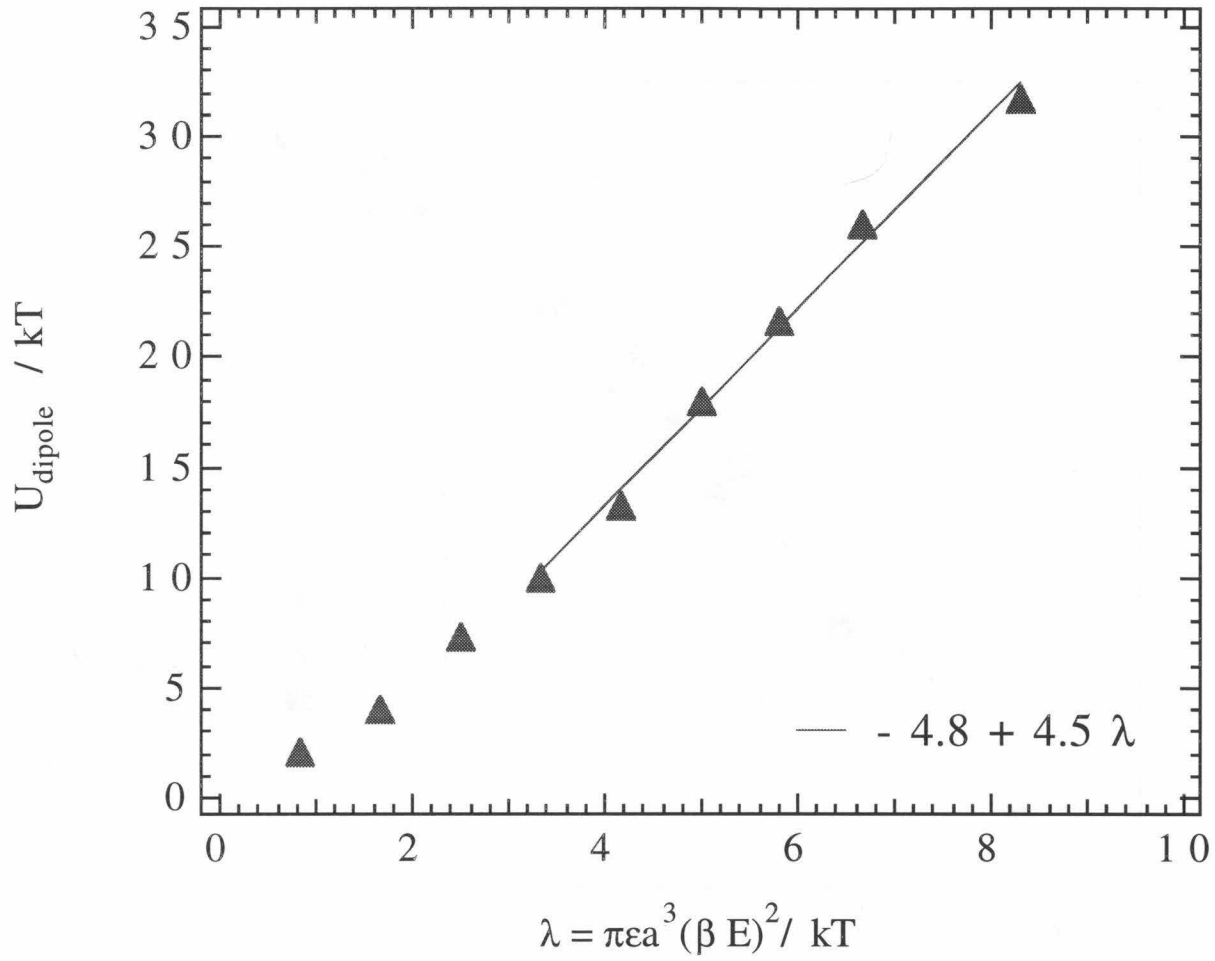

Figure 2.15: The pair potential well depth $\mathcal{U}_{dipole}/kT$ as a function of λ. For $\lambda < 4$ the point dipole approximation, λ, provides a good estimate of the potential well depth. Note the increase in the slope at $\lambda \sim 4$; here the aggregated structure provides enhancement beyond the point dipole limit. The point dipole approximation is one of two factors that causes the potential well depth U_{min}/kT that characterizes the escape time to differ from λ.

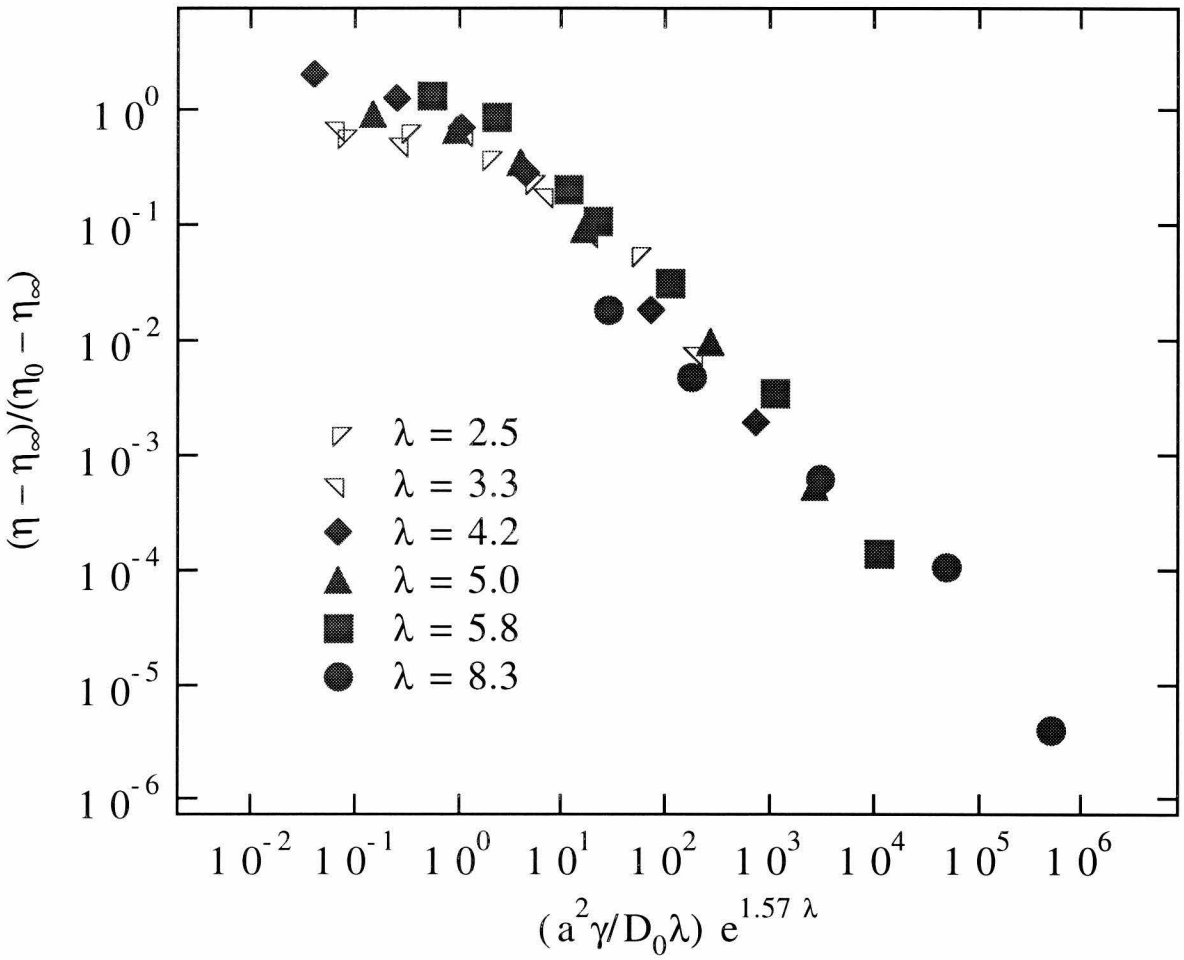

Figure 2.16: The reduced viscosity as a function of the dimensionless shear rate $(\dot{\gamma}a^2/D\lambda)\ e^{1.57\lambda}$. When the shear rate is rescaled with the escape time, τ, the data collapses onto a single curve.

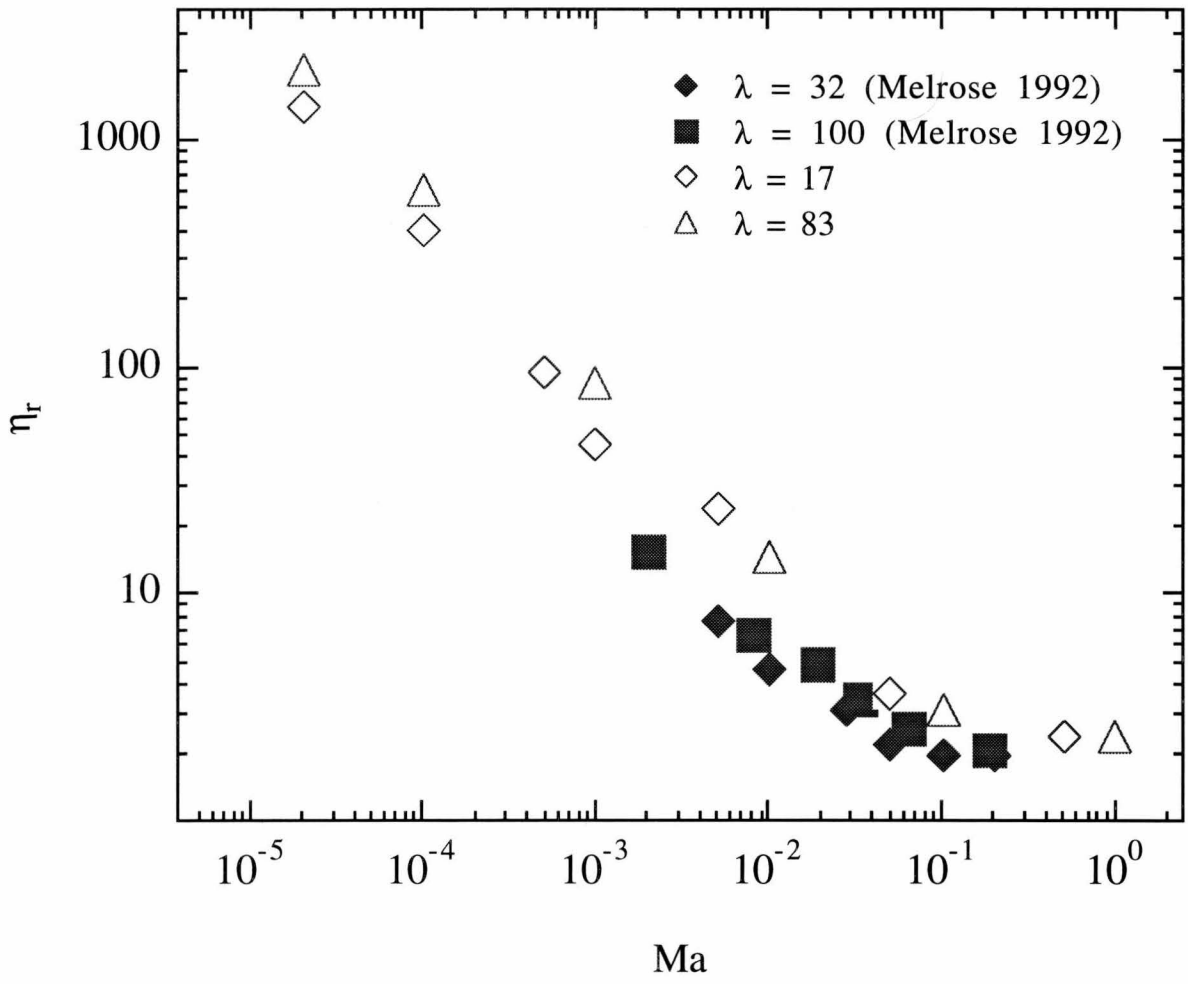

Figure 2.17: Comparison of the Stokesian Dynamics simulations at an area fraction of 0.4 with the Brownian Dynamics simulations of Melrose (1992) at volume fraction 0.31.

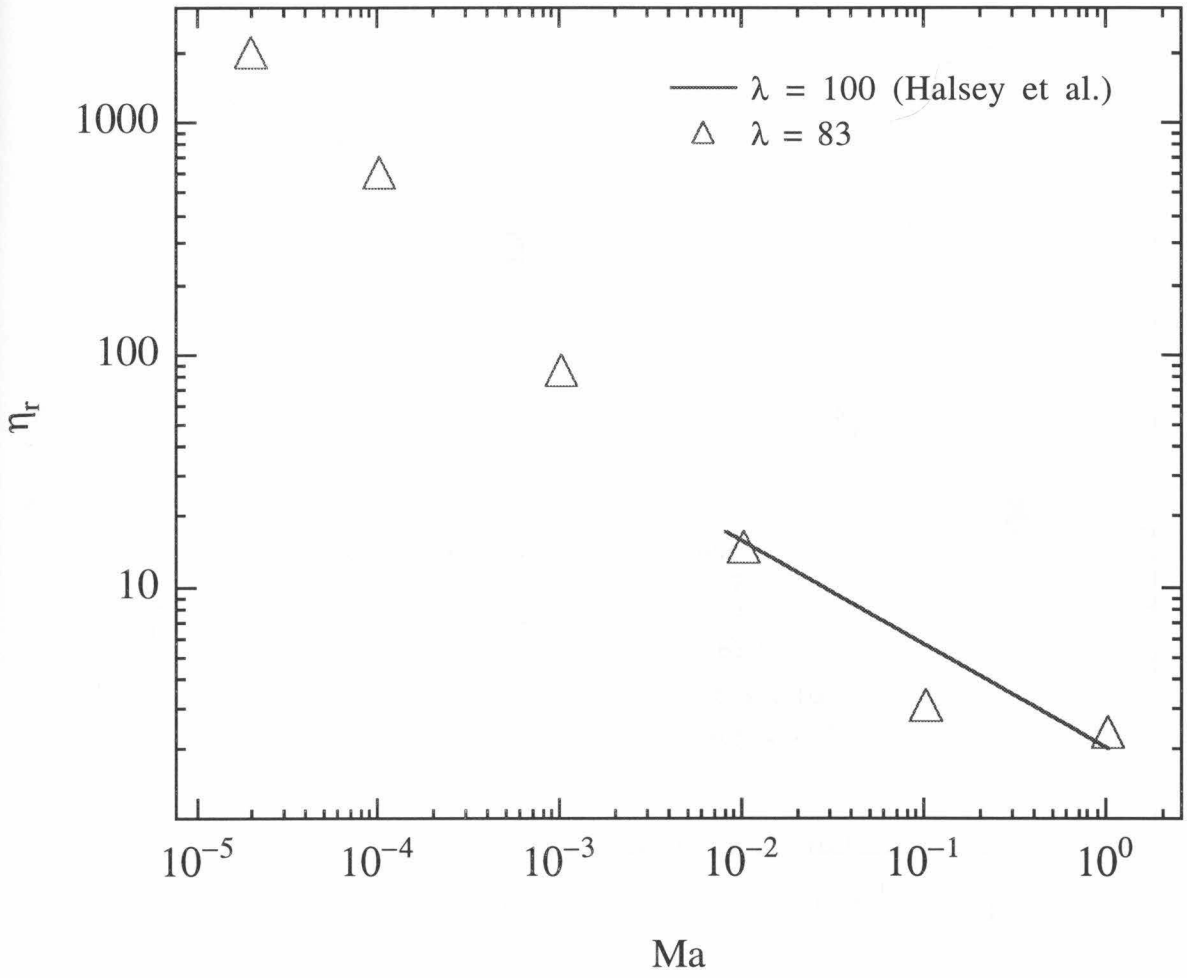

Figure 2.18: Comparison of simulation viscosities with the experiments of Halsey, Martin & Adolf (1992). The straight line is from figure (2) of their paper and gives their linear fit to the experimental data for an applied field of $400V/cm$.

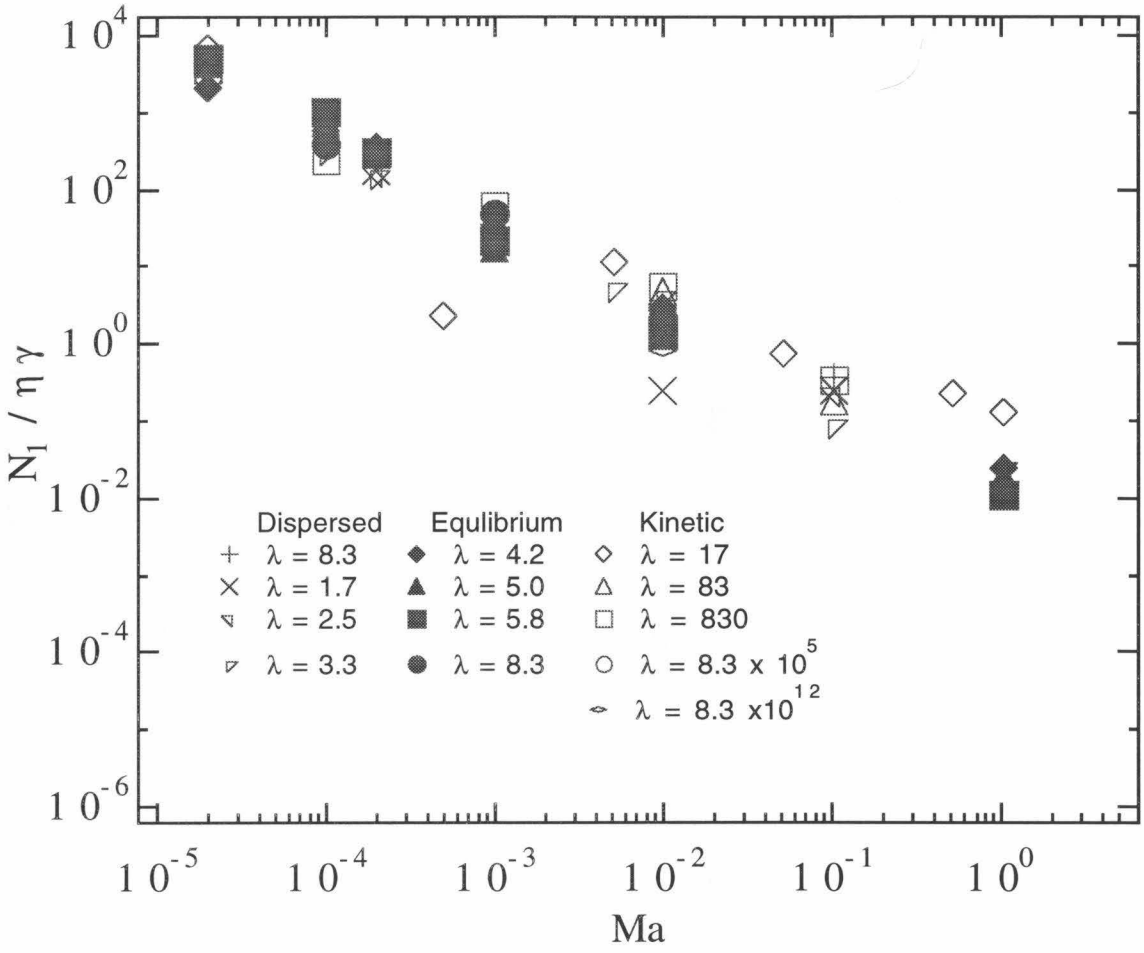

Figure 2.19: The first normal stress difference non-dimensionalized by $\eta\dot{\gamma}$ as a function of Ma. Note that for $\lambda = 8.3 \cdot 10^{12}$, $-N_1$ is plotted.

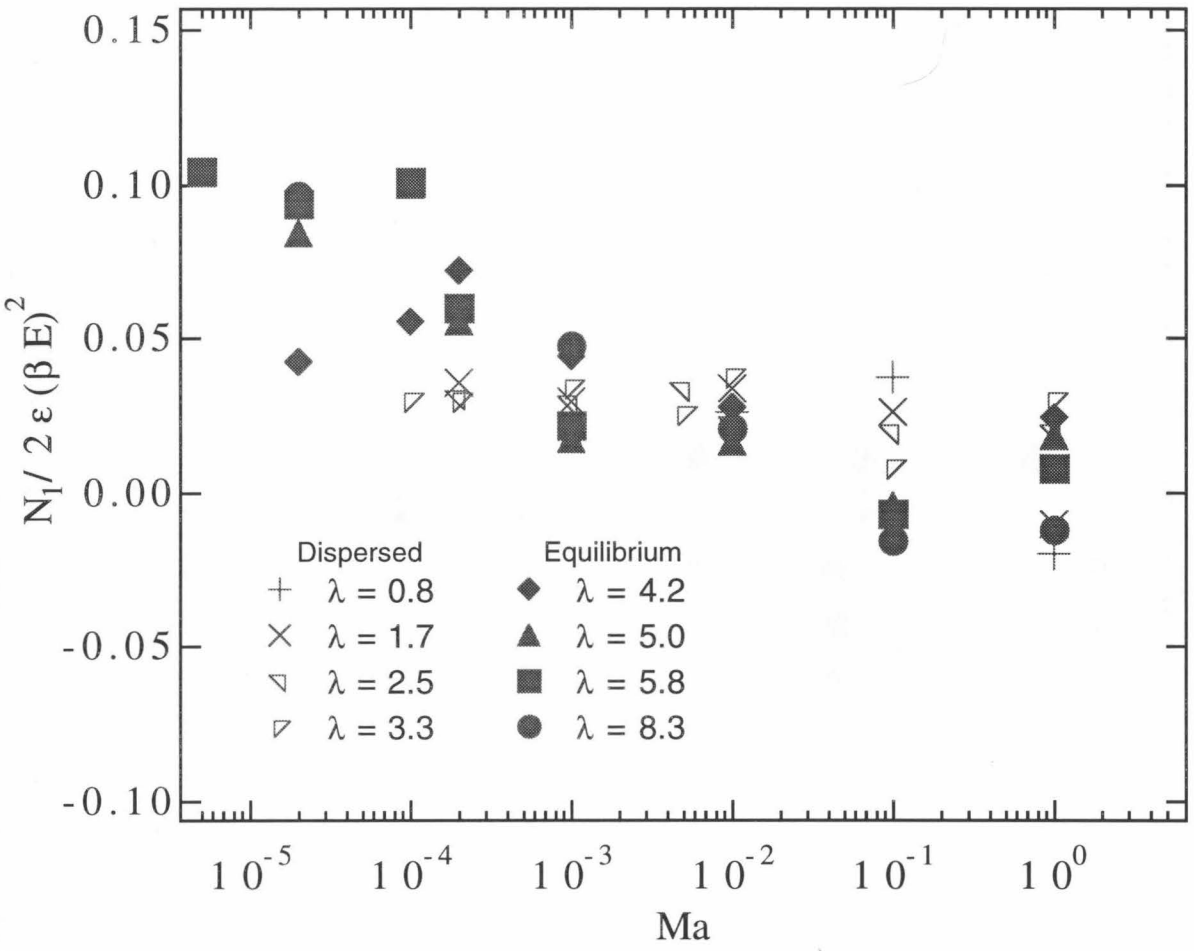

Figure 2.20: The first normal stress difference non-dimensionalized electrostatically vs. Ma for $\lambda < 10$. At low shear rates $N_1/(2\epsilon(\beta E)^2)$ is independent of Ma.

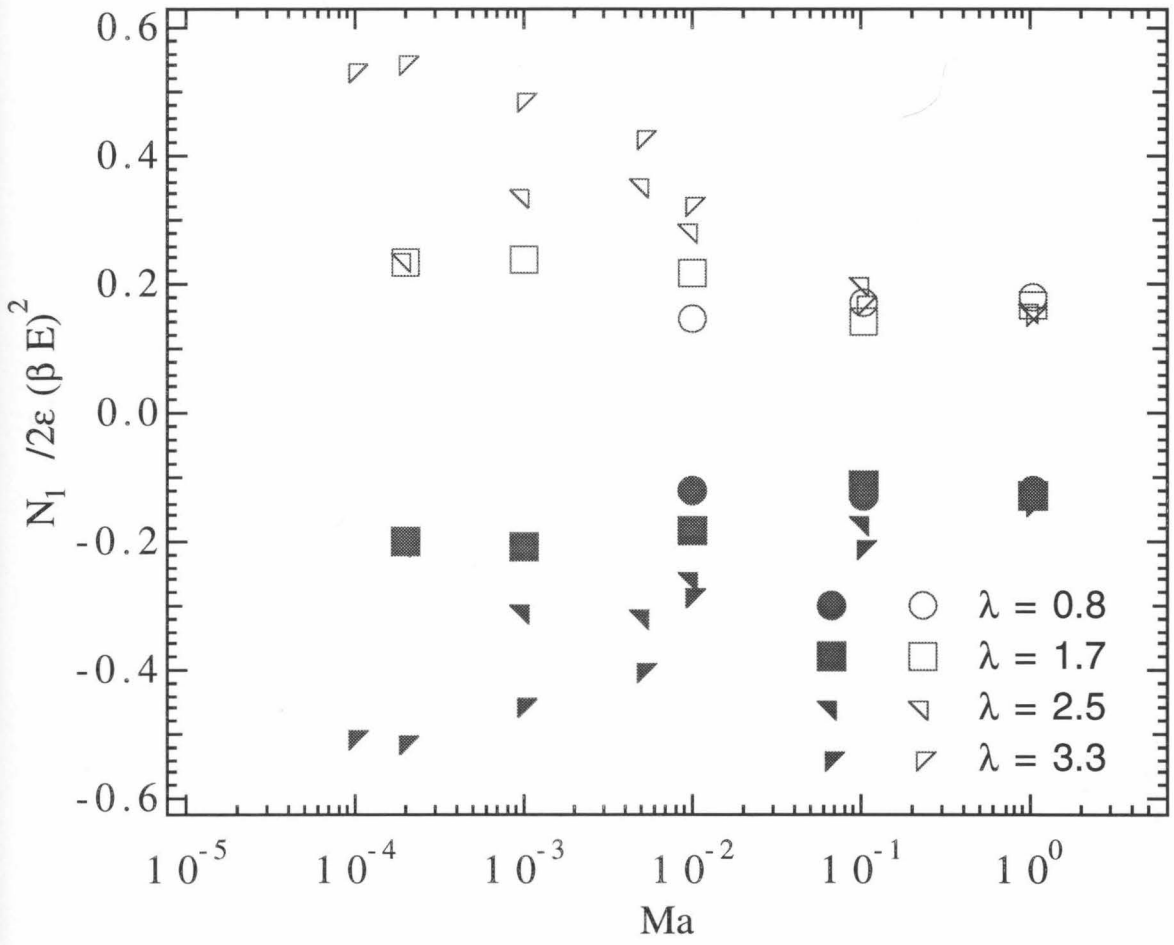

Figure 2.21: The interparticle and Brownian contributions to the first normal stress difference non-dimensionalized electrostatically vs. Ma for $\lambda < 4$. The shaded symbols are the xF contributions. The magnitude of the low-shear values of N_1^{xF} and N_1^{SP+B} scale exponentially with λ.

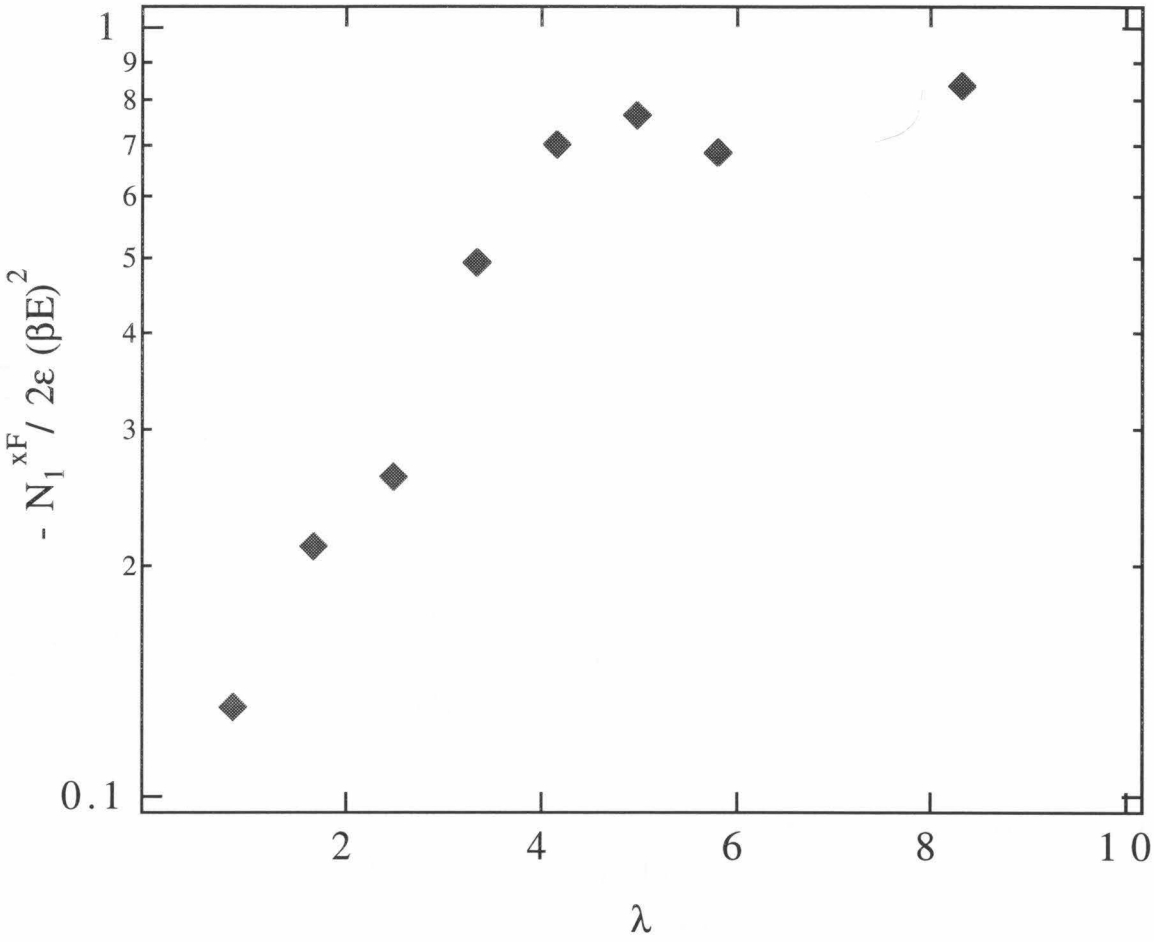

Figure 2.22: The low-shear first normal stress difference vs. λ. For $\lambda < 4$, the low-shear normal stress difference scales exponentially with λ since the stress is proportional to $g(2)$ which in turn scales as e^{λ}. Note that this gives the correct scaling as $\lambda \to 0$; $N_1(a^3/kT) \sim \lambda \exp(\lambda)$, which vanishes as $\lambda \to 0$. For $\lambda > 4$ the low-shear first normal stress difference is independent of λ.

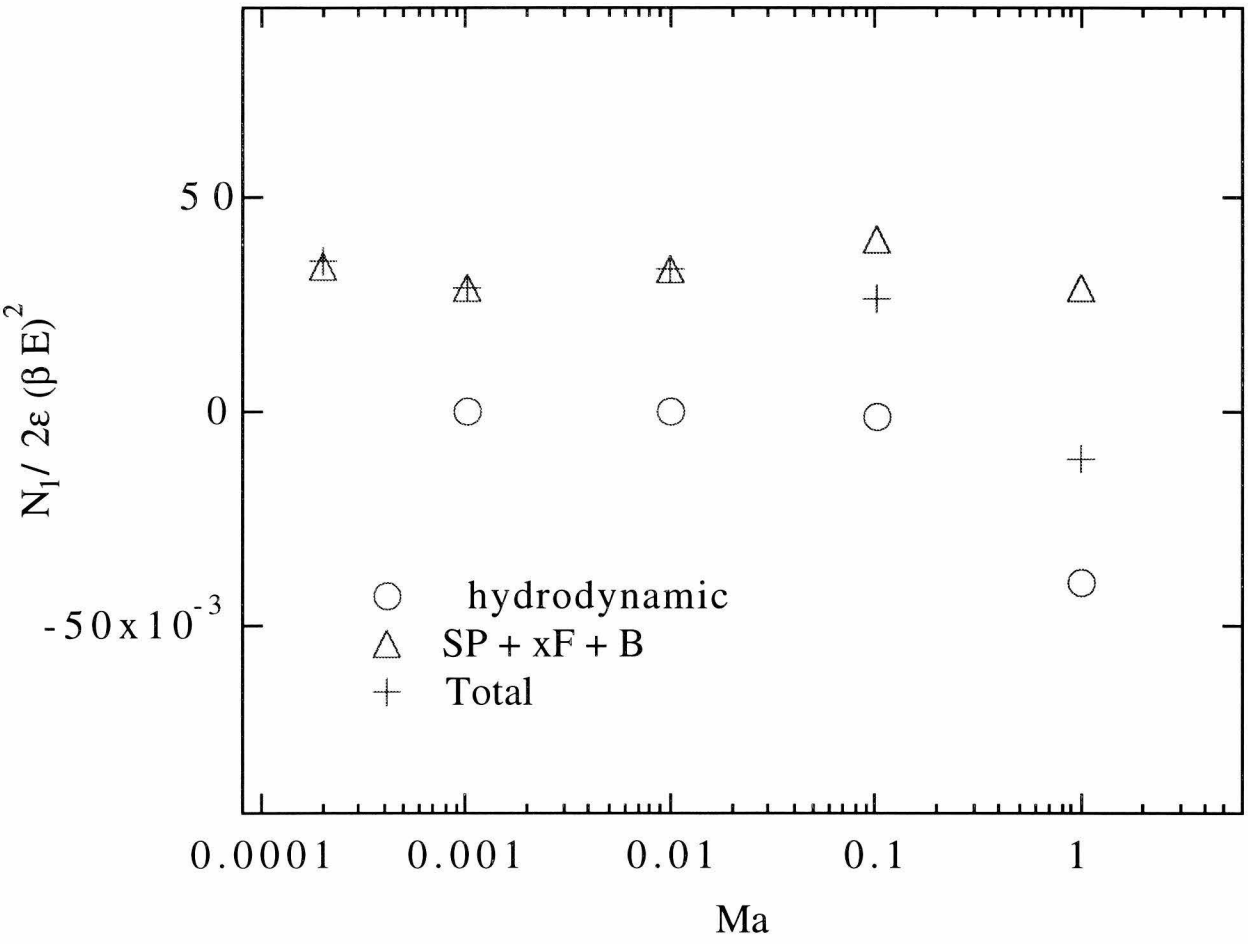

Figure 2.23: $N_1^{xF+SP+B}/2\epsilon(\beta E)^2$ and $N_1^H/2\epsilon(\beta E)^2$ vs. Ma for $\lambda = 1.7$. At low shear rates the sum of **xF, SP** and **B** dominates and the first normal stress difference is positive. At high shear rates when viscous forces dominate, the hydrodynamic stress is the major contributor to the stress.

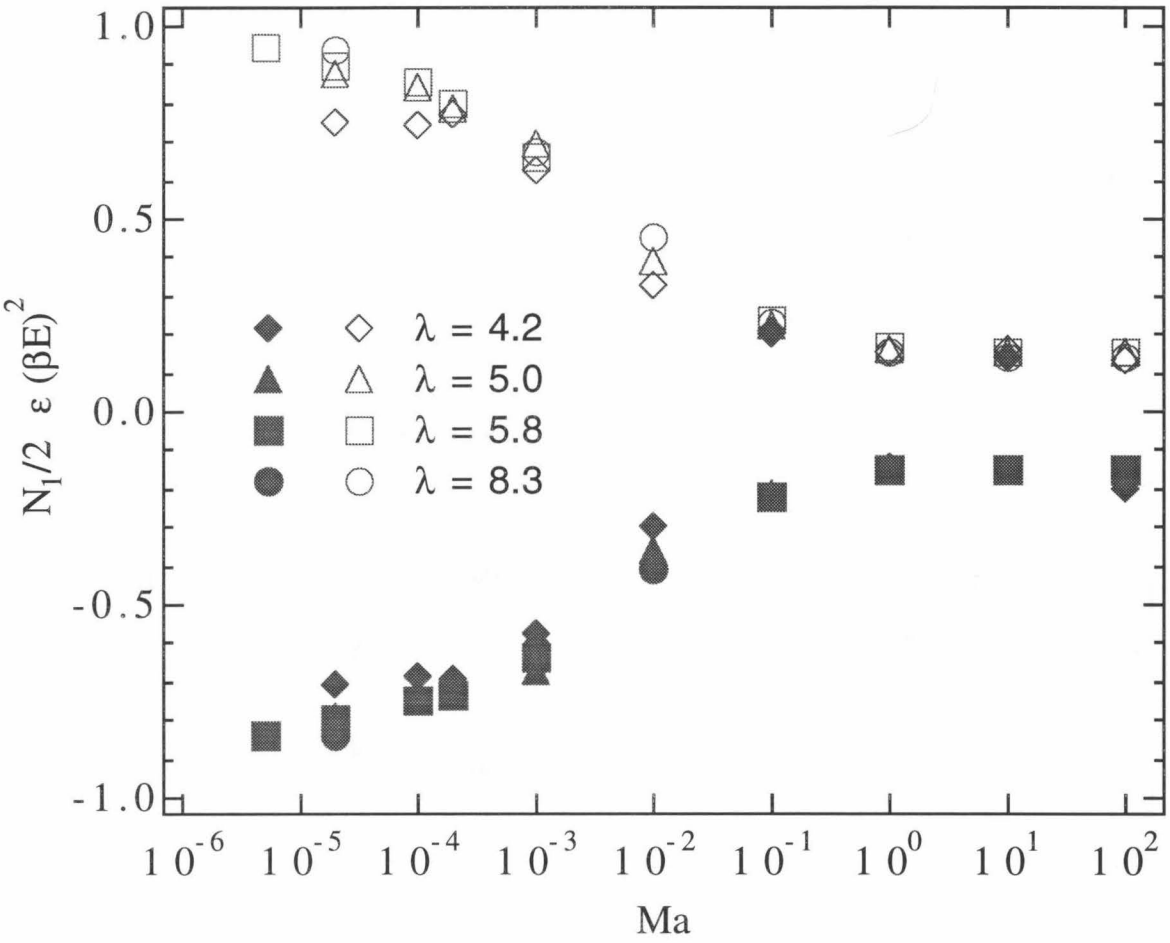

Figure 2.24: The interparticle and Brownian contributions to the first normal stress difference non-dimensionalized electrostatically vs. Ma for $4 < \lambda < 10$. The shaded symbols are the xF contributions. Similar to the dispersed regime, N_1^{xF} is negative for all Ma and approaches a low-shear-limiting value as $Ma \to 0$. Unlike the dispersed regime, however, the low-shear limiting value is independent of λ.

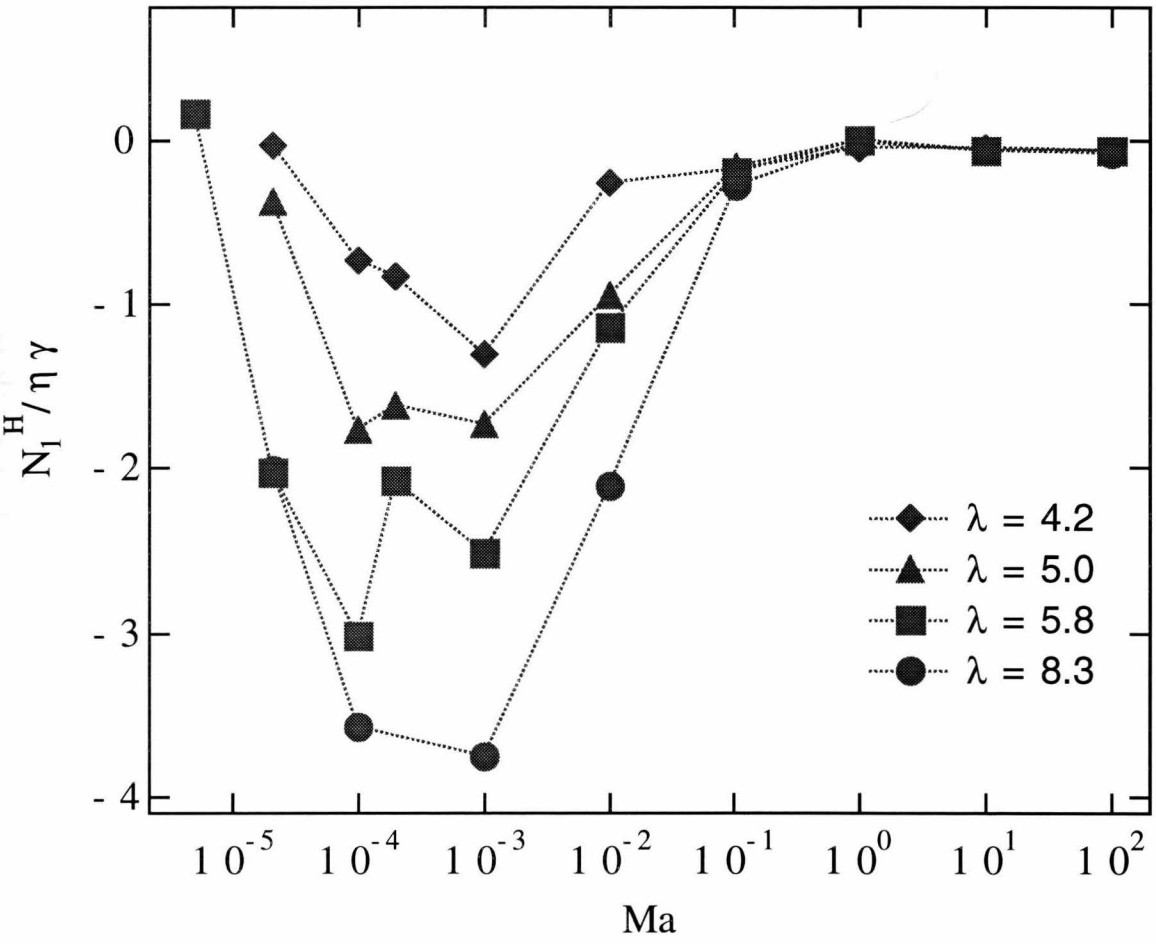

Figure 2.25: The hydrodynamic contribution to the first normal stress difference non-dimensionalized by $\eta\dot{\gamma}$ vs. Ma for $4 < \lambda < 10$. The lines are drawn to guide the eye. The hydrodynamic contribution is negative for all Ma, decreases as Ma decreases and has a minimum at intermediate shear rates. It finally increases for $Ma < 10^{-4}$.

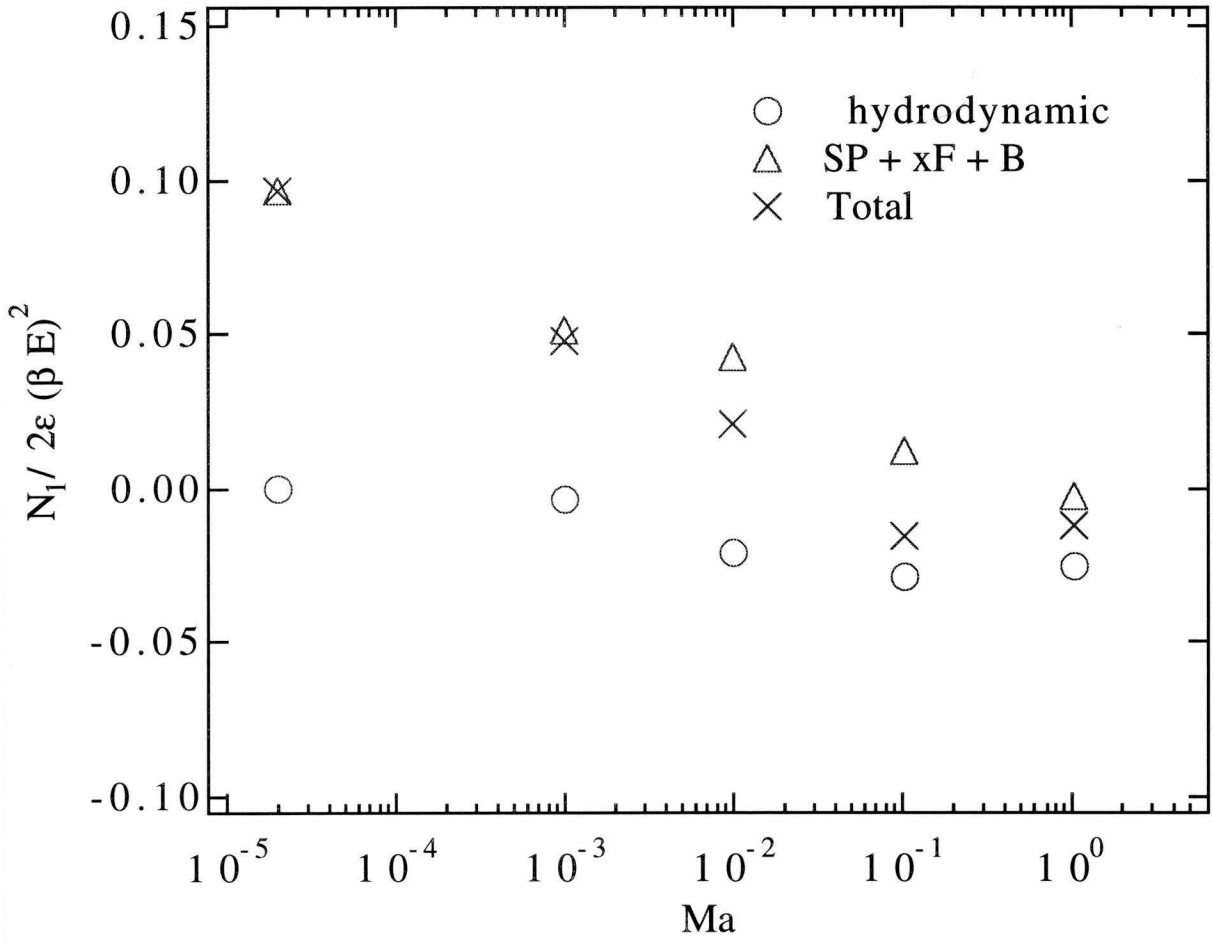

Figure 2.26: $N_1^{xF+SP+B}/2\epsilon(\beta E)^2$ and $N_1^H/2\epsilon(\beta E)^2$ vs. Ma for $\lambda = 8.3$. At low shear rates the sum of **xF, SP** and **B** dominates and the first normal stress difference is positive. At high shear rates when viscous forces dominate, the hydrodynamic stress is the major contributor to the stress.

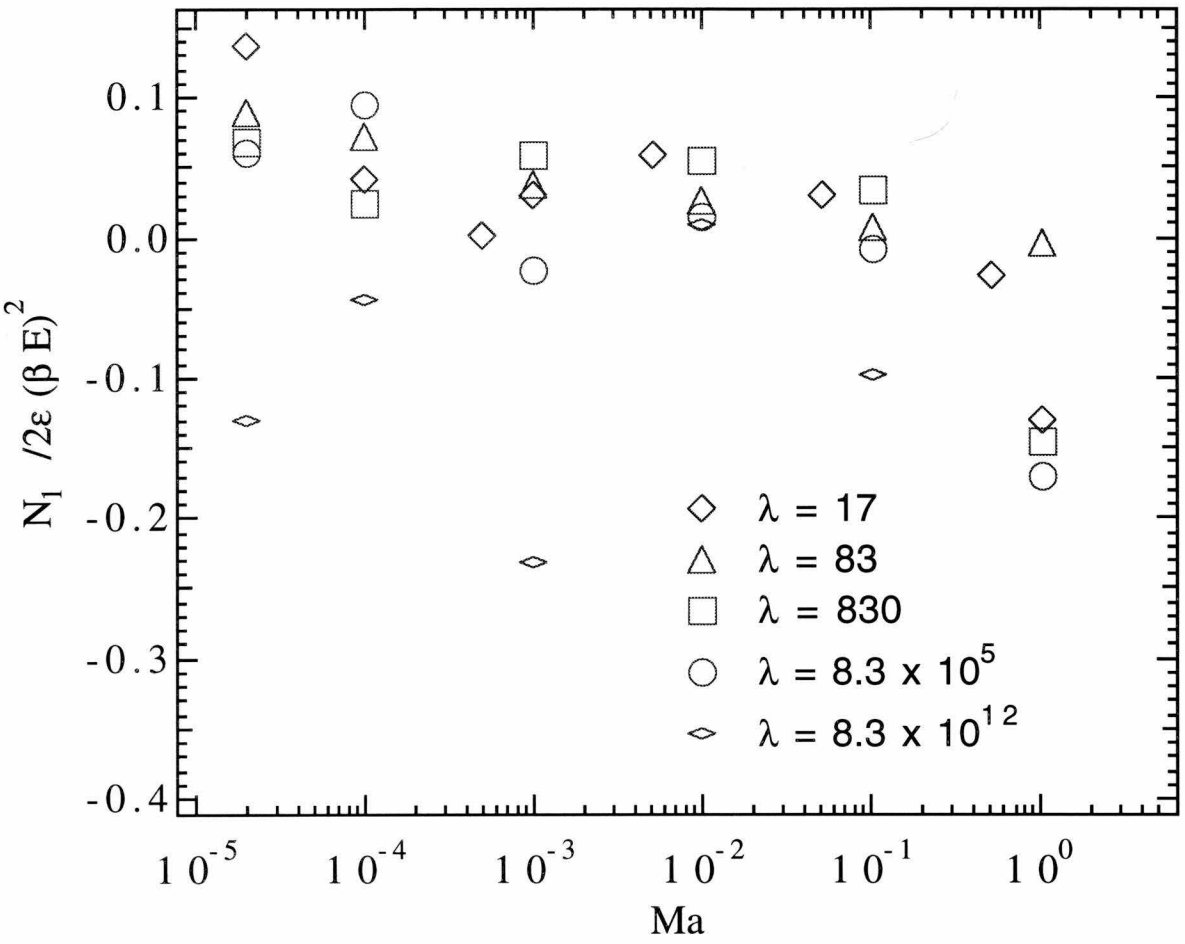

Figure 2.27: The first normal stress difference non-dimensionalized electrostatically vs. Ma in the kinetically flocculated regime. Statistical uncertainties make it difficult to determine a low- or high-shear plateau. For $\lambda = 8.3 \cdot 10^{12}$, N_1 is negative for all Ma studied, and for $\lambda = 8.3 \cdot 10^5$, N_1 appears to oscillate from positive to negative over the entire range of Ma.

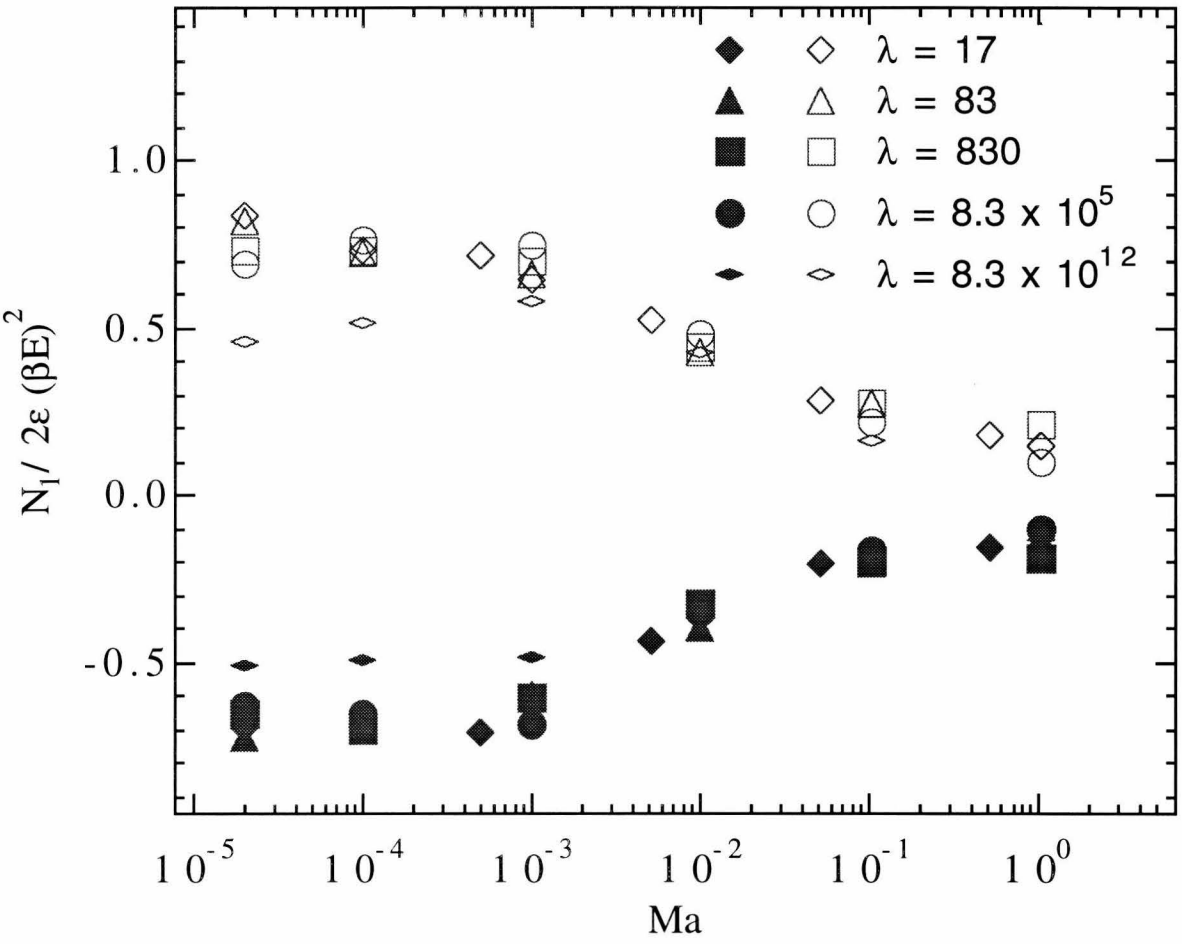

Figure 2.28: The interparticle and Brownian contributions to the first normal stress difference non-dimensionalized electrostatically vs. Ma in the kinetically flocculated regime. The shaded symbols are the xF contributions. There is a low-shear plateau that is independent of λ for $10 < \lambda < 8.3 \cdot 10^{12}$.

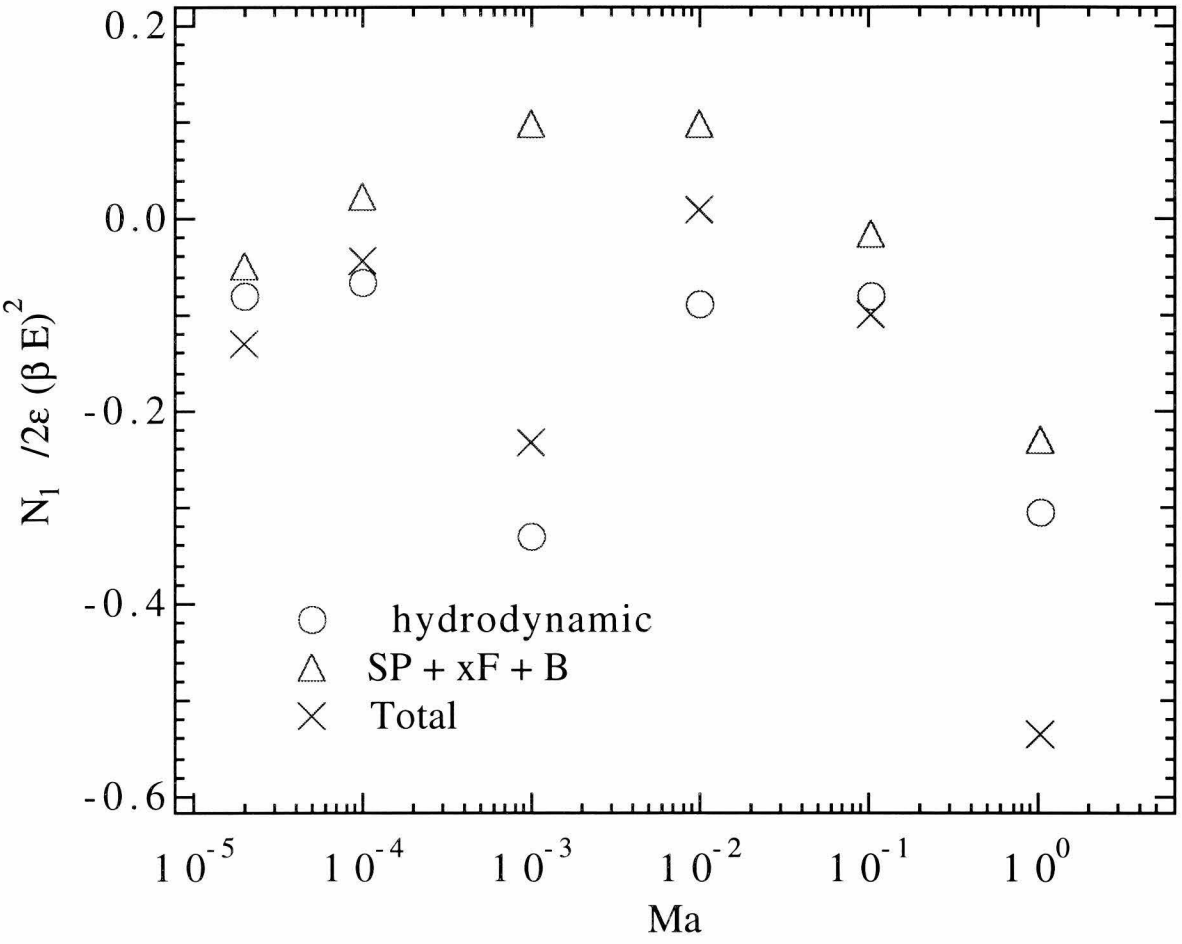

Figure 2.29: $N_1^{xF+SP+B}/2\epsilon(\beta E)^2$ and $N_1^H/2\epsilon(\beta E)^2$ vs. Ma for $\lambda = 8.3 \cdot 10^{12}$. At all shear rates the hydrodynamic stress is the major contributor to N_1 and the first normal stress difference is negative.

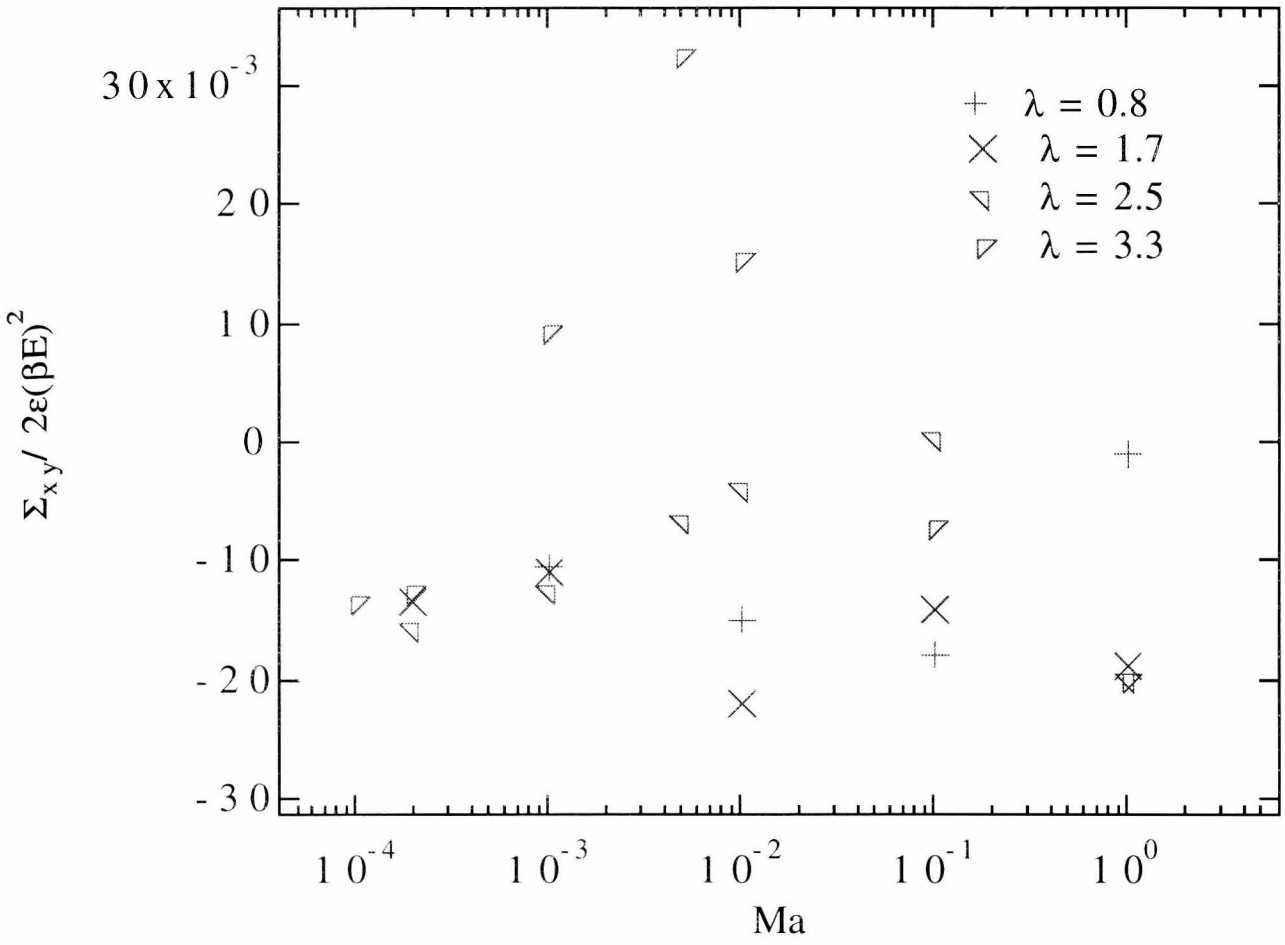

Figure 2.30: $\Sigma_{xy}^{xF}/2\epsilon(\beta E)^2$ vs. Ma for the dispersed regime, $\lambda < 4$.

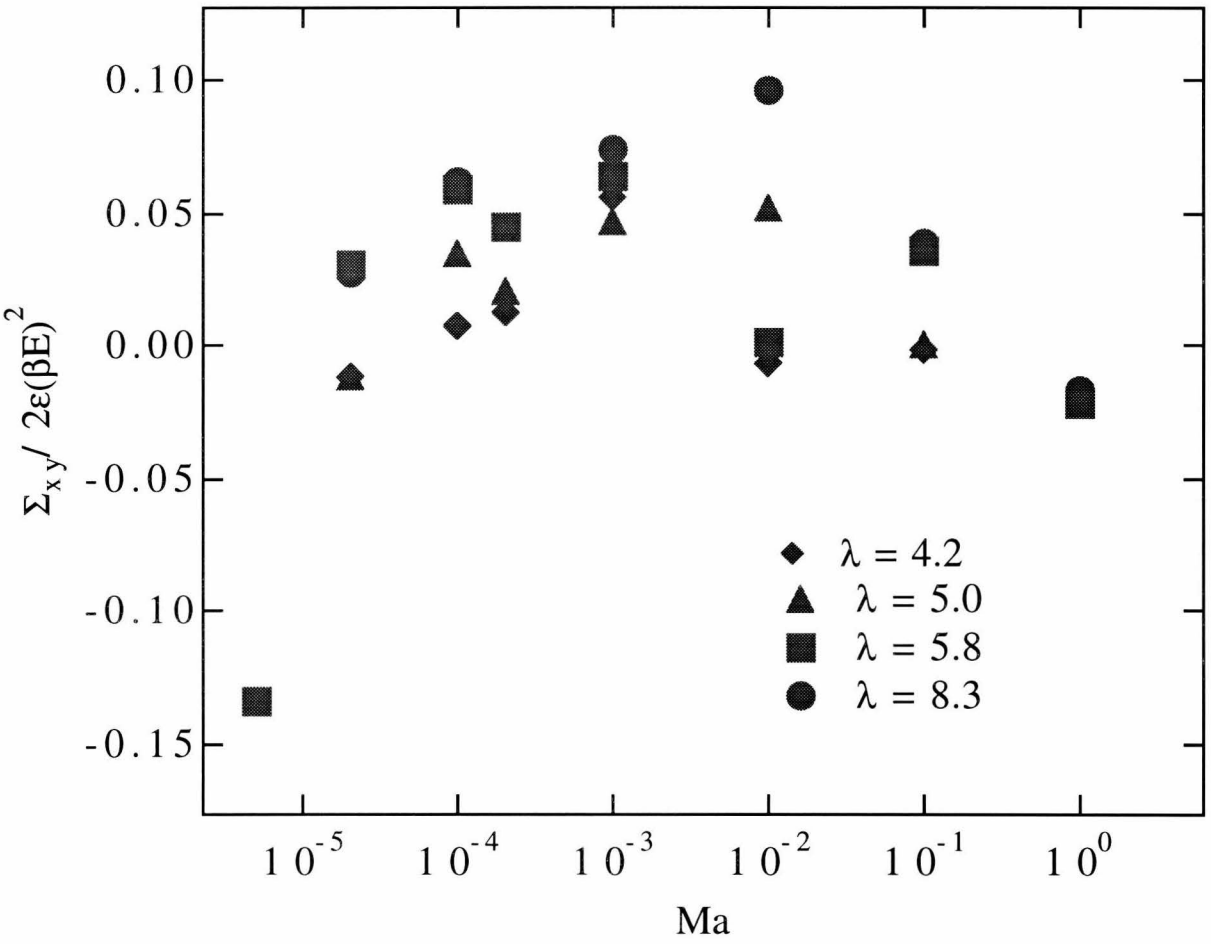

Figure 2.31: $\Sigma_{xy}^{xF}/2\epsilon(\beta E)^2$ vs. Ma for the equilibrium flocculated regime, $4 < \lambda < 10$.

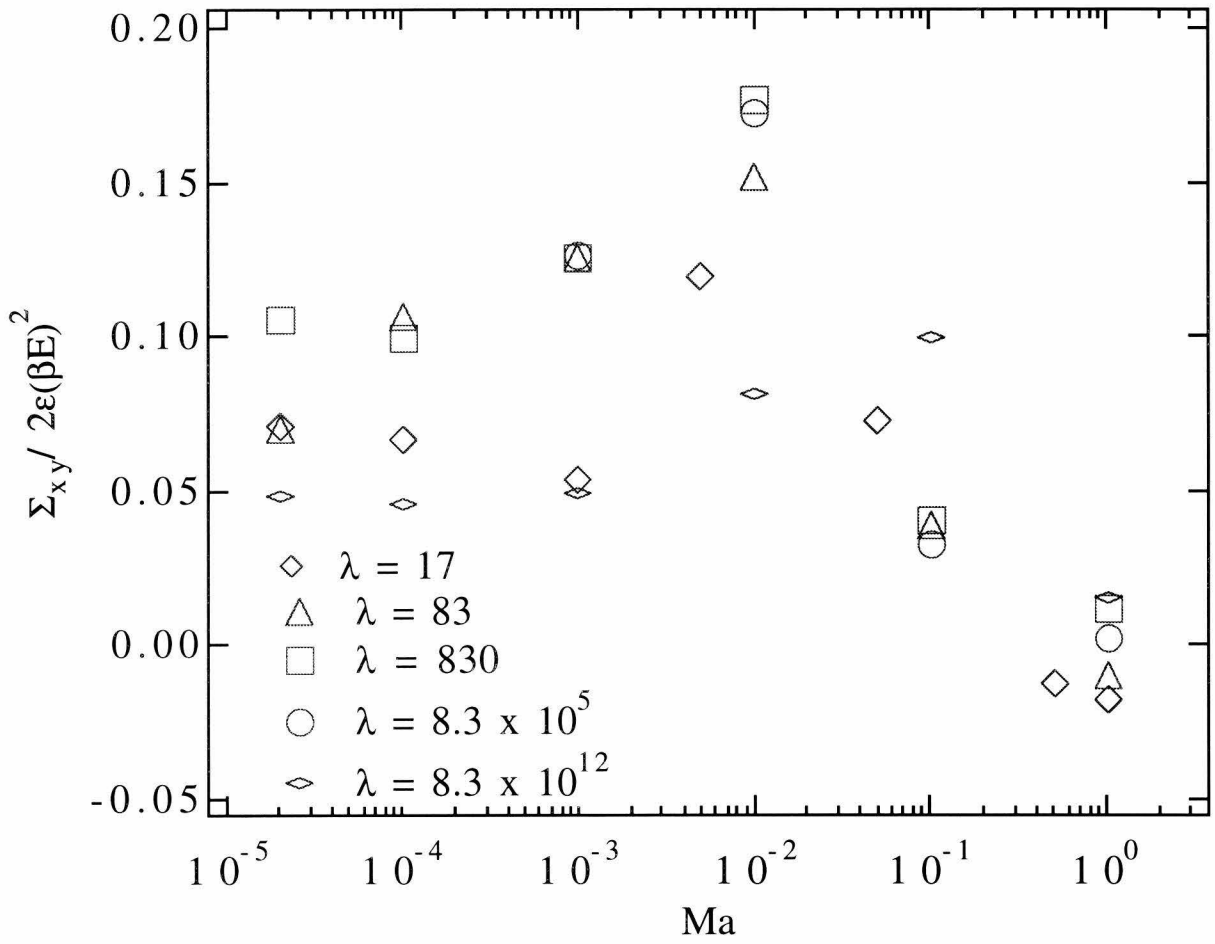

Figure 2.32: $\Sigma_{xy}^{xF}/2\epsilon(\beta E)^2$ vs. Ma for the kinetically flocculated regime, $\lambda > 10$.

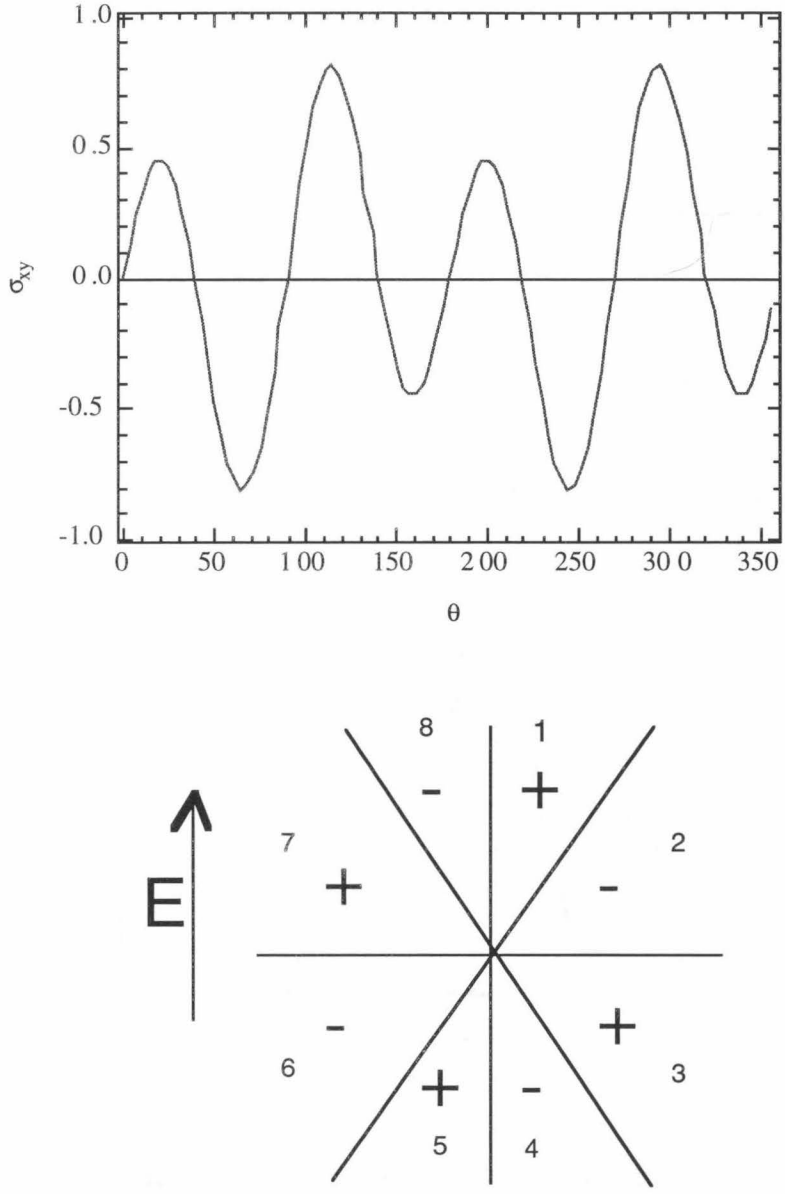

Figure 2.33: A schematic of the regions of orientation where Σ_{xy}^{xF} changes sign from positive to negative. The top graph is Σ_{xy}^{xF} for touching pairs as given in Eq. 2.33. The contribution from pairs in sections $2, 3, 6$, and 7 (lower graph) are larger than pairs in sections $1, 4, 5$, and 8. The bottom graph shows a schematic of the sections where Σ_{xy}^{xF} changes sign from positive to negative.

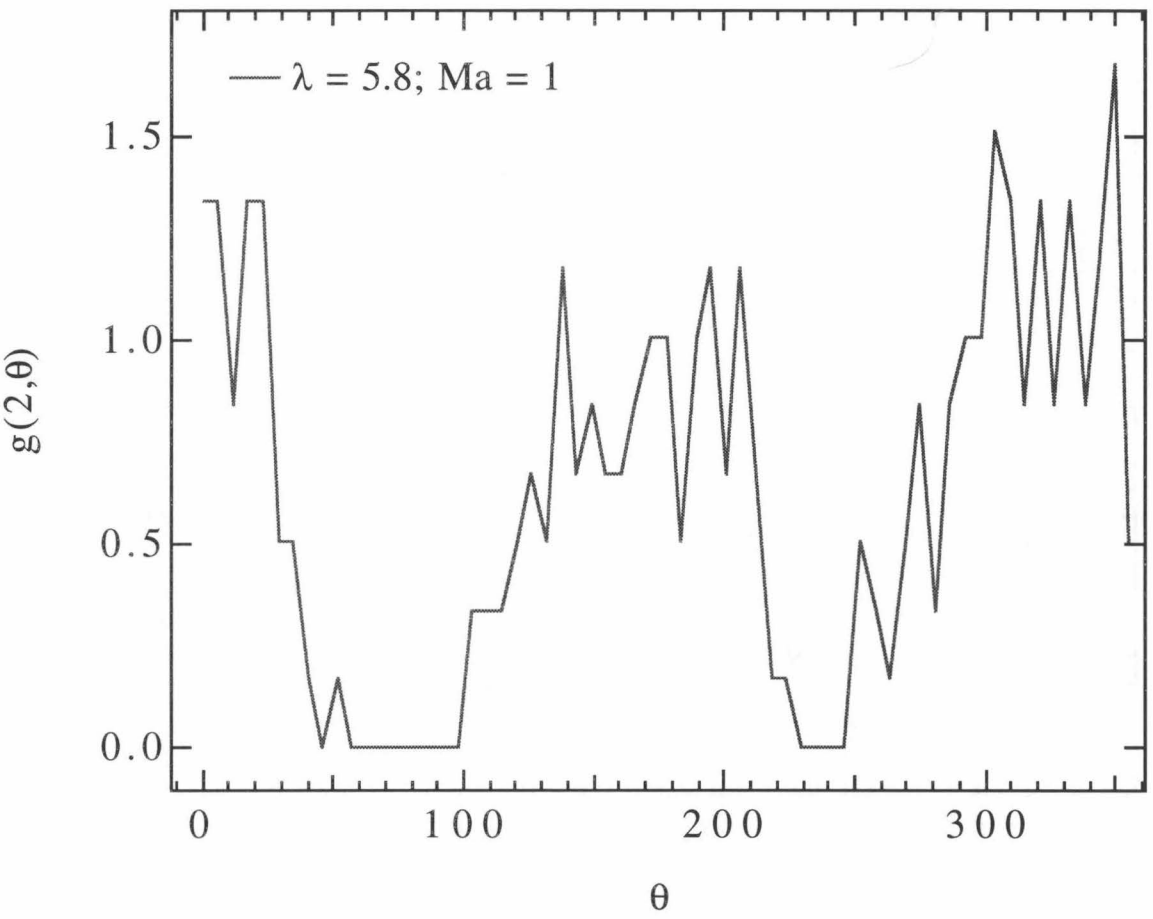

Figure 2.34: $g(2,\theta)$ averaged over the entire simulation as a function of θ for $\lambda = 5.8$ and $Ma = 1$. There is a preference for pairs aligned in section 8 where Σ_{xy}^{xF} is negative.

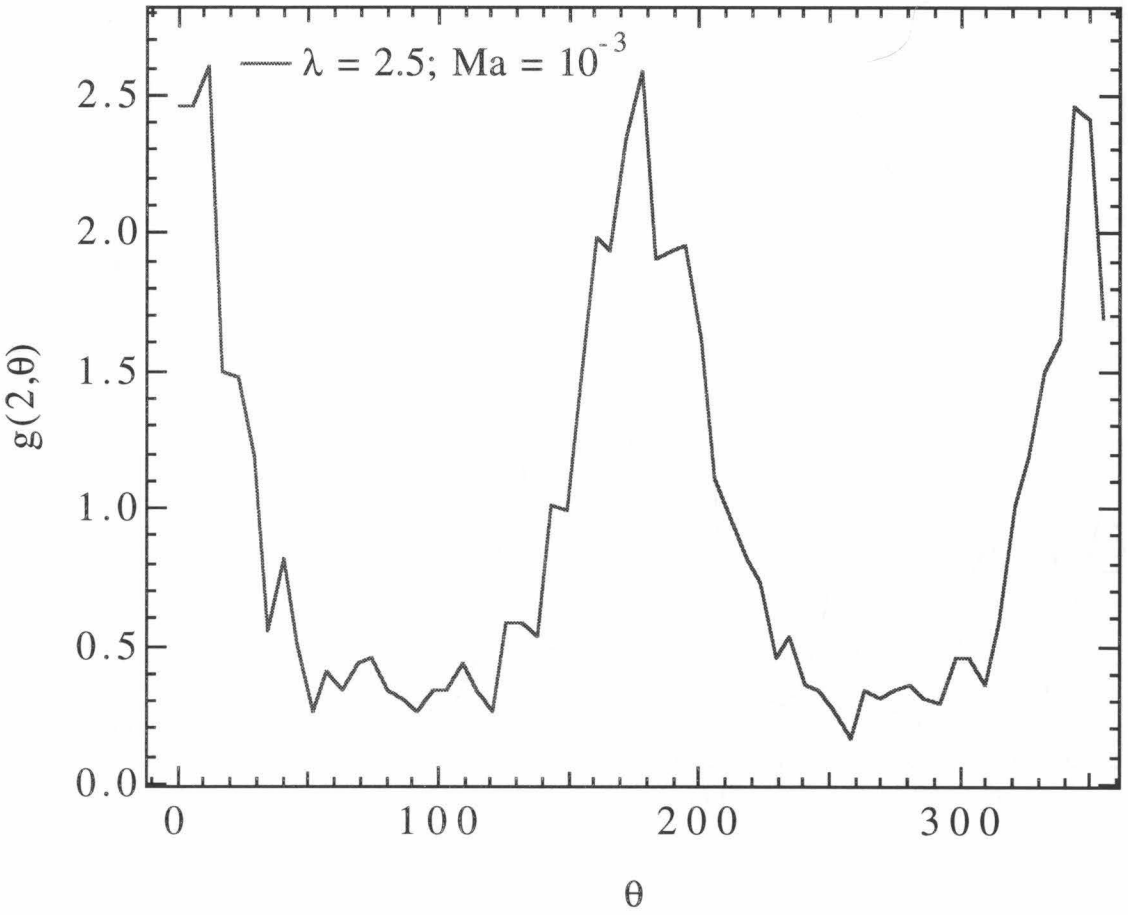

Figure 2.35: $g(2, \theta)$ averaged over the entire simulation as a function of θ for $\lambda = 2.5$ and $Ma = 10^{-3}$.

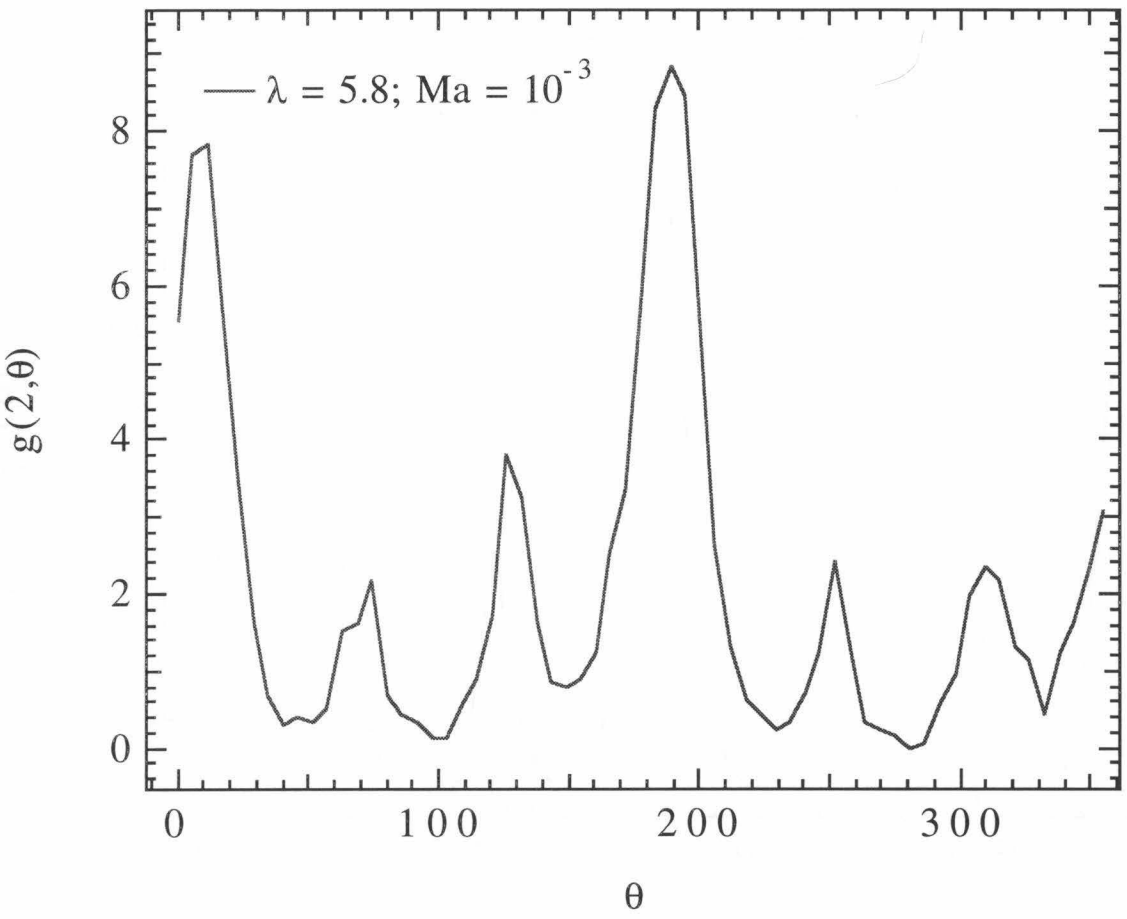

Figure 2.36: $g(2,\theta)$ averaged over the entire simulation as a function of θ for $\lambda = 5.8$ and $Ma = 10^{-3}$. There is a preference for pairs aligned in section 1 where Σ_{xy}^{xF} is positive.

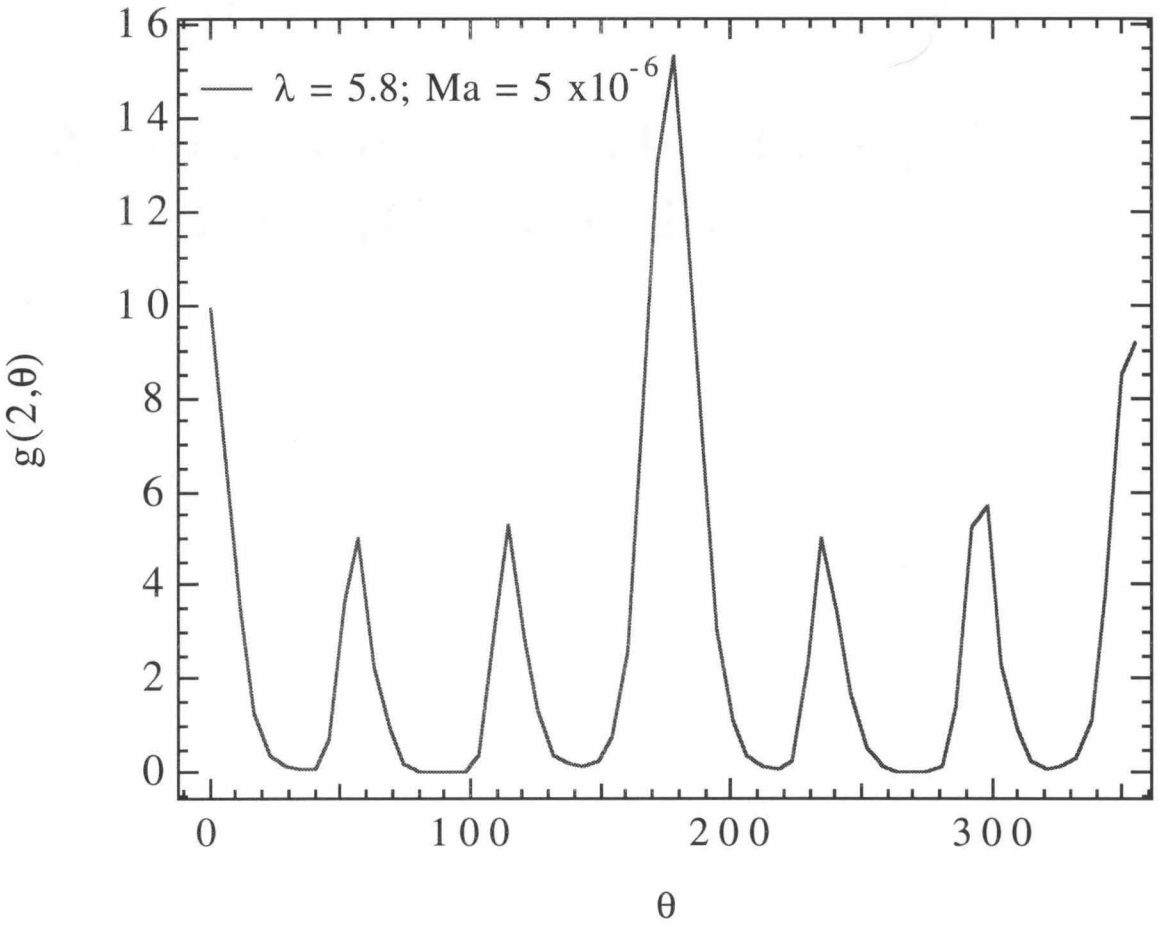

Figure 2.37: $g(2,\theta)$ averaged over the entire simulation as a function of θ for $\lambda = 5.8$ and $Ma = 5 \cdot 10^{-6}$

Chapter 3

A model for the rheology of flocculated dispersions

3.1 The Model

The concept of the escape time – the time to diffuse out of the potential minimum – can be used to formulate a model for the viscosity of aggregating suspensions. The model closely follows Glasstone et al.'s (1941) viscosity model for molecular liquids and describes the suspension rheology in terms of the microscopic rearrangements in the network structure. Similar ideas have been used by Potanin et al. (1995) to model fractal flocs. At rest, a flocculated suspension consists of a network of particles, each within a potential cage formed by its nearest neighbors as depicted in figure 3.1. Rearrangement requires breaking a contact pair and forming a new contact, i.e., hopping over a dimensionless distance Γ relative to the particle size. The activation energy barrier is on the order of the minimum in the pair potential. For simplicity, the particle potential is represented as being symmetrical about the hopping distance, i.e., the particle's activated state is halfway between its initial and final positions. Network rearrangement occurs as particles hop out of their potential well on the time scale τ. Under static, non-stressed conditions, the initial and final states are equally favorable so there is no net motion of the network; particles hop back and forth with equal probability, and the suspension does not flow or shear.

Under an external stress, σ, the suspension acquires an elastic energy density $\sigma\gamma/2\epsilon(\beta\mathcal{E})^2$, where γ is the macroscopic strain. (The stress is appropriately non-dimensionalized by $2\epsilon(\beta\mathcal{E})^2$ since the induced internal stress will be predominantly electrostatic in origin and at equilibrium the induced internal stress is equal to the applied stress.) On the microscopic scale the acquired energy resides in the pair-

interaction potential such that the new energy barrier is given by

$$\frac{-U_{min}}{kT} \pm \frac{\sigma a^3 \Gamma V_0}{\lambda kT}, \tag{3.1}$$

where V_0 is the dimensionless volume of the particle pair and depends, as does Γ, on the details of the network structure and how the macroscopic stress is distributed locally on the microscale. For example, an affine deformation would have the microscopic strain, Γ, equal to the macroscopic strain γ. The dimensionless energy $\pm\sigma a^3 \Gamma V_0/\lambda kT$ is the adjustment to the work done on a particle as it moves to the top of the potential well with (positive sign) or against (negative sign) the shear direction; the potential well becomes skewed as illustrated in figure 3.1. Unlike the non-stressed case, however, there is now a favored state. The barrier from the strained to relaxed state is smaller than the barrier from relaxed to strained state so that on average, more particles will hop to the lower energy state resulting in a net shearing motion along the stress direction with shear rate proportional to the net frequency of forward jumps,

$$\dot{\gamma} = \frac{D}{a^2 A_2} \frac{U_{min}}{kT} e^{-U_{min}/kT} \left(\exp\left(\frac{\sigma a^3 V_0 \Gamma}{\lambda kT} \right) - \exp\left(-\frac{\sigma a^3 V_0 \Gamma}{\lambda kT} \right) \right) \tag{3.2}$$

$$= \frac{2D}{a^2 A_2} \frac{U_{min}}{kT} e^{-U_{min}/kT} \sinh\left(\frac{\sigma a^3 V_0 \Gamma}{\lambda kT} \right), \tag{3.3}$$

where A_2 is a proportionality constant that depends on the network structure. Specifically, after a pair contact is broken, reformation with another particle requires diffusion not of an isolated particle (in which case $A_2 = 1$ in Eq. (3.3)) but by diffusion of a large floc structure. For example, in the case of an isolated strained ER chain, when a pair in the center is broken, the top half reconnects with the image of the

bottom half. The diffusion is thus of a rod, not a single particle, which scales as the the cube of the rod length.

Although the relative hopping distance Γ will depend on the suspension's microstructure, e.g., densely packed flocs will result in a smaller Γ, its variation with λ (once the flocculated structure is formed) is not likely to be large (i.e., greater than order 1). Thus we estimate that $V_0\Gamma = \mathcal{F}(\phi)$, a function of ϕ, and (3.3) gives for the stress

$$\frac{a^3}{kT}\sigma \sim \frac{\lambda}{\mathcal{F}(\phi)} \sinh^{-1}\left(A_2 \frac{\dot{\gamma}a^2}{D}\frac{kT}{U_{min}}\, e^{U_{min}/kT}\right), \tag{3.4}$$

or a viscosity

$$\eta = A_1(\phi)\frac{1}{Ma} \sinh^{-1}\left(A_2 \frac{\dot{\gamma}a^2}{D}\frac{kT}{U_{min}}\, e^{U_{min}/kT}\right), \tag{3.5}$$

where $A_1(\phi)$ is a proportionality constant dependent on ϕ.

With this model we recover naturally the dimensionless quantity $(\dot{\gamma}a^2/D)(kT/U_{min})\, e^{U_{min}/kT}$ that gives the ratio of the time scale of diffusion out of a potential well of depth U_{min}/kT to the time scale of shear found in the previous section to give the shear rate below which the low-shear viscosity was reached. From (3.5) the low-shear viscosity is achieved when $(\dot{\gamma}a^2/D)(kT/U_{min})\, e^{U_{min}/kT} \ll 1$, and (3.5) correctly predicts that $\eta \to \eta_0 \sim e^{U_{min}/kT}$ as $\dot{\gamma} \to 0$.

Up to now, only the interparticle force contribution to the viscosity has been discussed since it is assumed to be the major contributor. As $\dot{\gamma} \to \infty$, however, the hydrodynamic stress dominates, and the high shear viscosity η_∞ is purely hydrodynamic. Recalling Eq. (2.14), the suspension viscosity can be approximated as

$$\eta_r - \eta_\infty = 1 + \eta_r^B + \eta_r^H + \eta_r^{SP} + \eta_r^{xF} - \eta_\infty \approx \eta_r^{SP} + \eta_r^{xF} \approx \eta_r^{xF}, \tag{3.6}$$

neglecting the Brownian and interparticle force-flow contributions. Equation (3.6) assumes $1 + \eta_r^H \sim \eta_\infty$, which is true only in the limit of infinite shear rate. For finite Ma where clusters and chains are formed, the hydrodynamic viscosity is greater than η_∞. Nonetheless, as a first approximation we model the difference of $\eta - \eta_\infty$ neglecting the contributions from Brownian forces and the flow caused by interparticle forces. Thus we can write

$$\frac{\eta - \eta_\infty}{\eta_0 - \eta_\infty} = \frac{1}{A_2 \frac{\dot{\gamma} a^2}{D\lambda}\, e^{1.57\lambda}} \sinh^{-1}\left(A_2 \frac{\dot{\gamma} a^2}{D\lambda}\, e^{1.57\lambda}\right), \tag{3.7}$$

where $\exp(1.57\lambda)$ has been substituted for $\exp(U_{min}/kT)$ and λ has been substituted for U_{min}/kT in the prefactor.

Equation 3.7 with $A_2 = 8.8$ fits the reduced curve for ER suspensions (figure 2.16) as shown in figure 3.2. The model and (3.7) should also apply for $\lambda > 10$. For example, for $\lambda = 17$, (2.23) is used to estimate η_0, the reduced viscosity is then plotted as a function of $(\dot{\gamma} a^2/D\lambda)\ e^{1.57\lambda}$, and fits onto the universal curve (figure 2.16). Similar transformations for $\lambda > 17$ are possible, but for the shear rates studied the reduced viscosity is too small to be plotted. Note that the data for $\lambda = 2.5$ and 3.3 also fall on the universal curve; at low λ, η_0 scales as e^λ from the change in the equilibrium pair-distribution function, but the characteristic time scale for this region is a^2/D.

3.2 Conclusions

In conclusion, a microstructural approach to describe the dynamics of flocculated suspensions was presented. Unlike previous phenomenological models, it incorpo-

rates the physics of the particle interactions and motion to provide a general, widely applicable, and predictive model. In this model it was hypothesized that the network rearrangement process of a flocculated suspension is rate activated. Under stress or shear, the suspension flows when particles diffuse out of their mutual potential wells, not on the bare particle diffusion time scale a^2/D, but on the escape time scale $\tau \sim (a^2/D)(kT/U_{min}) \exp(U_{min}/kT)$. As a result, the relevant dimensionless shear rate is the ratio of the escape time scale τ to the time scale of shear, or $(\dot{\gamma}a^2/D)(kT/U_{min})\ e^{U_{min}/kT}$. Our numerical simulations on ER fluids verified this hypothesis; when the shear rate was scaled with τ, a single universal curve was obtained.

Finally, it is important to note that the distinction between flocculated suspensions with an apparent yield stress and suspensions with a low-shear viscosity is an artificial one. In theory, all flocculated suspensions, including ER fluids, will flow under stress and show a low-shear viscosity. One example of this is that although we did not see a low-shear viscosity for $\lambda = 17$ over the range of Mason numbers used, the viscosity data obey the universal curve described by Equation (3.7) when Equation (2.23) is used to predict η_0. Suspensions with larger λ are also expected to have a low-shear viscosity, but at exponentially small shear rates that may not be realized in practice.

3.3 Figures

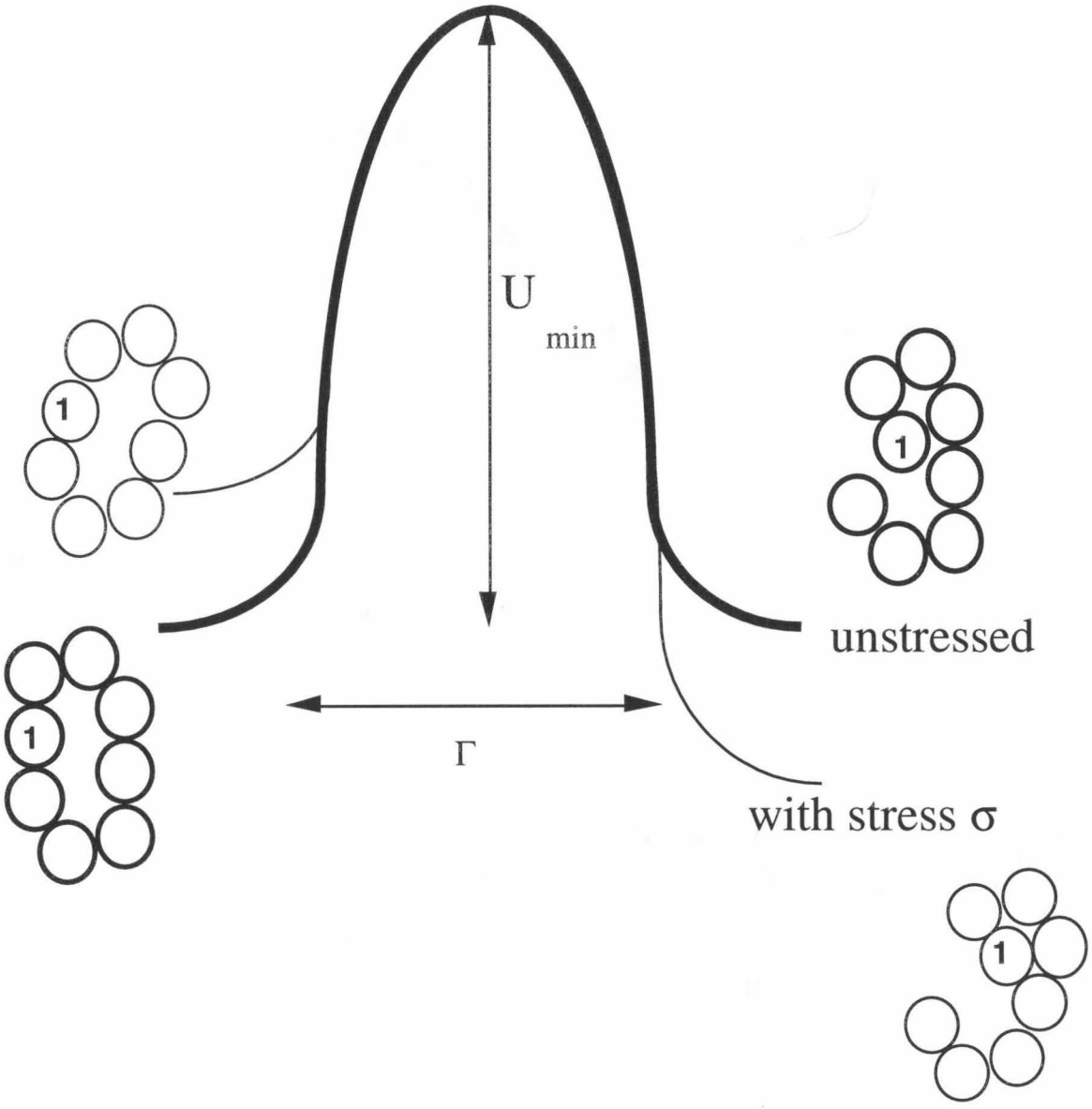

Figure 3.1: Illustration of the pair potential for a flocculated suspension. The thick lines denote the potential with no external stress, while the thin lines denote the potential with an applied stress σ. Rearrangement occurs when particle 1 hops a distance of $O(\Gamma)$.

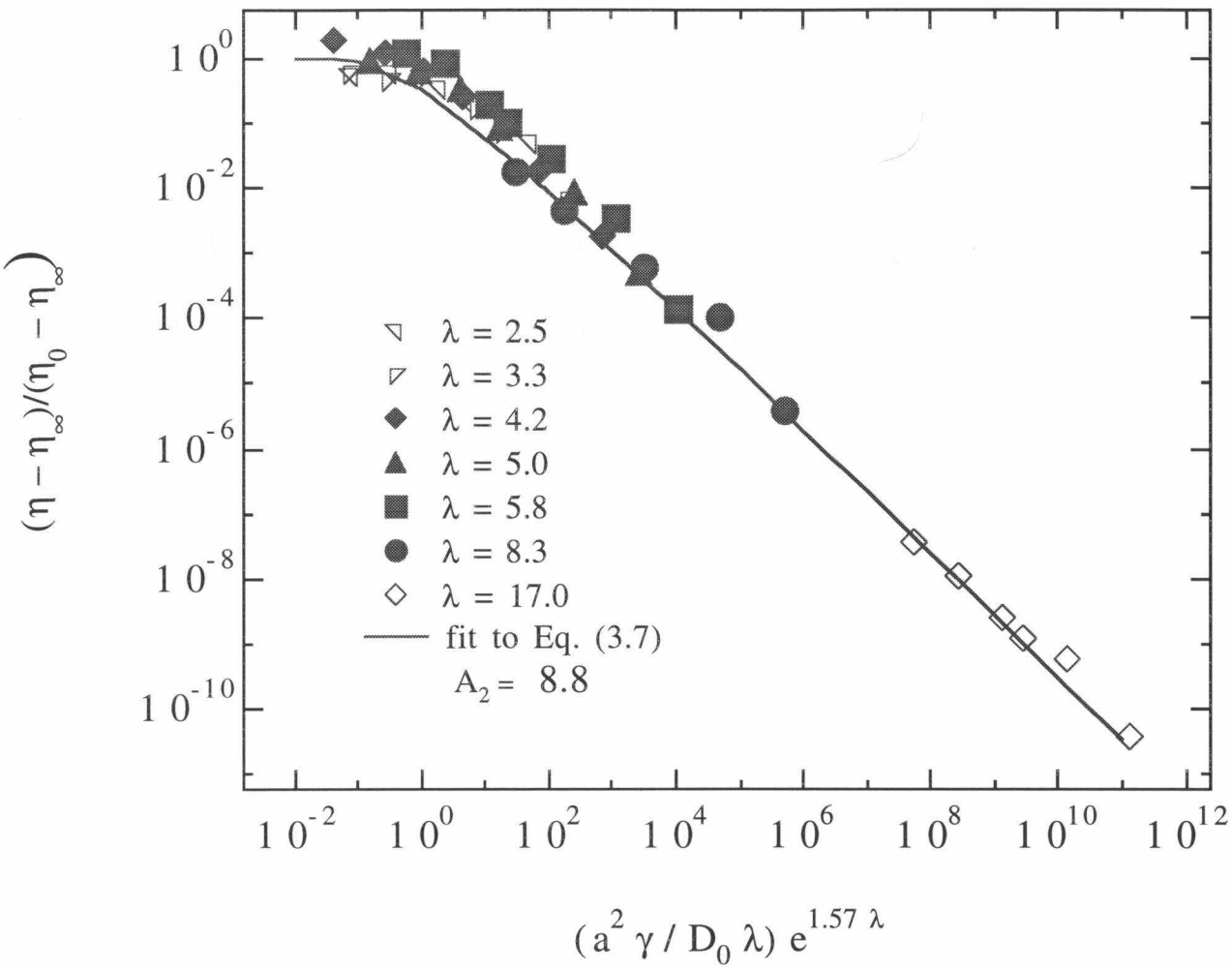

Figure 3.2: The reduced viscosity as a function of the dimensionless shear rate $(\dot{\gamma}a^2/D\lambda)\ e^{1.57\lambda}$. When the shear rate is rescaled with the escape time, τ, the data collapse onto a single curve described by Eq. (3.7) with $A_2 = 8.8$.

Chapter 4

Weakly flocculated dispersions with an isotropic potential

4.1 Introduction

The idealized two dimensional ER suspension provides a good starting point to test the model predictions. However, the salient features of the model, namely, the microstructural rearrangements and the escape time, should apply to any flocculated suspension. The work presented in this chapter aims to test the general applicability of the network model and employs two methods to accomplish this goal. First, we study a weakly flocculated suspension produced by an isotropic potential in three dimensions by Brownian Dynamics simulation neglecting hydrodynamic interactions and using simple pair-wise particle interactions. This is a highly simplified simulation scheme, but the idea is to investigate qualitatively the rheology of a suspension in three dimensions and a suspension without the anisotropy of the ER fluid. Second, we re-analyze the experimental data obtained by Buscall, McGowan & Morton-Jones (1993) for depletion flocculated suspensions.

4.2 Three-Dimensional Simulations With an Isotropic Potential

4.2.1 The Simulation Method

The simulation method is adopted from Melrose and Heyes (1993). The method was designed to mimic depletion flocculated suspensions but here it will be used simply as a representative method to produce a flocculated network without directional forcing. Melrose and Heyes studied weakly aggregating suspensions at 0.3 volume fraction with an emphasis on the suspension structure. They reported viscosities for the suspension

with pair potential well depth $24kT$ only. Here we study the suspension viscosity for a suspension at 0.3 volume fraction with pair potential minima from $5kT$ to $40kT$.

As for Electrorheological fluids, the motion of $\mathbf{N}$ particles suspended in a fluid of density ρ and viscosity η is governed by the coupled N-body Langevin equation:

$$\mathbf{m} \cdot \frac{d\mathbf{U}}{dt} = \mathbf{F}^H + \mathbf{F}^B + \mathbf{F}^P, \tag{4.1}$$

where $\mathbf{U}$ is the particle's translational/rotational velocity vector, $\mathbf{m}$ is its mass/moment of inertia tensor, $\mathbf{F}^H$ is the hydrodynamic force, $\mathbf{F}^B$ is the Brownian force, and $\mathbf{F}^P$ is the interparticle force. Hydrodynamic interactions are neglected and the hydrodynamic force is taken simply as Stokes drag,

$$\mathbf{F}^H = 6\pi\eta a \left(\mathbf{U} - \langle \mathbf{U} \rangle\right). \tag{4.2}$$

The Brownian force is characterized as "white noise,"

$$\left\langle \mathbf{F}^B \right\rangle = 0 \text{ and } \left\langle \mathbf{F}^B(0)\, \mathbf{F}^B(t) \right\rangle = 12\pi\eta a k T \mathbf{I}, \tag{4.3}$$

where the angle brackets denote an ensemble average. To calculate the interparticle force, we start with the interparticle depletion potential (Melrose & Heyes 1993),

$$\frac{U}{kT} = \sum_{ij} \left(\frac{r_{ij}}{2a}\right)^{-n} + Q\left[L^2\left(\frac{r_{ij}}{2a}\right) - \frac{1}{3}\left(\frac{r_{ij}}{2a}\right)^3 - A\right] H\left(L, r_{ij}\right), \tag{4.4}$$

where $L = 1 + \alpha/2a$, $A = 2L^3/3$, α is the diameter, or radius of gyration, of the polymer present at a volume fraction ϕ_s, and $H(L, r_{ij})$ is the heaviside step function,

$$H(L, r_{ij}) = \left\{ \begin{array}{ll} 1 & \text{if } r_{ij} < 2a + \alpha \\ 0 & \text{if } r_{ij} > 2a + \alpha \end{array} \right\}.$$

The interaction strength Q varies with ϕ_s as

$$Q = \frac{3\phi_s}{2(\alpha/2a)^3}, \tag{4.5}$$

and gives a measure of the polymer concentration and osmotic presure in the suspension due to the polymer. (Section 4.3 gives a more complete description of depletion flocculation).

A value of 36 is used for n and is somewhat arbitrary. In general, a stiff repulsion is preferred to capture the hard-sphere repulsive part of the potential. A value of 12 was found to yield artificially low potential minima and anomalous rheology results (Melrose & Heyes 1993), while $n = 36$ does not produce these anomalities.

For $\alpha/2a = 1/11$ and $n = 36$, $\phi_s = 0.26, 0.4, 0.51, 0.7$, and 1.0 give potential minima of $5, 10, 15, 24$, and 40 respectively as shown in figure 4.1. There is a shift in the particle core radius from 0.96 to 0.94 for U_{min} from $5kT$ to $40kT$, respectively. The effective volume fraction, taking the core diameter as the diameter at U_{min}, decreases slightly from the nominal 0.3 to 0.24 for $U_{min} = 40kT$ but this should not qualitatively affect the results.

The interparticle force can be calculated as

$$\frac{a\mathbf{F}^P}{kT} = -\frac{\partial U}{\partial r} \tag{4.6}$$

$$= Q\,\mathbf{F}^{attractive} + \mathbf{F}^{repulsive} \tag{4.7}$$

$$= -\frac{Q}{2}\left[L^2 - \left(\frac{r_{ij}}{2a}\right)^2\right] H(L, r_{ij}) + 18\left(\frac{r_{ij}}{2a}\right)^{-37}, \tag{4.8}$$

if $r < 2a\alpha$, and Eq. (4.1) can be integrated to give

$$\Delta\mathbf{x} = Pe\left[\langle\mathbf{U}\rangle + \frac{Q}{Pe}\mathbf{F}^{attr} + \frac{1}{Pe}\mathbf{F}^{rep}\right]\Delta t + \mathbf{X}(\Delta t), \tag{4.9}$$

where $\langle \mathbf{X} \rangle = 0$ and $\langle \mathbf{X}(\Delta t)\mathbf{X}(\Delta t) \rangle = 2\mathbf{I}\Delta t$. Here, x has been made non-dimensional by a and t by a^2/D. The dimensionless parameter Pe/Q is a dimensionless shear rate and plays a role similar to the Mason number, Ma, for ER fluids. However, unlike λ for ER fluids, Q is not a good estimate of U_{min}/kT as the particles are not true hard spheres. For example, for $\alpha/2a = 1/11$, $n = 36$, $\phi_s = 0.4$, and $Q = 798.6$, the pair potential well depth is $10kT$. Table 4.1 gives values for Q with corresponding values for U_{min}/kT. Equation (4.9) is the core of the simulation and is used to follow the motion of N particles given their initial configuration.

For the suspension rheology, the suspension stress is needed and can be calculated as

$$\langle \mathbf{\Sigma} \rangle = -\frac{1}{2V} \sum_{\alpha=1}^{N} \sum_{\beta=1}^{N} (\mathbf{x}_\alpha - \mathbf{x}_\beta) \left(\mathbf{F}_{\alpha\beta}^{attr} + \mathbf{F}_{\alpha\beta}^{rep} \right). \tag{4.10}$$

There is neither a hydrodynamic nor a Brownian contribution to the stress since hydrodynamic interactions are neglected. The only contribution comes from the interparticle force, i.e., the familiar **xF** stress. The relative viscosity of the suspension is defined by the ratio of the yx component of the bulk stress to the yx component of the bulk rate of strain, with the imposed flow $\langle U_x \rangle = \dot{\gamma} y$. In dimensionless form

$$\eta_r = 1 + \frac{5}{2}\phi + \eta_r^{xF}, \tag{4.11}$$

where $\frac{5}{2}\phi$ is the Einstein contribution.

4.2.2 Results and Discussion

The method outlined above was applied to an unbounded $3D$ suspension of monodispersed particles with shear in the **x**-direction, shear gradient in the **y**-direction, and

vorticity in the **z**-direction. The unbounded suspension is simulated by periodically replicating 27 identical spherical particles in a cubic cell forming a 0.3 volume fraction suspension. A spherical cut-off of $2a + \alpha$ is used for both the attractive and repulsive forces. The suspension viscosity is studied for $5 \leq U_{min}/kT \leq 40$ and $2 \cdot 10^{-5} \leq Pe \leq 100$. Steady state was determined by monitoring the time average viscosity.

For a suspension without shear, at a volume fraction of 0.3, and with $\alpha/2a = 1/10$, a transition from fluid to flocculated is predicted at a polymer concentration of $\phi_s \approx 0.15$ and confirmed by experiment (Gast et al. 1983, 1986). Since we are primarily interested in the flocculated suspension dynamics, a minimum ϕ_s of 0.26 and $\alpha/2a = 1/11$ are used to yield a suspension with a pair potential minimum of $5kT$. This suspension has been shown to be flocculated while quiescent and to remain flocculated under low to moderate shear (Melrose & Heyes 1993). To further ensure the potential range is outside the dispersed regime, the pair potential function at contact, $g(2)$, is determined for the quiescent suspension and is plotted as a function of U_{min}/kT in figure 4.2. For $U_{min} < 5kT$ the pair potential function at contact scales exponentially with U_{min}/kT. For $U_{min}/kT \geq 5$, however, $g(2)$ saturates and is roughly independent of U_{min}/kT.

Figure 4.3 gives the suspension viscosity as a function of Pe/Q for $5 \leq U_{min}/kT \leq 40$. The corresponding data are given in table 4.2. At high shear rates, the viscosity is Newtonian and independent of the particle potential minimum. As the shear rate decreases, the viscosity increases and there is a shear thinning regime at intermediate

shear rates. Of primary interest is the low-shear viscosity for $U_{min}/kT = 5$ and 10. For $U_{min}/kT = 15$, the viscosity appears to be approaching a low-shear plateau, while for $U_{min}/kT = 24$ and 40 the shear rates studied are not low enough to observe the low-shear behavior. The low-shear viscosity for $U_{min}/kT \leq 15$ scales exponentially with the pair potential well depth (figure 4.4), similar to the low-shear viscosity for Brownian ER fluids discussed in Chapter 2. (Note that the value at $U_{min}/kT = 15$ is approximate as only the beginning of a plateau was seen for the shear rates studied). In addition, the shear rate at which the low-shear limiting behavior occurs scales *inversely* with the exponential of the pair potential minimum as shown in figure 4.5, i.e., the low-shear-rate-asymptote is reached for shear rates that decrease exponentially as $e^{-0.76U_{min}/kT}$. The results for $U_{min}/kT = 24$ compare only qualitatively to Melrose & Heyes' results (1993). Melrose & Heyes found a lower limiting low-shear viscosity, (15), at much higher shear rates, ($Pe/Q \approx 10^{-3}$). The reason for the difference between their results and ours is unclear but we note that Melrose & Heyes used a much larger system of 500 particles, and their shear rates were not as low as those reported here.

To test the model presented in the previous chapter, the reduced viscosity is plotted as a function of the reduced shear rate, $Pe(kT/U_{min})\exp(0.65U_{min}/kT)$, in figure 4.6. Firstly, the data for $U_{min} > 5kT$ collapse onto a single curve. The results for $U_{min} = 5kT$ do not fit the reduced curve well possibly because $5kT$ marks the approximate transition from dispersed to flocculated for this suspension. Secondly,

the reduced curve has the same form as the predicted equation (3.7);

$$\frac{\eta - \eta_\infty}{\eta_0 - \eta_\infty} = \frac{1}{A_2 \frac{\dot{\gamma}a^2}{D} \frac{kT}{U_{min}} e^{0.65 U_{min}/kT}} \sinh^{-1}\left(A_2 \frac{\dot{\gamma}a^2}{D} \frac{kT}{U_{min}} e^{0.65 U_{min}/kT} \right) \tag{4.12}$$

with the network dependent constant $A_2 = 12$.

4.3 Depletion Flocculated Suspensions by Buscall, McGowan & Morton-Jones

Depletion flocculation is achieved by dissolving a non-adsorbing polymer in a dispersion. The nature of the interparticle potential depends on the interaction between the polymer and the suspended particles. Interactions between the suspended particles at separations less than the dissolved chain dimension drives the polymer from the gap. Since the osmotic pressure is proportional to the polymer concentration (for dilute polymer concentrations), and the integration of this normal force over the surface yields the net force; there is now a deficit in the osmotic pressure and an attractive force between the particles.

Buscall et al.'s suspension consisted of a non-aqueous polymer latex in a low-aromatic white spirit flocculated by adding a soluble non-adsorbing polymer, and the apparent pair potential well depth was varied by changing the soluble polymer concentration. Once slip at the rheometer plates was eliminated, they found that the low-shear viscosity increased exponentially with the potential well depth for well depths from $2kT$ to $25kT$. Buscall et al. estimated the apparent pair potential associated with depletion flocculation using the Asakura & Oosawa equation (Asakura & Oosawa 1954, Gast et al. 1983) and the results are reproduced here in figure 4.7.

Figure 4.8 shows the apparent shear viscosity as a function of $Pe(kT/U_{min})$ for U_{min}/kT from 2 to 25. The dimensionless shear rate $Pe(kT/U_{min})$ is the ratio for the time scale of aggregation due to the polymer to the time scale of shear, and plays a similar role to the Mason number for ER fluids. The suspension viscosity reaches a low-shear plateau similar to that seen for ER fluids and for suspensions with a general isotropic potential as discussed in the previous section. The low-shear viscosity, taken from Buscall et al.'s paper, scales exponentially with the pair potential minimum as shown in figure 4.9, with

$$\eta_0 = 7.5 \exp(0.55\ U_{min}/kT). \tag{4.13}$$

Buscall and co-workers observed that the critical stress at which the low-shear behavior is observed scales as the square of the polymer concentration. However, as shown in figure 4.10, the critical shear rate at which the low-shear limiting behavior is observed scales inverse exponentially with the pair potential well depth, suggesting instead a linear dependence of the critical stress with the pair potential well depth and the polymer concentration.

The reduced viscosity $(\eta - \eta_\infty)/(\eta_0 - \eta_\infty)$ is plotted as a function of the reduced shear rate $Pe(kT/U_{min}) \exp(0.55 U_{min}/kT)$ in figure 4.11, and a single curve is obtained. Equation (4.13) was used to calculate η_0.

The reduced curve has the same form as the predicted equation (3.7);

$$\frac{\eta - \eta_\infty}{\eta_0 - \eta_\infty} = \left(\frac{1}{A_2 \frac{\dot{\gamma} a^2}{D}}\right) \left(\frac{kT}{U_{min}}\right) \sinh^{-1} \left(A_2 \frac{\dot{\gamma} a^2}{D} \frac{kT}{U_{min} e^{0.55 U_{min}/kT}}\right) \tag{4.14}$$

with the network dependent constant $A_2 = 15$.

4.4 Conclusions

In this chapter, the network model presented in Chapter 2 was tested for its general applicability. This was accomplished by a study of the rheology of a three dimensional flocculated dispersion with an isotropic potential by Brownian Dynamics simulation, and by using the experimental results of a depletion flocculated suspension by Buscall et al. (1993). In both cases there was a low-shear rate regime at shear rates that scale inverse exponentially with the pair potential well depth, U_{min}/kT. The low-shear viscosity in this regime scaled exponentially with the pair potential well depth, $\eta_0 \sim \exp(U_{min}/kT)$. When the reduced viscosity was plotted as a function of the new shear rate, $Pe(kT/U_{min})\exp(\beta U_{min}/kT)$, the data collapsed onto a single curve that can be described by the model with the network dependent constant $A_2 = 12$ for our Brownian Dynamics simulations with an isotropic potential, and $A_2 = 15$ for Buscall et al.'s data. This is further evidence that the model captures the essential features of flocculated networks and can be used to describe flocculated dispersions generally.

4.5 Tables

Table 4.1: The dimensionless parameter Q and corresponding U_{min}/kT.

Q	U_{min}/kT
519	5
798.6	10
1018.2	15
1397.6	20
1996.5	40

Table 4.2: The suspension viscosity for $5 \leq U_{min}/kT \leq 40$. Statistical information is omitted where sampling is insufficient to produce meaningful standard deviations.

Pe	U_{min}/kT				
	5	10	15	24	40
$5 \cdot 10^{-4}$			1720		
10^{-3}		106	1190	3470	
$5 \cdot 10^{-3}$		83.9 ± 30.2	413 ± 209		
0.01		75.4 ± 73.5	75.2 ± 59.5	388 ± 141	256 ± 393
0.1		9.51 ± 18.3	8.50 ± 12.1	37.9 ± 6.13	34.1 ± 47
0.5	2.49 ± 2.9				
1.0	2.47 ± 2.11	2.83 ± 1.56	4.00 ± 2.03	3.99 ± 5.03	7.86 ± 0.41
10.0	1.85 ± 0.12	1.96 ± 0.23	2.11 ± 0.32	2.21 ± 0.445	2.41 ± 0.81
100.0	1.79 ± 0.024	1.79 ± 0.031	1.81 ± 0.041	1.82 ± 0.06	1.85 ± 0.078

4.6 Figures

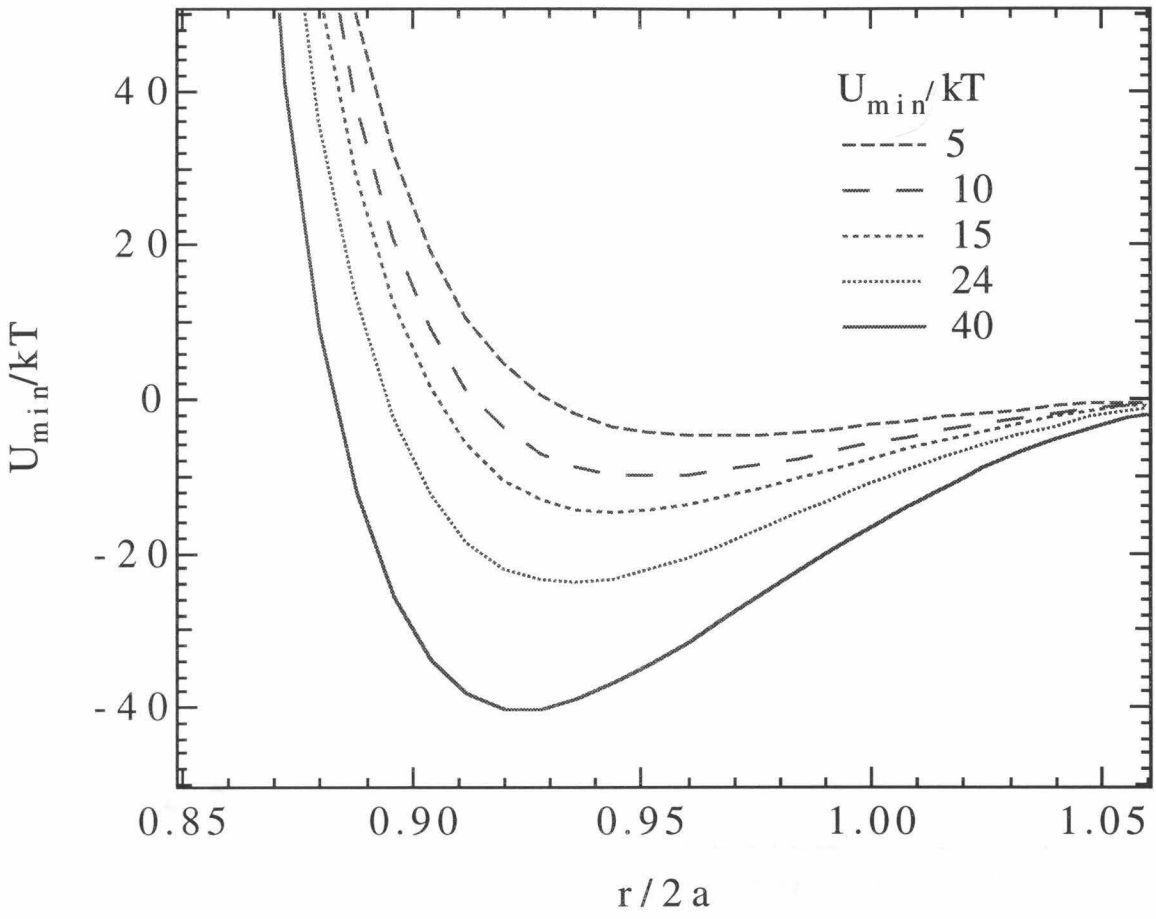

Figure 4.1: The isotropic pair potential used for the simulations. There is a shift in the particle core radius from 0.96 to 0.94 for U_{min} from $5kT$ to $40kT$ respectively that causes a decrease in the particle volume fraction from 0.3 to 0.24 for $U_{min}/kT = 40$.

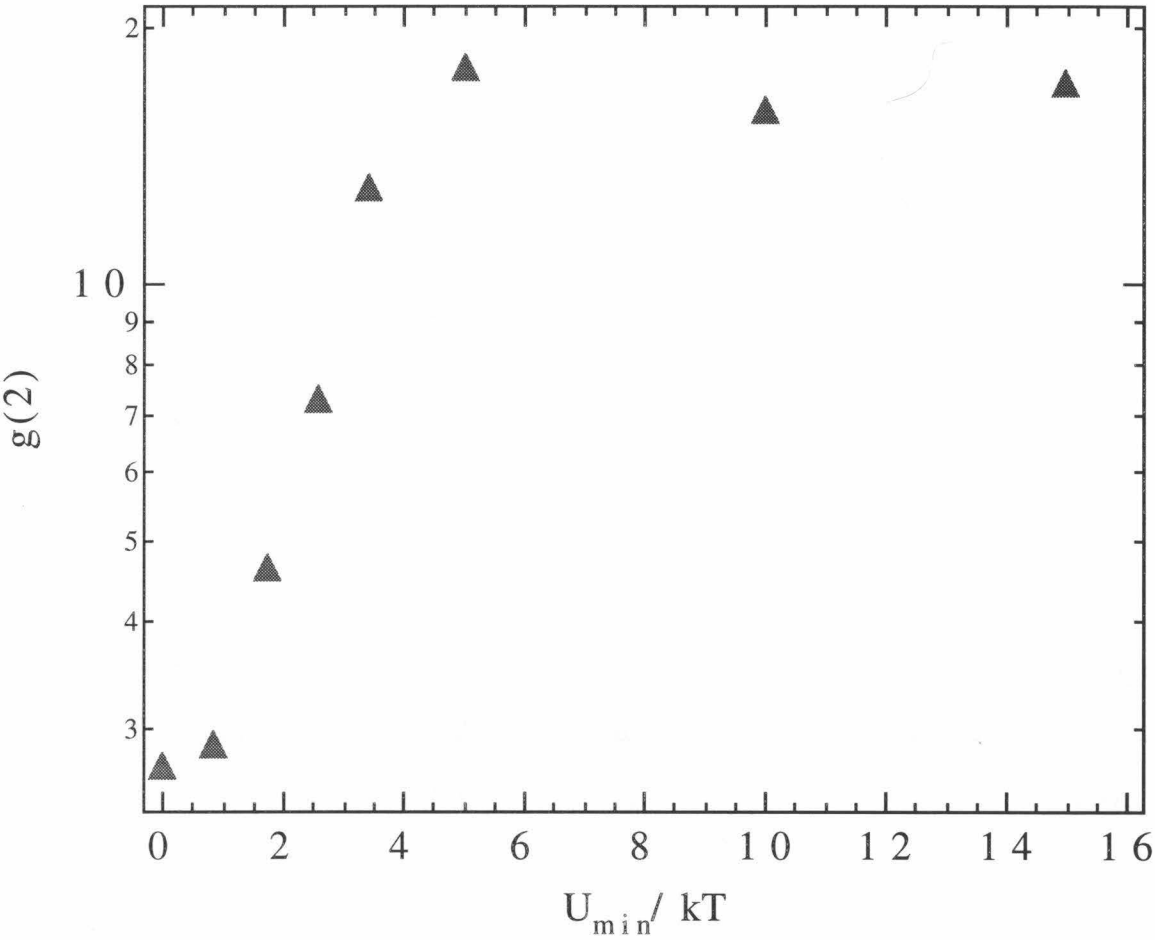

Figure 4.2: The pair potential function at contact, $g(2)$, vs. U_{min}/kT. For $U_{min} < 5kT$ the pair potential function at contact scales exponentially with U_{min}/kT. For $U_{min}/kT > 5$, however, $g(2)$ saturates and is independent of U_{min}/kT.

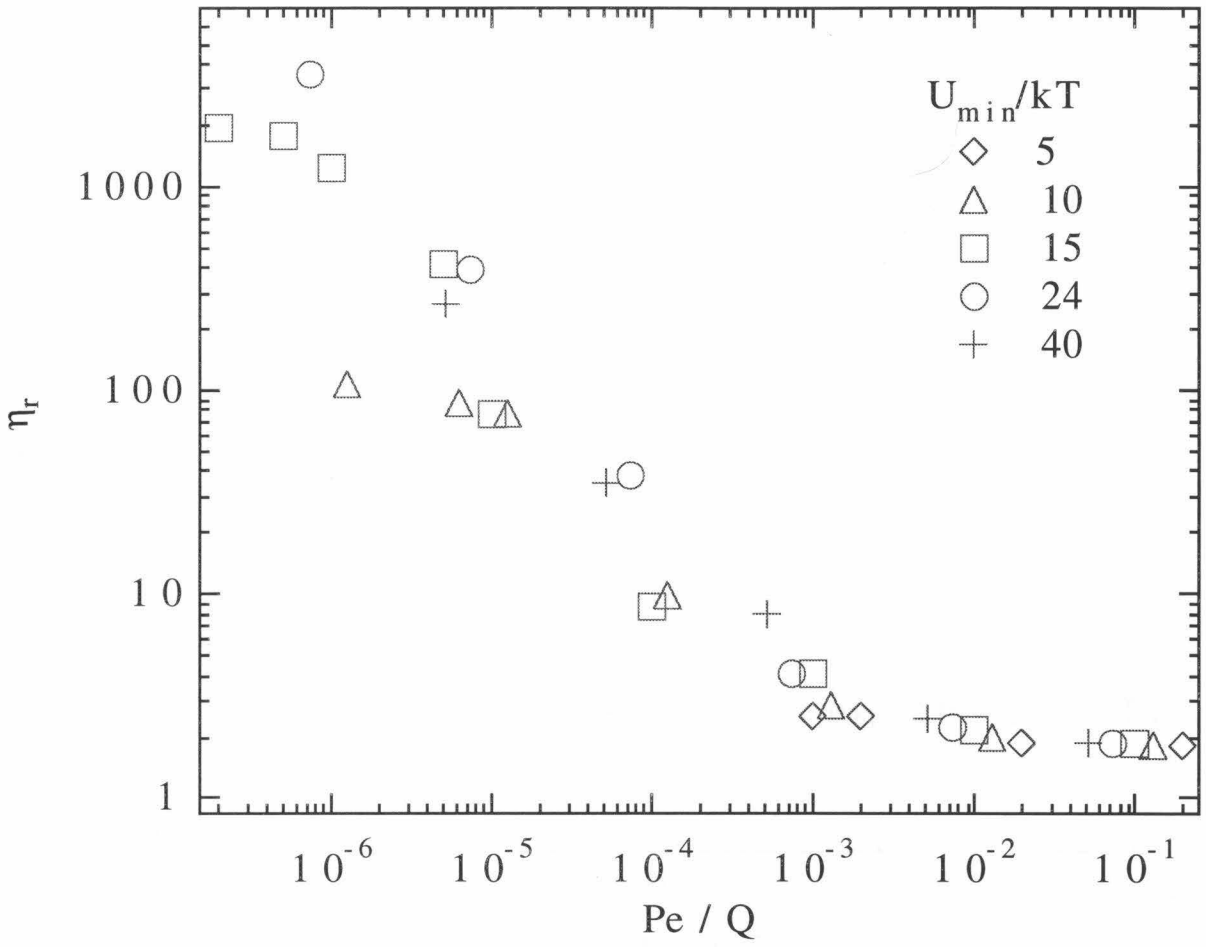

Figure 4.3: The suspension viscosity as a function of Pe/Q) for $5 \leq U_{min}/kT \leq 40$. At high shear rates, the viscosity is Newtonian and independent of the pair potential minimum. As the shear rate decreases, the viscosity increases and has a shear thinning regime at intermediate shear rates. There is a clear low-shear viscosity for $U_{min}/kT = 5$ and 10. For $U_{min}/kT = 15$, the viscosity appears to be approaching a low-shear plateau, while for $U_{min} = 24$ and 40 the shear rates studied are not low enough to observe the low-shear behavior.

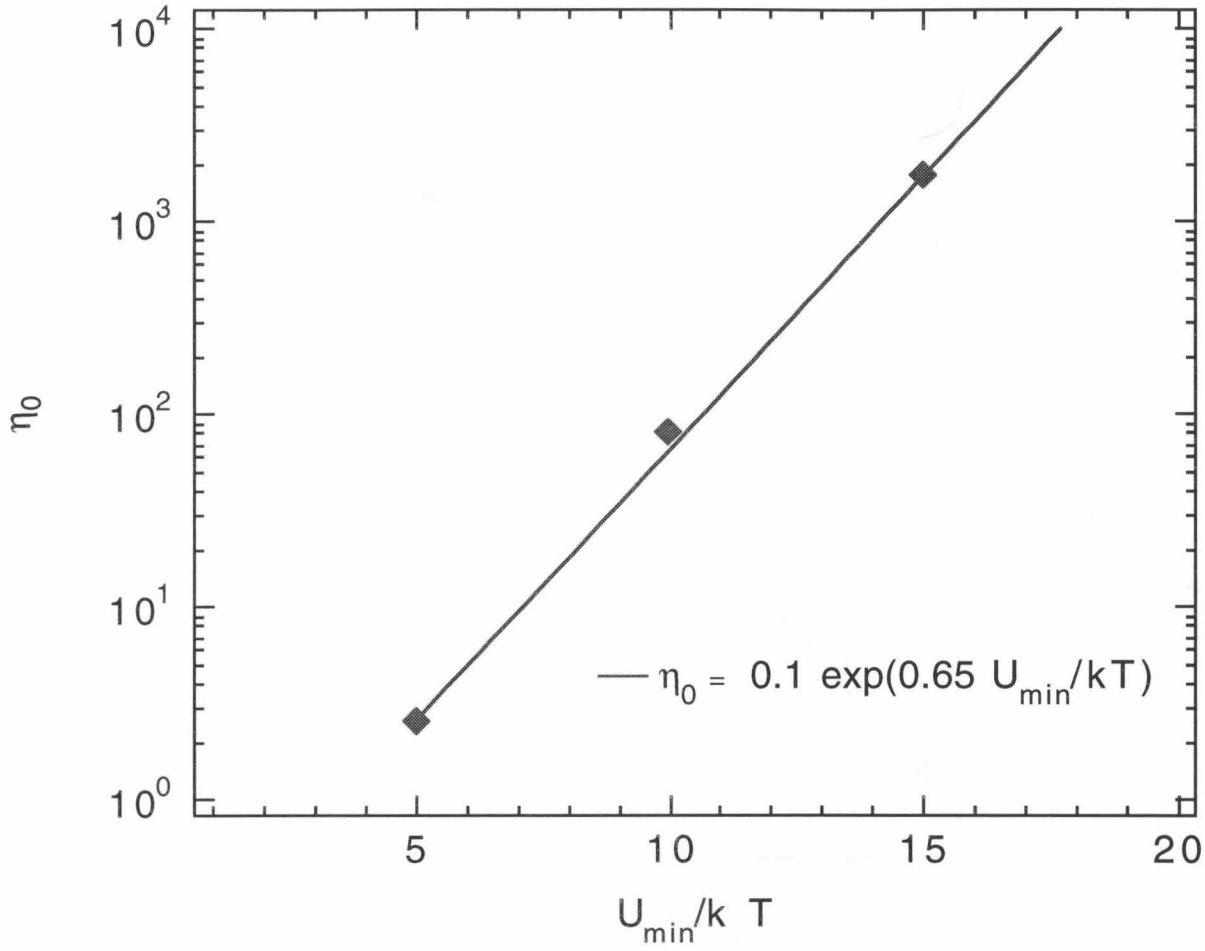

Figure 4.4: The low-shear viscosity as a function of the pair potential well depth. The low-shear viscosity scales exponentially with the pair potential well depth similar to the low-shear viscosity for Brownian ER fluids discussed in Chapter 2. The low-shear viscosity at $U_{min}/kT = 15$ is approximate, as only the beginning of a plateau was seen at the shear rate studied.

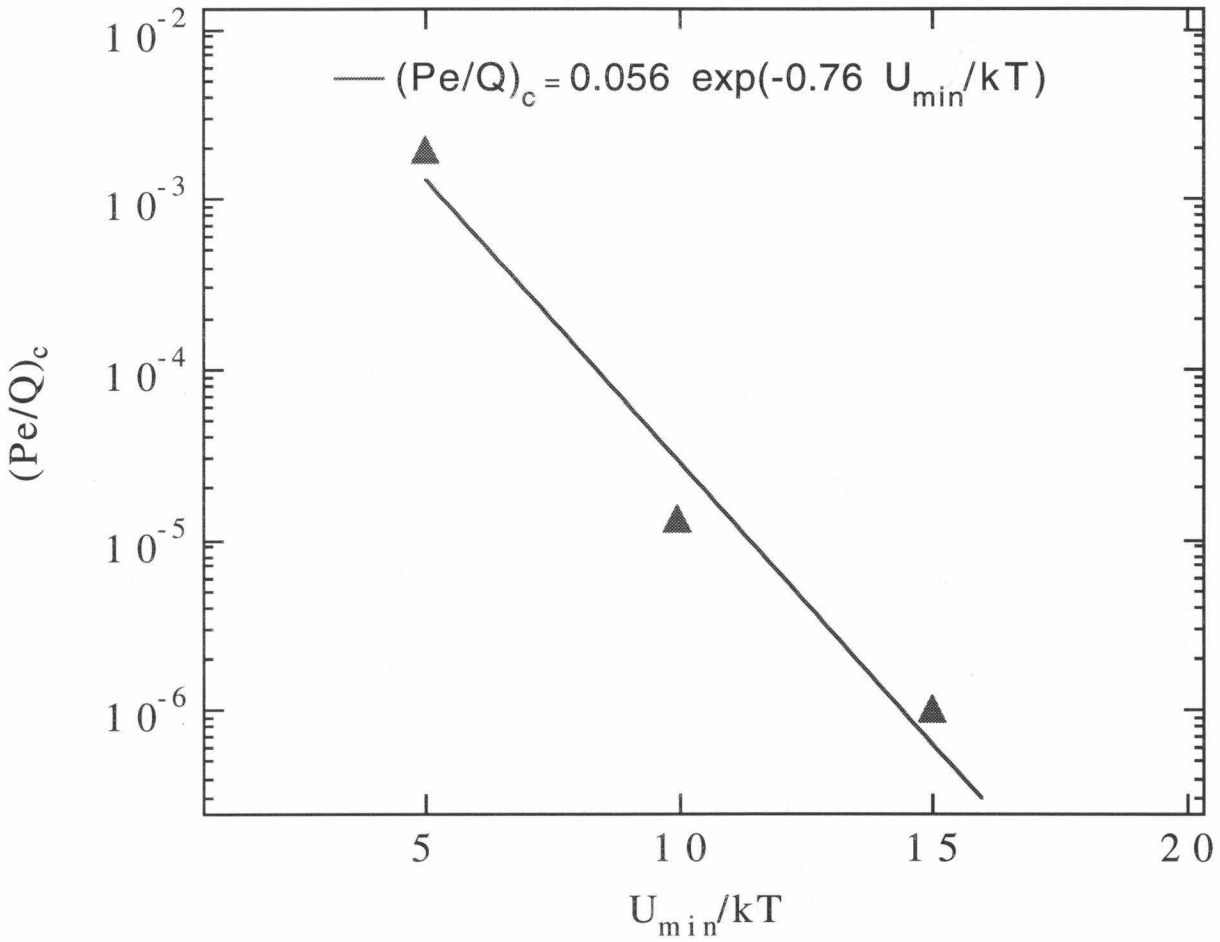

Figure 4.5: The shear rate where the low-shear limiting behavior is seen as a function of the pair potential well depth. We again see that the shear rate scales *inversely* with the exponential of the pair potential minimum.

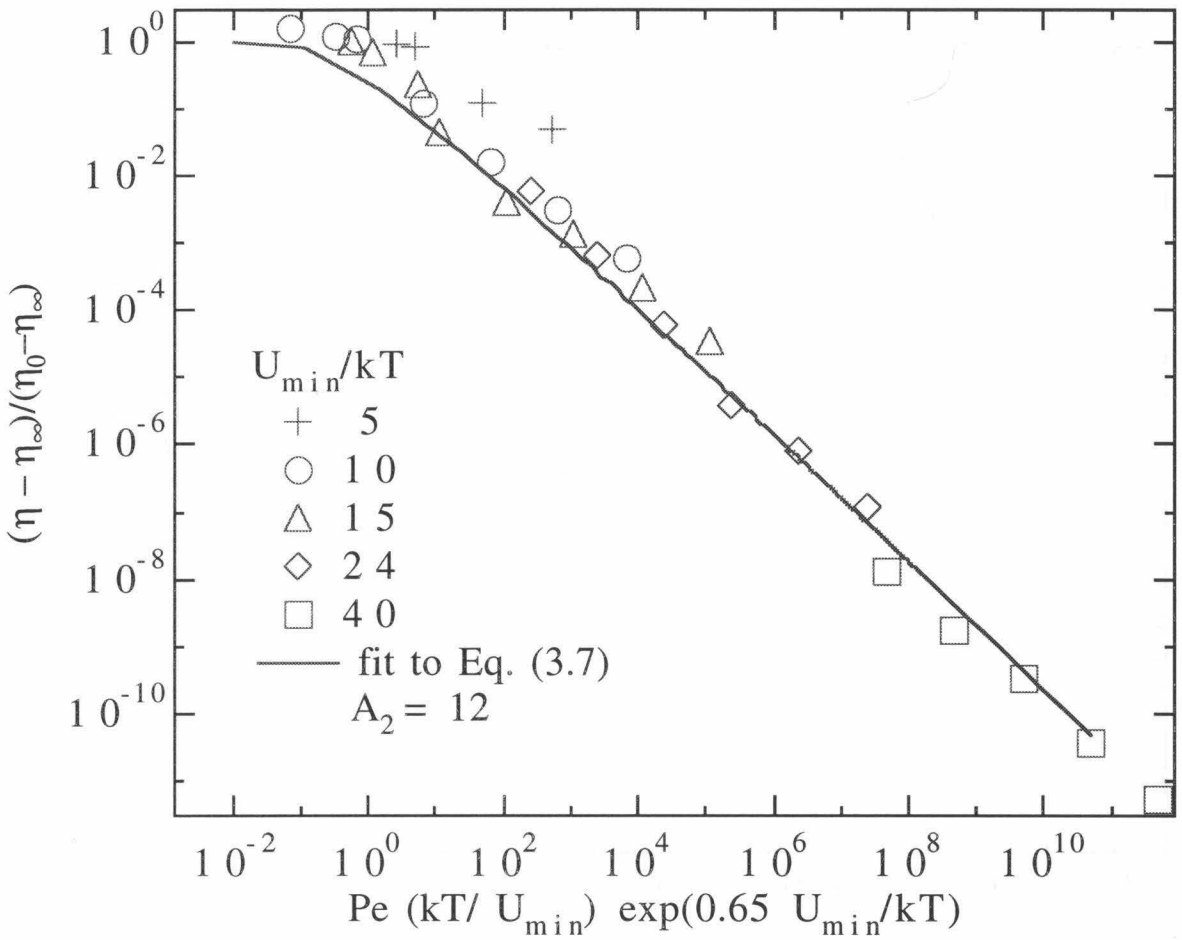

Figure 4.6: The reduced viscosity as a function of the reduced shear rate. The data collapse onto a single curve, and has the same form as the predicted equation (3.7), with the network dependent constant $A_2 = 12$.

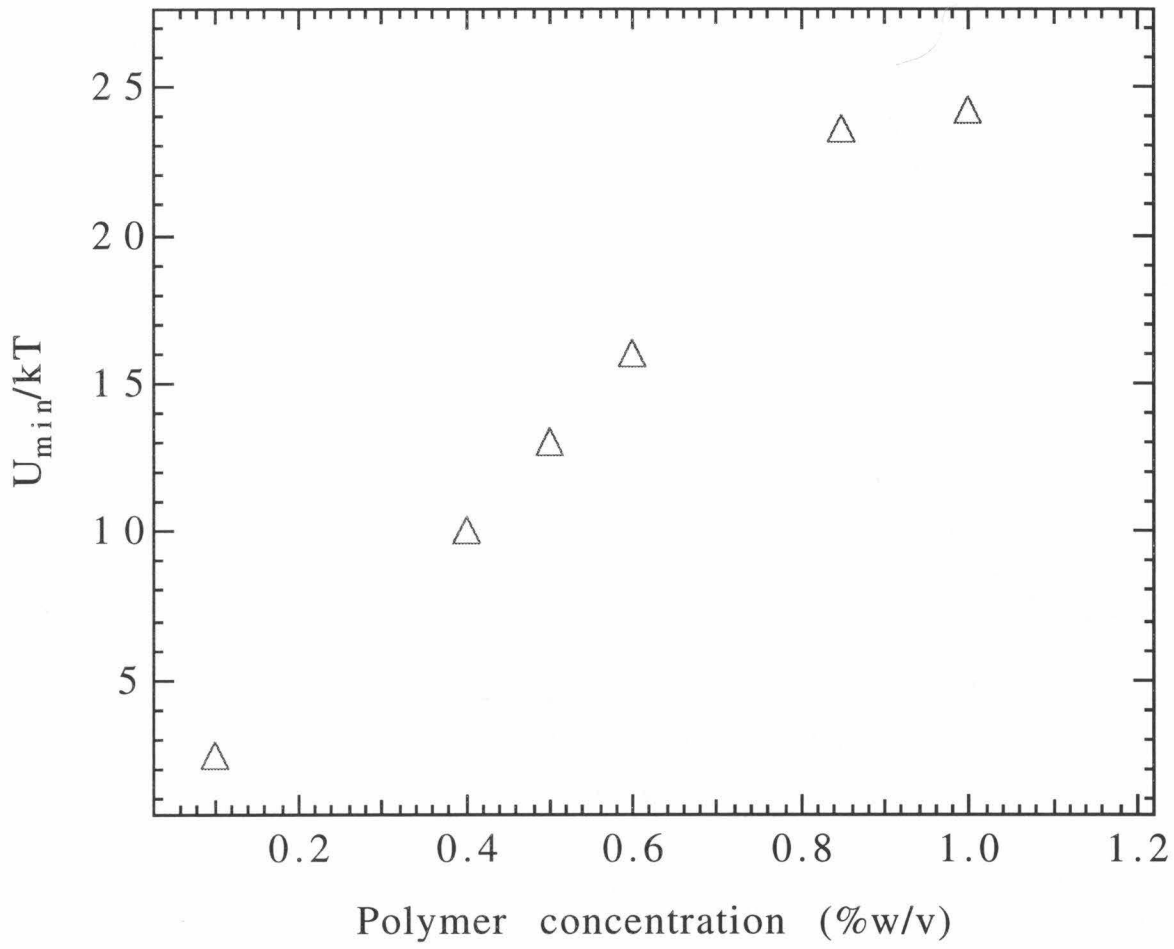

Figure 4.7: The pair potential well depth as a function of the PIB concentration.

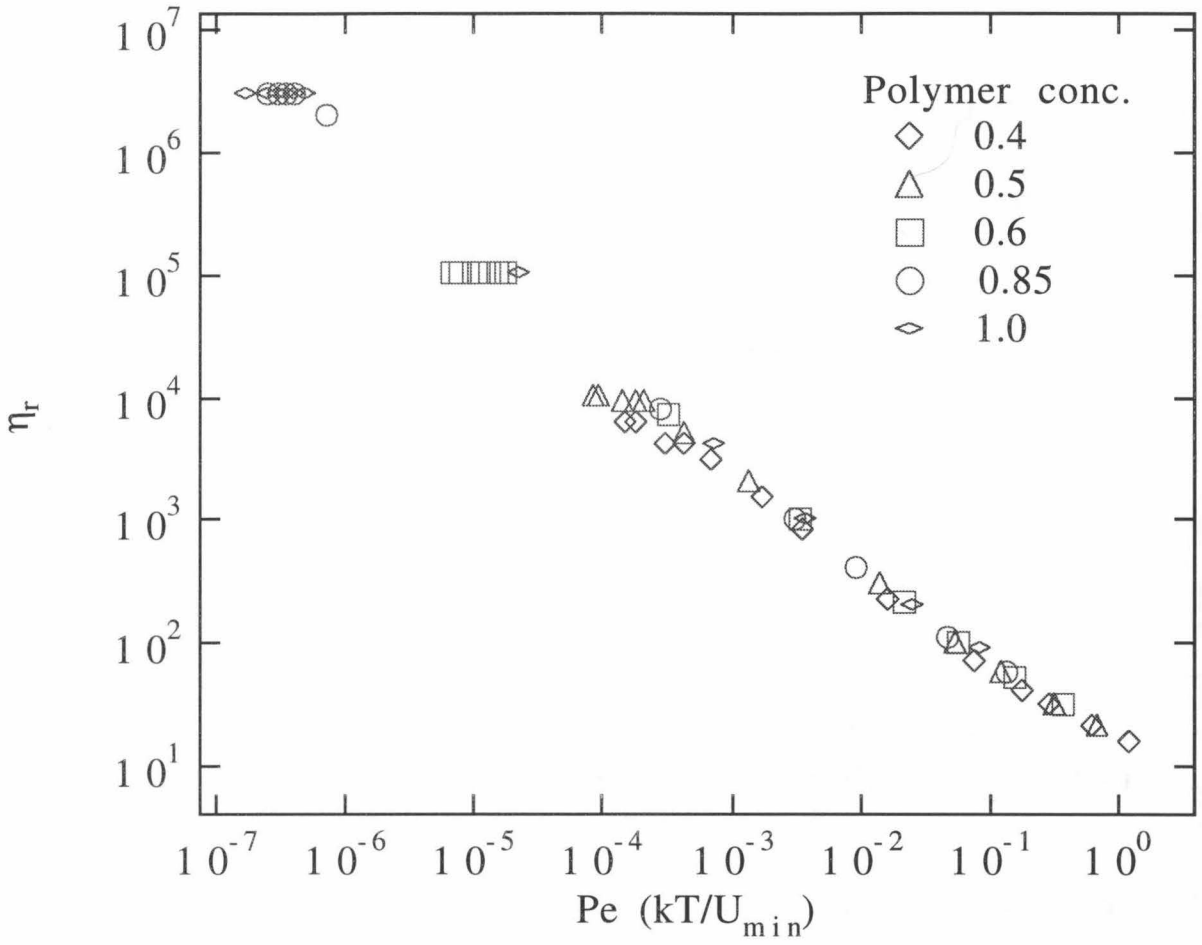

Figure 4.8: The apparent shear viscosity as a function of $Pe(kT/U_{min})$ for U_{min}/kT from 10 to 25. The data points are taken from Buscall et al. (1993). The dimensionless shear rate $Pe(kT/U_{min})$ is the ratio for the time scale of aggregation due to the polymer to the time scale of shear and plays a similar role to the Mason number for ER fluids. The suspension viscosity reaches a low-shear plateau similar to that observed for ER fluids and for suspension with a general isotropic potential discussed in the previous section.

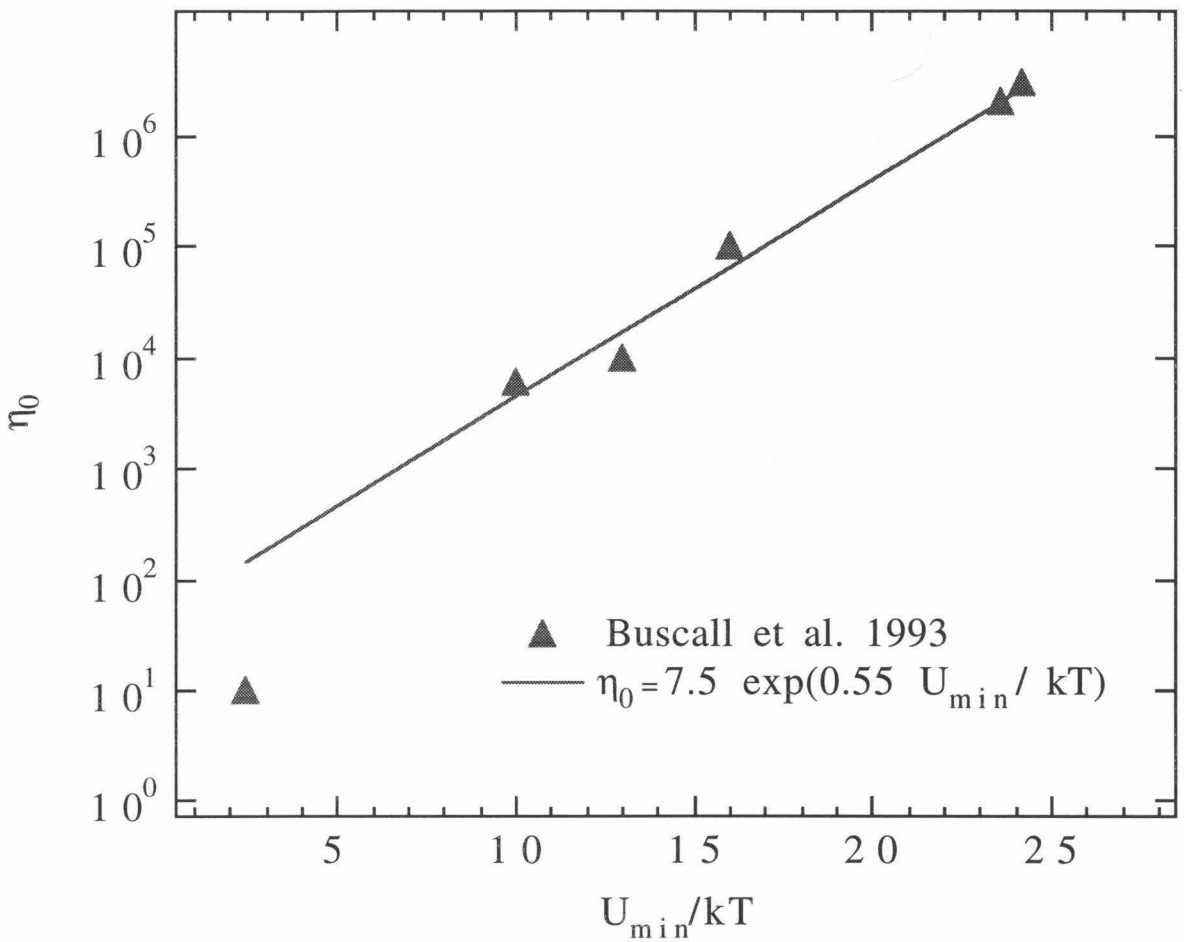

Figure 4.9: The low-shear viscosity vs. the pair potential minimum for Buscall et al.'s data. The low-shear viscosity scales exponentially with the pair potential minimum.

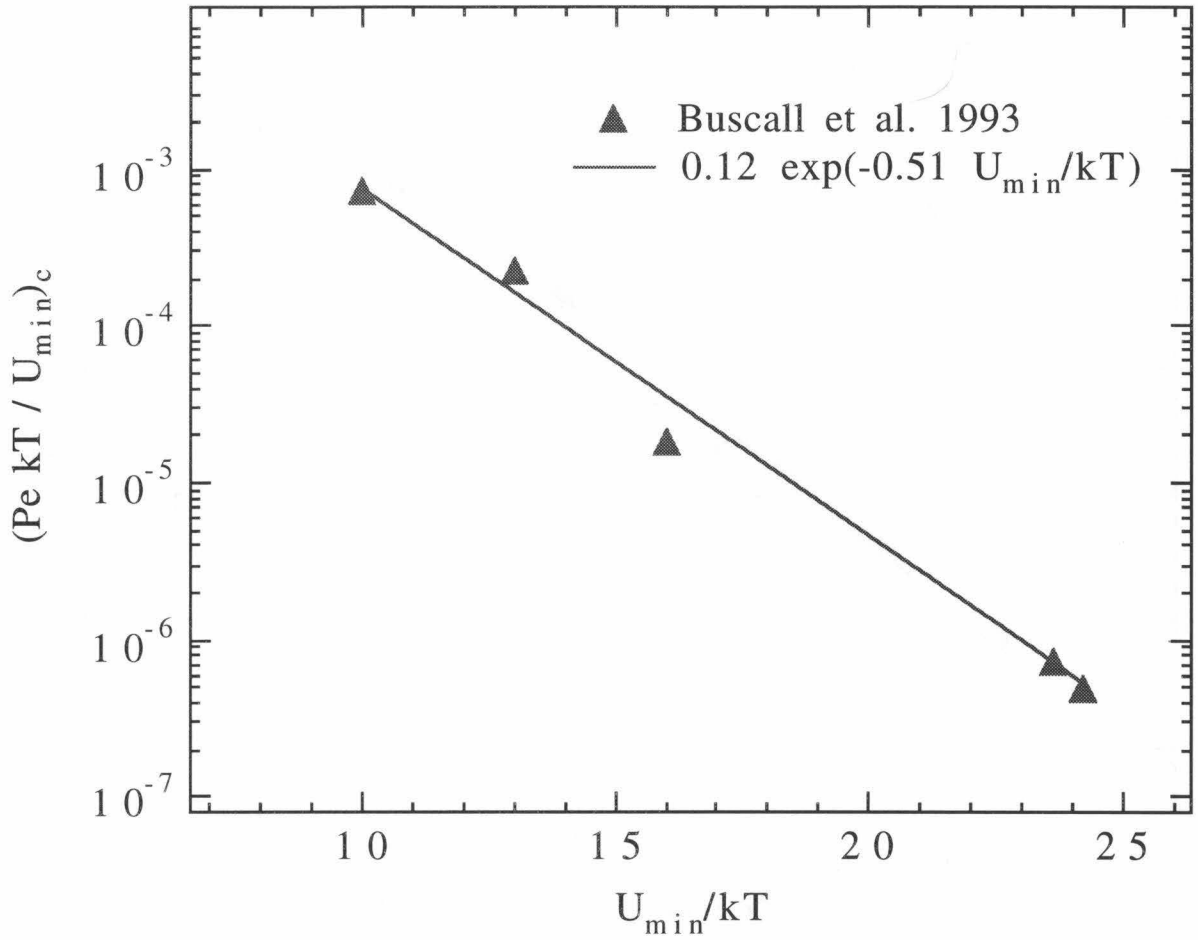

Figure 4.10: The critical shear rate where the low-shear limiting behavior is observed for Buscall et al.'s data. The shear rate scales inverse exponentially with the pair potential well depth for $U_{min}/kT \geq 10$.

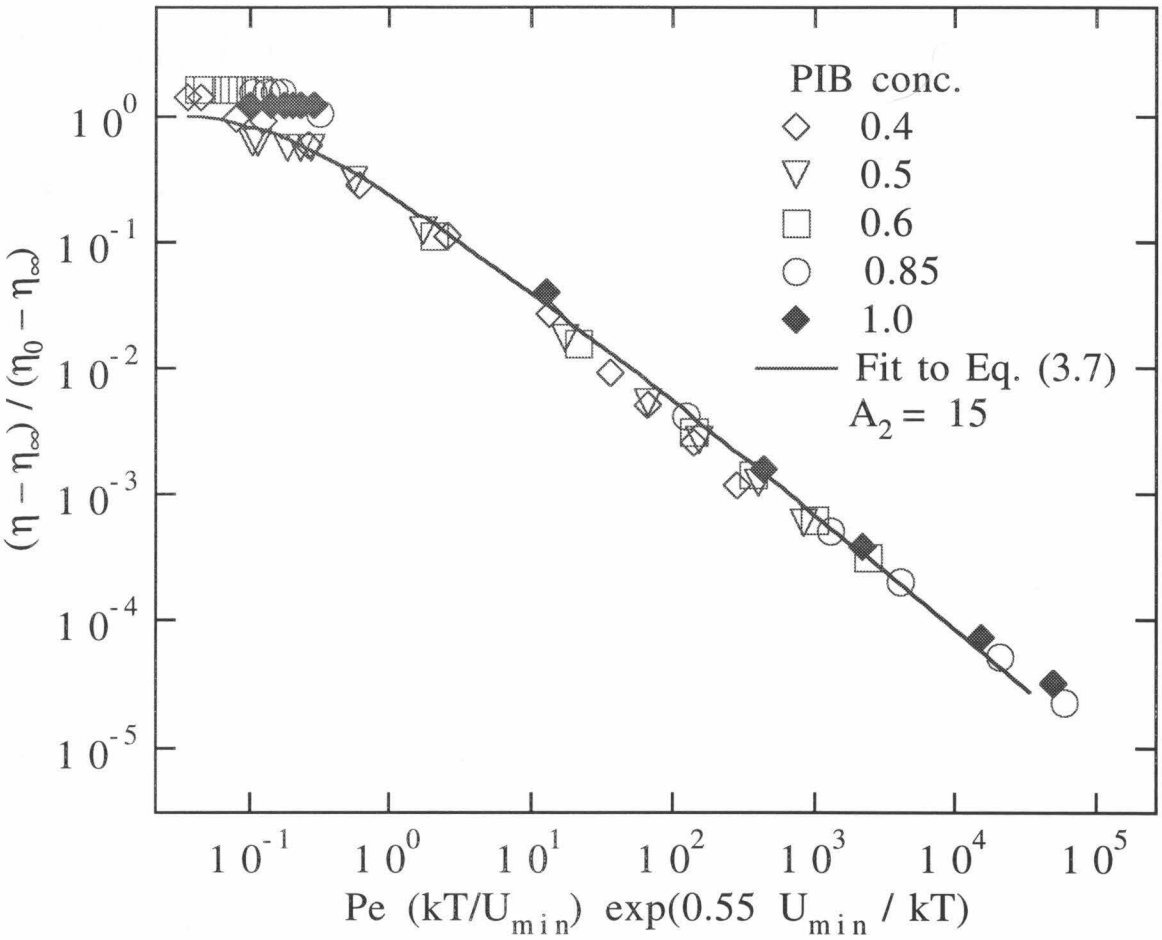

Figure 4.11: The reduced viscosity as a function of the reduced shear rate $Pe\ (kT/U_{min})\exp(0.55\ U_{min}/kT)$. A single curve is obtained that has the same form as the predicted curve (3.7), with the network dependent constant $A_2 = 15$.

Chapter 5

Concluding remarks

This thesis aims to elucidate the dynamic behavior of flocculated suspensions. To this end, the rheological behavior of Electrorheological fluids was first studied as a model suspension for flocculated colloidal dispersions using a molecular dynamic-like simulation method, Stokesian Dynamics. The ER suspension was particularly well suited as a model suspension as its interparticle potential can be varied easily by simply changing the applied field strength. Also, the suspension microstructure essentially consists of chains aligned along the field direction and facilitates correlation between the suspension microstructure and the suspension dynamics.

Under simple shear flow the dispersed, $\lambda < 4$, and weakly flocculated, $4 < \lambda < 10$, ER suspension, have a low-shear viscosity that scales exponentially with λ, but for different reasons. When dispersed, the exponential scaling of the low-shear viscosity with λ comes from the pair distribution function which scales as e^{λ}, but the relaxation time is the bare diffusion time, a^2/D. This is not the case when the suspension is flocculated. Previously, three times scales have been used to describe the dynamics of flocculated ER fluids: τ_B, the Brownian time that gives the time of diffusion of an *isolated* Brownian particle, τ_{ER}, the electrostatic time that gives the time scale of aggregation due the applied field, and τ_V, the viscous time that gives the time scale of shear. In fact, the time scale that proves most relevant to aggregated suspension is the escape time first proposed by Kramers (1940), $\tau \sim (a^2/D)(kT/U_{min}) \exp(U_{min}/kT)$. The escape time gives the time for two particles in a mutual potential well of depth U_{min}/kT, with $U_{min}/kT \gg 1$, to escape by diffusion from their well, and the suspension viscosity is now set by this escape time. The result is that the low-shear viscosity

scales as e^{λ}.

A new dimensionless shear rate can be defined as $(\dot{\gamma}a^2/D)(kT/U_{min})\exp(U_{min}/kT)$ and replaces the Mason number as the dimensionless shear rate of choice for ER suspensions. When the reduced viscosity is plotted as a function of this new shear-rate, a single curve is produced. Although there have been previous discussions of the escape time as it relates to weakly aggregated suspension dynamics, this is the first work to scale the shear rate with the escape time scale to produce a universal curve for Electrorheological fluids and weakly flocculated dispersions in general. The physical significance of this new shear rate is simple. Just as $\dot{\gamma}a^2/D \approx O(1)$ marks the transition from diffusion limited to shear dominated dynamics for Brownian hard-spheres, $(\dot{\gamma}a^2/D)(kT/U_{min})\exp(U_{min}/kT) \approx O(1)$ marks the same transition for flocculated dispersions. When $(\dot{\gamma}a^2/D)(kT/U_{min})\exp(U_{min}/kT) \ll 1$, particles hop out of their mutual potential wells and network rearrangement occurs on the hopping time τ.

The concept of the escape time was extended to a general model for the rheology of flocculated suspensions. Following the pioneering work of Glasstone et al. (1941) who formulated a viscosity model for molecular liquids, the model takes a microstructural approach and incorporates the physics of the particle interaction and dynamics to produce a simple and effective, yet general method to model flocculated suspensions. The results are encouraging. With only one adjustable parameter, A_2, the model describes the rheological behavior for not only the model ER suspensions, but also for suspensions with a more complex morphology of aggregates in an isotropically flocculated dispersion, by simulation and by experiments done independently by other

researchers. The model captures the essential physics of the pair interaction potential particularly influencing the suspension dynamics. Future efforts should be directed at determining the effect of the particle volume fraction and network structure on the suspension dynamics and the constant A_2. This will require extensive characterization of the floc structures formed and their evolution under shear.

Finally, this work suggests that the distinction between weakly flocculated suspension and strongly flocculated ones (the border being approximately 20 kT) is an artificial one. Even suspensions with pair potentials well above $20kT$ are expected to flow under small stresses or strains but at exponentially large time scales. These long times scales make observation of the low-shear regime by experiments or by computation using the traditional molecular-dynamic type simulation methods unfeasible. A novel method is needed to explore the low-shear behavior for strongly flocculated suspensions and it is hoped that this work will inspire further investigations into developing such a method.

Bibliography

Adriani, P. M. and Gast, A. P. (1988). A microscopic model of electrorheology. *Phys. Fluids*, 31(10):2757-2768.

Annonymous (1992). Liquid shocks. *Tech. Edge*, October.

Asakura, S. and Oosawa, F. (1954). On interaction between two bodies immersed in a solution of macromolecules. *J. Chem. Phys.*, 22:1255.

Bergenholtz, J. and Wagner, N. J. (1994). The Huggins coefficient for the square-well colloidal fluid. *Ind. Eng. Res.*, 33(10):2391-2397.

Bonnecaze, R. T. (1991). *Macroscopic properties of electrically interacting suspensions.* PhD thesis, The California Institute of Technology.

Bonnecaze, R. T. and Brady, J. F. (1992a). Dynamic simulation of an Electrorheological fluid. *J. Chem. Phys.*, 96:2183.

Bonnecaze, R. T. and Brady, J. F. (1992b). Yield stresses in Electrorheological fluids. *J. Rheol.*, 36(1):73.

Bossis, G. and Brady, J. F. (1987). Self-diffusion of Brownian particles in concentrated suspension under shear. *J. Chem. Phys.*, 87(9):5437-5448.

Bossis, G. and Brady, J. F. (1989). The rheology of Brownian suspensions. *J. Chem. Phys.*, 91(3):1866-1874.

Bossis, G., Mathis, C., Mimouni, Z., and Paparoditis, C. (1990). Magnetoviscosity of micronic suspensions. *Europh. Lett.*, 11(2):133.

Brady, J. F. (1993). The rheological behavior of concentrated colloidal suspensions. *J. Chem. Phys.*, 98 (1):1.

Brady, J. F. (1994). The long-time self-diffusivity in concentrated colloidal suspensions. *J. Fluid Mech.*, 272:109-133.

Brady, J. F. and Vicic, M. (1995). Normal stresses in colloidal dispersions. *J. Rheol.*, 39(3):545.

Buscall, R., Goodwin, J. W., Hawkins, M. W., and Ottewill, R. H. (1982). Viscoelectic properties of concentrated latices. Parts 1 and 2. *J. Chem. Soc. Faraday Trans. 1*, 78:2873.

Buscall, R., McGowan, J. I., and Morton-Jones, A. J. (1993). The rheology of concentrated dispersions of weakly attracting colloidal particles with and without wall slip. *J. Rheol.*, 37(4):621.

Chaffey, C. E. and Porter, R. S. (1985). On the origin of negative normal stresses in sheared or lyotropic liquid crystals. *J. Rheol.*, 29(3):281-305.

Chandrasekhar, S. (1943). Stochastic problems in physics and astronomy. *Rev. Mod. Phys.*, 15:1.

Cichocki, B. and Felderhof, B. U. (1990). Diffusion coefficient and effective viscosity of suspensions of sticky hard spheres with hydrodynamic interactions. *J. Chem. Phys.*, 93(6):4427-4432.

CRC (1990-91). *The CRC Handbook of Chemistry and Physics.* CRC Press.

De Rooij, R., Potanin, A. A., van den Ende, D., and Mellema, J. (1993). Steady shear viscosity of weakly aggregating polystyrene latex dispersions. *J. Chem. Phys.*, 99(11):9213-9223.

Ehrgott, R. C. and Masri, S. F. (1994). Experimental characterization of an electrorheological material subjected to oscillatory shear strains. *J. Vib. & Acoustics*, 116(1):53.

Ferry, J. D. (1980). *Viscoelastic properties of polymers.* Wiley.

Gast, A. P., Hall, K., and Russel, W. B. (1983). Phase separations induced in aqueous colloidal suspensions by dissolved polymer. *Faraday Discuss. Chem. Soc.*, 76:189.

Gast, A. P., Russel, W. B., and Hall, C. K. (1986). An experimental and theoretical-study of phase-transitions in the polystyrene latex and hydroxyethylcellulose system. *J. Coll. Int. Sci.*, 109:161-171.

Gast, A. P. and Zukoski, C. (1989). Electrorheological fluids as colloidal suspensions. *Adv. Coll. Int. Sci.*, 30:153.

Glasstone, S., Laidler, K., and Eyring, H. (1941). *The Theory of Rate Processes.* McGraw-Hill Book Company.

Halsey, T. C., Martin, J. E., and Adolf, D. (1992). Rheology of Electrorheological fluids. *Phy. Rev. Lett.*, 68(10):1519.

Hayter, J. B. and Pynn, R. (1982). Structure factor of a magnetically saturated ferrofluid. *Phys. Rev. Lett*, 49 (15):1103-1106.

Hwang, Y. and Wu, X.-. (1993). Small-angle light scattering study of quasi-two-dimensional structures of magnetic particles. *Coll. & Surfaces A: Physiochemical and Engineering Aspects*, 80:19.

Jeffrey, D. J., Morris, J. F., and Brady, J. F. (1993). The pressure moments for two rigid spheres in low-Reynolds-number flow. *Phys. of Fluids A*, 10:2317-2325.

Klingenberg, D. J., Dierking, D., and Zukoski, C. F. (1991). Stress-transfer mechanisms in Electrorheological suspensions. *J. Chem. Soc. Faraday Trans.*, 87(3):425-430.

Klingenberg, D. J. and Zukoski, C. F. (1990). Studies on the steady-shear behavior of Electrorheological suspensions. *Langmuir*, 6:15-24.

Kramers, H. A. (1940). Brownian motion in a field of force and the diffusion model of chemical reactions. *Physica VII* , 4:284-304.

Kraynik, A., Bonnecaze, R. T., and Brady, J. F. (1991). Electrically induced stresses in er fluids: The role of particle chain structures. In Tao, R., editor, *Electrorheological Fluids.*

Liang, R. and Xu, Y. (1993). Some new evidence on electro-rheological mechanisms. In Tao, R., editor, *4th ER fluids conference proceedings.* Feldkirch, Austria.

Liu, J., Lawrence, E., Ivey, M., Flores, G., Bibette, J., and Richard, J. (1993). Field-induced structure of confined Ferrofluid emulsion. In Tao, R., editor, *4th ER fluids conference proceedings.* Feldkirch, Austria.

Marshall, L., Zukoski, C., and Goodwin, J. W. (1989). Effect of electric fields on the rheology of non-aqueous concentrated suspensions. *J. Chem. Soc. Faraday Trans.*, 85:2785.

Melrose, J. R. (1992). Brownian dynamics simulation of dipole suspensions under shear: The phase diagram. *Molec. Phys.*, 76(3):635.

Melrose, J. R. and Heyes, D. (1993a). Rheology of weakly flocculated suspensions: Simulation of agglomerates under shear. *J. Coll. Int. Sci.*, 157(1):227.

Melrose, J. R. and Heyes, D. M. (1993b). Rheology of weakly flocculated suspensions: simulation of agglomerates under shear. *J. Coll. Int. Sci.*, 157:227-234.

Morris, J. F. (1996). *Suspensions: microstructure, diffusion, and inhomogenous flow.* PhD thesis, The California Institute of Technology.

Phung, T. (1993). *Behavior of concentrated colloidal suspensions by Stokesian dynamics simulation.* PhD thesis, The California Institute of Technology.

Phung, T. N., Brady, J. F., and Bossis, G. (1996). Stokesian Dynamics simulation of Brownian suspensions. *J. Fluid Mech.*, 313:181-207.

Potanin, A. A., R. De Rooij, D. V. d. E., and Mellema, J. (1995). Microrheological modeling of weakly aggregating dispersions. *J. Chem. Phys.*, 102(14):5845-5853.

Russel, W. B. (1984). The huggins coefficient as a means for characterizing suspended particles. *J. Chem. Soc. Faraday Trans.*, 80:31-41.

Russel, W. B., Saville, D. A., and Schowalter., W. (1989). *Colloidal Dispersions.* Cambridge University.

Sun, J. M. and Tao, R. (1995). Viscosity of a one-component polarizable fluid. *Phys. Rev. E*, 52(1):813.

Tanner, R. (1985). *Engineering Rheology.* Clarendon Press, Oxford.

Tao, R. (1993). Electric-field-induced phase transition in Electrorheological fluids. *Phys. Rev. E*, 47(1):423-426.

van der Werff, J. C. and de Kruif, C. G. (1989). Hard-sphere colloidal dispersions: the scaling of rheological properties with particle size, volume fraction, and shear rate. *J. Rheol.*, 33(3):421.

Winslow, W. M. (1949). Induced vibrations of suspensions. *J. Appl. Phy.*, 20:1137.

Xu, B. C. and Hass, K. C. (1993). Liquid-state properties of electrorheological fluids. *J. Chem. Phys.*, 98 (3): 2258.

Appendix A

The low-shear viscosity for dispersed suspensions

The equation governing the N-particle distribution is the Smoluckowski equation,

$$\frac{\partial P_N}{\partial t} + \nabla \cdot \mathbf{j}_N = 0, \tag{A.1}$$

where the probability flux $\mathbf{j}_N$ is given by

$$\mathbf{j}_N = \mathbf{U} P_N + \mathbf{R}_{FU} \cdot (\mathbf{F}^P - kT \nabla \ln P_N)\, P_N, \tag{A.2}$$

and represents, respectively, contributions from convection, the pair potential, and diffusion. Small perturbations to the equilibrium structure are denoted by

$$P_N = P_N^o (1 - f_N), \tag{A.3}$$

and the particle flux becomes

$$\mathbf{j}_N = \mathbf{U} P_N^0 (1 - f_N) - P_N^0 \mathbf{D} \cdot \nabla f_N. \tag{A.4}$$

In order to proceed analytically, an equation for the pair-distribution function P_2 is obtained by integrating over N-2 particles. Following the method of Brady (1993), we obtain to the first order in Pe,

$$P_2^0 \frac{\partial f_2}{\partial t} - \nabla_r \cdot \langle \mathbf{D}_r \rangle_2^o \, P_2^0 \cdot \nabla_r f_2 = -\nabla_r \cdot \langle \mathbf{U}_r \rangle_2^0 \, P_2^0, \tag{A.5}$$

where the angled brackets denote a conditional average with two particles fixed and f_2 is the normalized disturbance, $\langle f_2 \rangle_2^0 = Pe f_2$. We have also neglected direct couplings to a third particle in writing (A.5). The quantities $\langle \mathbf{D}_r \rangle_2^0$ and the $\langle \mathbf{U}_r \rangle_2^0$ are the diffusivity and velocity of the particle pair, respectively. Neglecting all hydrodynamic interactions, and anisotropy, and noting that the scalar function $f_2(r) = -(1/2) f(r) \mathbf{d} \cdot$

$\langle \mathbf{E} \rangle \cdot \mathbf{d}$, where $\mathbf{d}$ is the dimensionless separation vector between particle centers, Equation (A.5) reduces to

$$\frac{1}{g(r)r^2}\frac{d}{dr}\left(gr^2\frac{df}{dr}\right) - \frac{6f}{r^2} = -r\frac{d\ \ln g}{dr}, \tag{A.6}$$

where $g(r)$ is the equilibrium pair-distribution function. For weakly aggregated suspensions the pair-distribution function scales as the exponential of the pair potential,

$$g(r,\theta) = g_{HS}\ \exp\left(\lambda\left(\frac{2a}{r}\right)^3\frac{(3\ \cos^2\theta - 1)}{2}\right), \tag{A.7}$$

for a dilute suspension. Again, for simplicity, we neglect any anisotropy in the structure and the potential, and use the infinite dilution value of 1 for g_{HS} such that

$$g(r,\theta) \approx g(r) \approx \exp\left(\lambda\left(\frac{2a}{r}\right)^3\right). \tag{A.8}$$

Substituting into Equation (A.6), the evolution equation for the pair-perturbation function is

$$\frac{d^2f}{dr^2} + \frac{2}{r}\frac{df}{dr} - \frac{24\lambda}{r^4}\frac{df}{dr} - \frac{6f}{r^2} - \frac{24\lambda}{r^3} = 0, \tag{A.9}$$

with boundary conditions

$$\begin{aligned} f &\sim 0 \quad \text{as} \quad r \to \infty \\ \frac{df}{dr} &= -2 \quad \text{at} \quad r = 2. \end{aligned}$$

The first boundary condition ensures no disturbance far-away, while the second ensures no relative flux at the surface of contact of the two particles.

In the absence of hydrodynamic interactions, there is no contribution to the stress from Brownian motion. The interparticle force, however, is now the sum of a hard

sphere repulsion and the electrostatic force,

$$\mathbf{F}^P = \frac{1}{2}kT\ \mathbf{n}\ \delta(r-2a) + \mathbf{F}^{ER}. \tag{A.10}$$

The hard sphere contribution to the stress $\langle \mathbf{xF} \rangle$ is

$$\begin{aligned} \langle \mathbf{xF} \rangle^{HS} &= -\frac{1}{2}kTn^2 \int \mathbf{nn}\delta(r-2a)g(\mathbf{r})d\mathbf{r}, \\ &= -kTn^2 a \int_{r=2a} \mathbf{nn}\ g(r)d\mathbf{S}, \end{aligned}$$

where $\mathbf{n}$ is the unit vector connecting two particle centers. The viscosity is now a sum of the ER viscosity which, from Equation (71) in Brady (1993), becomes

$$\eta_{ER} = -\frac{27}{5}\lambda\phi^2 \int_2^\infty \frac{1}{r} e^{\frac{8\lambda}{r^3}} f(r)dr, \tag{A.11}$$

with our expression for g(r), and the contribution from the hard-sphere repulsion, which is identical to Equation (53) from Brady (1993),

$$\eta_{HS} = \frac{9}{5}\phi^2 e^{\lambda} f(2), \tag{A.12}$$

where we have substituted Equation (A.8) evaluated at $r = 2a$ for $g(2)$ and the infinite dilution diffusivity for the short-time diffusivity.

Equation (A.9) was solved numerically using a shooting method. The boundary condition for $r \to \infty$ was satisfied on $r = 100a$, and the results for $f(2)$ are displayed in figure A.1. Note that $f(2)$ becomes negative for $\lambda > 2$, such that the hard-sphere contribution is negative while the ER contribution is positive.

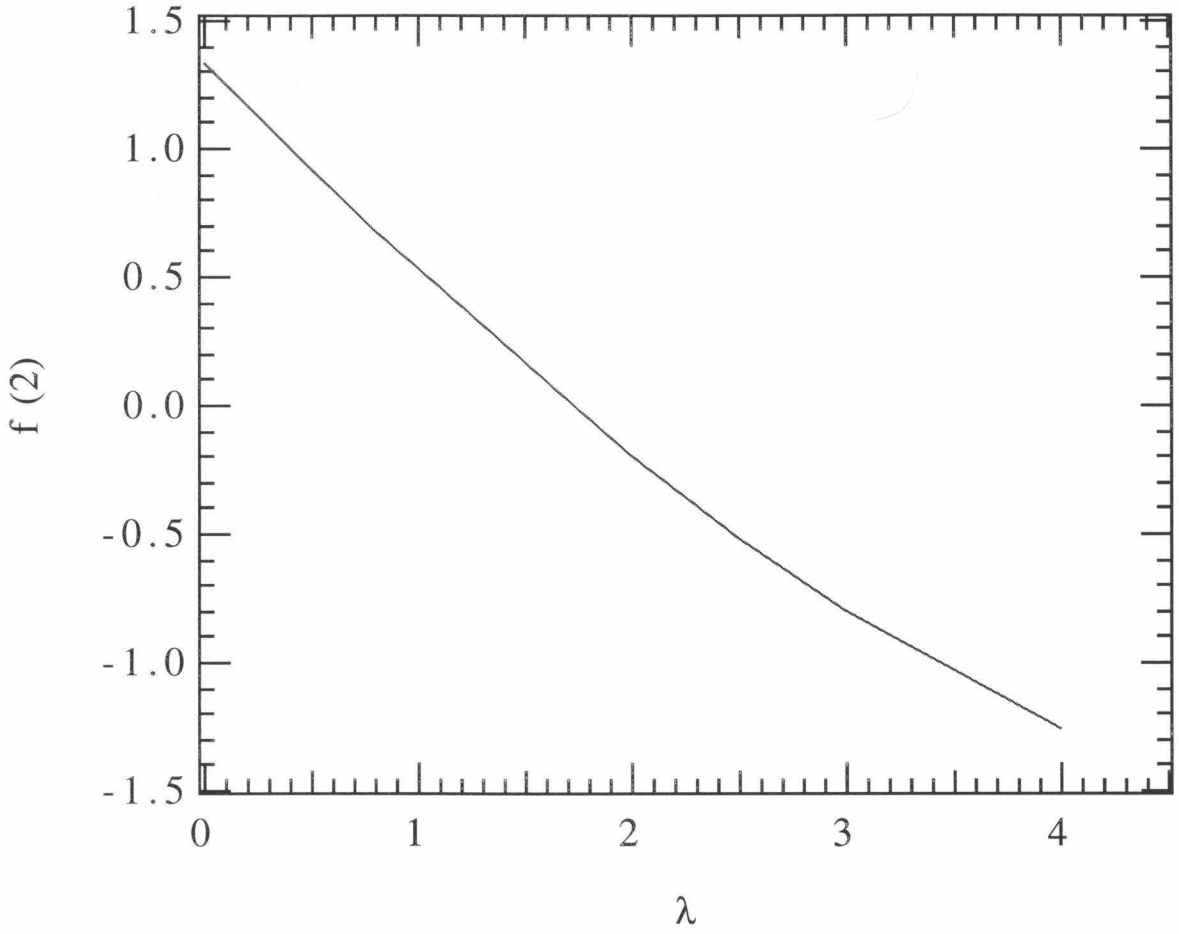

Figure A.1: The disturbance function $f(2)$ as a function of λ. Note that $f(2)$ becomes negative for increasingly attractive potential wells. This suggests an increase in particle density at angular positions where for hard sphere suspensions there was a depletion.

Appendix B

Tables

For completeness the individual components of both the suspension viscosity and first normal stress difference are reported here.

Table B.1: The **xF, SP** and hydrodynamic contributions to the total suspension viscosity for the dispersed regime, $\lambda < 4$. Statistical information is omitted where sampling is insufficient to produce meaningful standard deviations.

λ	Ma	η_H	η_{BR}	η_{XF}	η_{ER}
0.8	0.001	1.3	3.15	-3.76	0.962
	0.01	1.3 ± 0.03	0.6 ± 0.5	-0.5 ± 0.8	0.2 ± 0.3
	0.1	1.3 ± 0.1	0.22 ± 0.4	-0.1 ± 0.3	0.04 ± 0.1
	1.0	1.2 ± 0.08	0.05 ± 0.04	-0.03 ± 0.04	0.01 ± 0.01
1.7	0.0002	1.3 ± 0.1	-1.2 ± 4.1	4.6 ± 4.1	-2.0 ± 0.05
	0.001	1.3	-5.04	9.12	-3.11
	0.01	1.3 ± 0.1	0.07 ± 0.2	-0.16 ± 3.1	0.1 ± 0.2
	0.1	1.5 ± 0.2	0.19 ± 0.2	-0.05 ± 0.1	0.01 ± 0.2
	1.0	1.3 ± 0.06	0.03 ± 0.02	-0.03 ± 0.04	0.02 ± 0.01
2.5	0.0002	1.3	-3.14	9.08	-3.23
	0.001	1.4 ± 0.05	-0.03 ± 2.3	5.2 ± 5.6	-1.6 ± 1.0
	0.005	1.4 ± 3.46	-1.85 ± 4.19	5.2 ± 8.48	-1.2 ± 3.53
	0.01	1.3 ± 1.3	-0.7 ± 2.0	2.5 ± 4.4	-0.033 ± 0.26
	0.1	1.5 ± 0.17	0.08 ± 0.19	0.06 ± 0.14	-0.07 ± 0.14
	1.0	1.3 ± 0.08	0.02 ± 0.02	-0.03 ± 0.04	0.02 ± 0.02
	10	1.3 ± 0.1	0.002 ± 0.002	-0.003 ± 0.005	0.001 ± 0.002
	100	1.3 ± 0.1	0.0001 ± 0.0002	0 ± 0	0 ± 0
3.3	10^{-4}	1.4	-46.3	68.1	-3.8
	0.0002	1.4 ± 0.05	-28.5 ± 26.4	42.8 ± 46.6	-1.1 ± 11.4
	0.001	1.5 ± 0.1	-20.6 ± 7.0	44.8 ± 15.9	-8.1 ± 1.5
	0.005	1.5 ± 0.2	-5.1 ± 4.4	14.7 ± 10.4	-5.0 ± 2.3
	0.01	1.5 ± 0.2	-1.7 ± 0.08	5.5 ± 0.3	-1.9 ± 0.1
	0.1	1.4 ± 0.1	0.009 ± 0.1	0.07 ± 0.3	-0.008 ± 0.2
	1.0	1.3 ± 0.08	0.02 ± 0.01	-0.03 ± 0.05	0.02 ± 0.02
	10	1.3 ± 0.1	0.001 ± 0.001	-0.002 ± 0.004	0.001 ± 0.002
	100	1.2 ± 0.1	-0.0001 ± 0.0002	-0.0002 ± 0.0005	0.0001 ± 0.0003

Table B.2: The **xF, SP** and hydrodynamic contributions to the total suspension viscosity for the equilibrium flocculated regime, $4 < \lambda < 10$. Statistical information is omitted where sampling is insufficient to produce meaningful standard deviations.

λ	Ma	η_H	η_{BR}	η_{XF}	η_{ER}
4.2	$2 \cdot 10^5$	1.7 ± 0.05	-86.3 ± 93.5	421 ± 100	-116 ± 31.4
	10^{-4}	1.7 ± 0.05	-191 ± 27.7	363 ± 57.7	-47.5 ± 8.2
	0.0002	1.7 ± 0.05	-106 ± 19.3	213 ± 32.6	-37.5 ± 4.1
	0.001	1.9 ± 0.05	-39.3 ± 3.3	85.6 ± 4.8	-18.9 ± 2.2
	0.01	1.4 ± 0.1	-0.9 ± 1.2	3.8 ± 4.7	-1.2 ± 2.5
	0.1	1.4 ± 0.1	-0.02 ± 0.1	0.13 ± 0.4	-0.03 ± 0.2
	1.0	1.3 ± 0.1	0.01 ± 0.01	-0.02 ± 0.05	0.02 ± 0.02
	10	1.3 ± 0.1	0.001 ± 0.001	-0.002 ± 0.005	0.001 ± 0.002
	100	1.3 ± 0.1	0.0001 ± 0.0001	-0.0002 ± 0.0005	0.0001 ± 0.0003
5.0	$2 \cdot 10^{-5}$	1.8 ± 0.2	-351 ± 4.5	715 ± 149	-7.8 ± 0.05
	10^{-4}	2.0 ± 0.2	-420 ± 137	529 ± 242	-55.9 ± 45.7
	0.0002	2.0 ± 0.2	-180 ± 17.5	386 ± 65.6	-74.5 ± 29.7
	0.001	1.8 ± 0.2	-40.3 ± 8.5	96.2 ± 8.8	-21.7 ± 3.9
	0.01	1.6 ± 0.2	-2.8 ± 1.6	9.7 ± 3.6	-3.6 ± 1.8
	0.1	1.4 ± 0.1	-0.03 ± 0.06	0.19 ± 0.3	-0.75 ± 0.4
	1.0	1.3 ± 0.08	0.01 ± 0.01	-0.02 ± 0.05	0.02 ± 0.02
	10	1.3 ± 0.1	$0.0007 \pm .001$	-0.002 ± 0.005	0.001 ± 0.003
	100	1.3 ± 0.1	0 ± 0	-0.0002 ± 0.0005	0 ± 0
5.8	$5 \cdot 10^{-6}$	2.0	1300	2400	-1830
	$2 \cdot 10^{-5}$	2.3 ± 0.05	-2100 ± 248	3640 ± 388	-296 ± 4.4
	10^{-4}	2.4 ± 0.1	-652 ± 24.6	1130 ± 39.0	-195 ± 2.7
	0.0002	2.3 ± 0.2	-214 ± 70.0	436 ± 151	-69.7 ± 29.9
	0.001	2.2 ± 0.3	-53.9 ± 15.4	121 ± 30.4	-24.8 ± 7.2
	0.01	1.8 ± 0.3	-2.5 ± 1.5	11.0 ± 4.1	-4.1 ± 1.9
	0.1	1.5 ± 0.1	-0.04 ± 0.12	0.26 ± 0.69	-0.13 ± 0.3
	1.0	1.3 ± 0.09	0.008 ± 0.007	-0.02 ± 0.05	0.01 ± 0.02
	10	1.2 ± 0.1	0.0006 ± 0.0009	-0.002 ± 0.003	0.0009 ± 0.005
	100	1.2 ± 0.1	0 ± 0	-0.0002 ± 0.0005	$0pm0$
8.3	$2 \cdot 10^{-5}$	2.2 ± 0.5	-1420 ± 629	3070 ± 1170	-340 ± 49.0
	10^{-4}	3.2 ± 0.140	-543 ± 221	1070 ± 190	698 ± 373
	0.001	2.7 ± 0.7	-56.5 ± 17.9	126.0 ± 22.0	-27.0 ± 5.60
	0.01	2.5 ± 0	-4.4 ± 0.05	18.3 ± 1.50	-7.2 ± 2.30
	0.1	1.5 ± 0.01	-0.05 ± 0.01	0.42 ± 0.02	-0.24 ± 0.04
	1.0	1.3 ± 0.09	0.005 ± 0.005	-0.02 ± 0.05	0.01 ± 0.02
	10	1.2 ± 0.1	0.0004 ± 0	-0.002 ± 0.005	0.0008 ± 0.003
	100	1.2 ± 0.1	0	0	0

Table B.3: The **xF, SP** and hydrodynamic contributions to the total suspension viscosity for the kinetic flocculated regime, $10 < \lambda$. Statistical information is omitted where sampling is insufficient to produce meaningful standard deviations.

λ	Ma	η_H	η_{BR}	η_{XF}	η_{ER}
17.0	$2 \cdot 10^{-5}$	5.6 ± 1.2	-2350 ± 1110	5620 ± 1550	-1800 ± 541
	10^{-4}	5.1 ± 0.3	-635 ± 83.0	1220 ± 142	-205 ± 93.5
	0.0005	4.4	-95.7	265	-82.0
	0.001	3.9 ± 0.3	-39.2 ± 7.1	113 ± 4.9	-33.9 ± 18.6
	0.005	5.1 ± 1.7	-12.6 ± 6.6	45.1 ± 13.9	-15.7 ± 9.5
	0.05	1.9 ± 0.5	-0.2 ± 0.1	2.3 ± 0.9	-1.4 ± 0.4
	0.5	1.3 ± 0.1	0.003 ± 0.006	-0.017 ± 0.09	0.004 ± 0.05
	1.0	1.3 ± 0.11	0.003 ± 0.003	-0.02 ± 0.026	0.008 ± 0.057
83.0	$2 \cdot 10^{-5}$	11.5 ± 1.0	-1390 ± 93.2	5960 ± 25.7	-2600 ± 190
	10^{-4}	13.7 ± 2.9	-524 ± 77	1650 ± 258	-581 ± 246
	0.001	12.9 ± 1.5	-46.2 ± 4.5	181 ± 13.1	-66.5 ± 8.1
	0.01	5.5 ± 0.1	-1.6 ± 0.03	23.1 ± 1.3	-13.6 ± 0.9
	0.1	1.8 ± 0.2	-0.02 ± 0.003	0.82 ± 0.06	-0.59 ± 0.05
	1.0	1.3 ± 0.24	$3 \cdot 10^{-4} \pm 0.001$	-0.011 ± 0.06	0.004 ± 0.029
830	$2 \cdot 10^{-5}$	39.4 ± 1.9	-671 ± 13.7	906 ± 107	-5900 ± 50.8
	10^{-4}	38.0 ± 0.8	-143 ± 2.6	1930 ± 36.2	-1240 ± 73.0
	0.001	18.0 ± 1.1	-8.83 ± 0.3	217 ± 4.7	-136 ± 5.6
	0.01	9.8 ± 0.8	-0.3 ± 0.04	27.7 ± 3.5	-19.3 ± 2.2
	0.1	2.2 ± 0.1	-0.002 ± 0.001	0.89 ± 0.1	-0.67 ± 0.08
	1.0	1.3 ± 0.1	0 ± 0	0.008 ± 0.002	0.002 ± 0.001
$8.3 \cdot 10^5$	$2 \cdot 10^{-5}$	45.0 ± 23.3	-0.99 ± 0.3	5070 ± 411	-2610 ± 1130
	10^{-4}	84.1 ± 16.8	-0.37 ± 0.07	1880 ± 277	-1260 ± 250
	0.001	38.1 ± 6.6	-0.02 ± 0.004	216 ± 56.9	-130 ± 32.1
	0.01	12.6 ± 2.0	-0.0005 ± 0	27.0 ± 2.2	-20.2 ± 2.2
	0.1	2.5 ± 0.3	0 ± 0	0.64 ± 0.2	-0.59 ± 0.1
	1.0	1.3 ± 0.1	0 ± 0	-0.01 ± 0.02	0.006 ± 0.01
$8.3 \cdot 10^{12}$	$2 \cdot 10^{-5}$	2450 ± 347	0	6240 ± 123	-1430 ± 1840
	10^{-4}	496 ± 36.7	0	1420 ± 108	-755 ± 123
	0.001	125 ± 51.2	0	160 ± 16.1	-91.0 ± 3.7
	0.01	17.9 ± 2.8	0	19.2 ± 2.1	-14.3 ± 1.4
	0.1	2.67 ± 0.8	0	0.63 ± 0.3	-0.55 ± 0.18
	1.0	1.46 ± 0.2	0	-0.02 ± 0.01	0.005 ± 0.007

Table B.4: The **xF, SP** and hydrodynamic contributions to the total suspension first normal stress difference for the dispersed regime, $4 < \lambda$. Statistical information is omitted where sampling is insufficient to produce meaningful standard deviations.

λ	Ma	N_1^H	N_1^{BR}	N_1^{XF}	N_1^{ER}
0.8	0.001	0.019	66.9	-120	92.8
	0.01	-0.011 ± 0.007	5.65 ± 0.57	-12.1 ± 0.6	9.01 ± 0533
	0.1	-0.037 ± 0.013	0.766 ± 0.061	-1.31 ± 0.09	0.950 ± 0.031
	1.0	-0.08 ± 0.19	0.06 ± 0.094	-0.13 ± 0.06	0.09 ± 0.05
1.7	0.0002	-0.025 ± 0.006	456 ± 28	-997 ± 12	711 ± 1
	0.001	-0.063	97.0	-208	140
	0.01	-0.030 ± 0.064	8.00 ± 0.44	-18.5 ± 0.6	13.8 ± 0.2
	0.1	-0.01 ± 0.19	0.433 ± 0.36	-1.12 ± 0.56	1.10 ± 0.34
	1.0	-0.04 ± 0.14	0.05 ± 0.04	-0.121 ± 0.07	0.10 ± 0.05
2.5	0.0002	-0.016 ± 0.039	775 ± 19.1	-1700 ± 28.9	1110 ± 16.3
	0.001	-0.016 ± 0.05	131 ± 10	-310 ± 12	208 ± 4
	0.005	-0.189 ± 0.39	28.9 ± 11.6	-63.3 ± 15.0	41.8 ± 11.6
	0.01	-0.22 ± 0.21	10.7 ± 5.9	-25.8 ± 8.0	17.6 ± 5.7
	0.1	-0.159 ± 0.193	0.687 ± 0.346	-1.69 ± 0.672	1.39 ± 0.450
	1.0	-0.009 ± 0.21	0.047 ± 0.03	-0.13 ± 0.08	0.115 ± 0.06
	10	-0.033 ± 0.2	0.005 ± 0.004	-0.015 ± 0.009	0.013 ± 0.009
	100	-0.076 ± 0.248	0.0004 ± 0.0004	-0.0014 ± 0.0009	0.0013 ± 0.001
3.3	10^{-4}	-0.125	2480	-5040	2860
	0.0002	-0.168 ± 0.164	1280 ± 56.0	-2570 ± 35.0	1440 ± 20.0
	0.001	-0.562 ± 0.245	213 ± 14.0	-454 ± 22.0	276 ± 13.0
	0.005	-0.653 ± 0.54	32.9 ± 14.3	-80.3 ± 22.2	53.2 ± 13.0
	0.01	-0.457 ± 0.32	11.2 ± 4.3	-28.4 ± 6.8	21.5 ± 5.4
	0.1	-0.134 ± 0.18	0.72 ± 0.32	-2.07 ± 0.61	1.57 ± 0.45
	1.0	-0.003 ± 0.25	0.043 ± 0.03	-0.14 ± 0.09	0.13 ± 0.07
	10	-0.093 ± 0.236	0.004 ± 0.002	-0.015 ± 0.009	0.013 ± 0.007
	100	-0.07 ± 0.237	0.0003 ± 0.0003	-0.002 ± 0.001	0.001 ± 0.001

Table B.5: The **xF, SP** and hydrodynamic contributions to the total suspension first normal stress difference for the equilibrium flocculated regime, $4 < \lambda < 10$. Statistical information is omitted where sampling is insufficient to produce meaningful standard deviations.

λ	Ma	N_1^H	N_1^{BR}	N_1^{XF}	N_1^{ER}
4.2	$2 \cdot 10^5$	0.153 ± 0.07	22800 ± 100	-35300 ± 100	14600 ± 300
	10^{-4}	-0.739 ± 0.1	4360 ± 44.0	-6888 ± 100	3080 ± 10.0
	0.0002	-0.827 ± 0.126	2250 ± 10.5	-3480 ± 20.0	1590 ± 58.5
	0.001	-1.30 ± 0.265	312 ± 70.6	-577 ± 87.5	310 ± 46.0
	0.01	-0.269 ± 0.461	8.65 ± 7.94	-29.8 ± 22.3	24.2 ± 27.3
	0.1	-0.17 ± 0.351	0.56 ± 0.057	-2.1 ± 1.82	1.6 ± 0.142
	1.0	-0.056 ± 0.28	0.028 ± 0.024	-0.148 ± 0.173	0.13 ± 0.02
	10.0	-0.055 ± 0.242	0.003 ± 0.002	-0.014 ± 0.010	0.013 ± 0.009
	100.0	-0.072 ± 0.237	0.0003 ± 0.0002	-0.002 ± 0.001	0.001 ± 0.001
5.0	$2 \cdot 10^{-5}$	0.097 ± 0.059	28400 ± 420	-39700 ± 100	15500 ± 250
	10^{-4}	-1.77 ± 0.332	5210 ± 2920	-7410 ± 699	3200 ± 100
	0.0002	-1.61 ± 0.11	2250 ± 300	-3650 ± 186	1680 ± 64.5
	0.001	-1.73 ± 0.426	330 ± 29.4	-673 ± 10.0	362 ± 10.0
	0.01	-0.943 ± 0.49	11.7 ± 5.36	-36.0 ± 36.5	26.9 ± 8.35
	0.1	-0.171 ± 0.24	0.52 ± 1.58	-2.14 ± 0.63	1.75 ± 0.49
	1.0	-0.003 ± 0.259	0.033 ± 0.208	-0.15 ± 0.094	0.13 ± 0.074
	10.0	-0.061 ± 0.243	0.002 ± 0.002	-0.015 ± 0.010	0.013 ± 0.009
	100.0	-0.072 ± 0.237	0.0002 ± 0.0002	-0.002 ± 0.001	0.001 ± 0.001
5.8	$5 \cdot 10^{-6}$	0.157	127000	-168000	61800
	$2 \cdot 10^{-5}$	-2.03 ± 0.235	29400 ± 400	-40000 ± 200	15300 ± 100
	10^{-4}	-3.02 ± 0.185	4930 ± 140	-7530 ± 200	3610 ± 60
	0.0002	-2.07 ± 0.681	2390 ± 300	-3680 ± 50	1590 ± 160
	0.001	-2.52 ± 0.848	308 ± 44	-638 ± 47.0	354 ± 39.0
	0.01	-1.15 ± 0.58	11.4 ± 5.1	-37.3 ± 10.4	28.3 ± 7.5
	0.1	-0.202 ± 0.2	0.492 ± 0.18	-2.25 ± 0.53	1.89 ± 0.48
	1.0	-0.008 ± 0.27	0.029 ± 0.019	-0.15 ± 0.094	0.14 ± 0.076
	10.0	-0.065 ± 0.242	0.002 ± 0.002	-0.015 ± 0.010	0.013 ± 0.009
	100.0	-0.072 ± 0.237	0.0002 ± 0.0002	-0.002 ± 0.001	0.001 ± 0.001
8.3	$2 \cdot 10^{-5}$	-2.01 ± 1.34	30700 ± 1940	-42000 ± 2400	16000 ± 1050
	10^{-4}	-3.58 ± 1.50	4713 ± 371	-8320 ± 225	3990 ± 64.0
	0.001	-3.76 ± 0.633	309 ± 15.0	-620 ± 50.0	362 ± 25.0
	0.01	-2.11 ± 0.045	11.8 ± 0.350	-41.2 ± 1.05	33.6 ± 0.05
	0.1	-0.285 ± 0.009	0.352 ± 0.027	-2.24 ± 0.015	2.01 ± 0.005
	1.0	-0.025 ± 0.26	0.02 ± 0.013	-0.15 ± 0.10	0.14 ± 0.082
	10.0	-0.075 ± 0.245	0.002 ± 0.0001	-0.015 ± 0.010	0.013 ± 0.009
	100.0	-0.071 ± 0.237	0.0001 ± 0.0002	-0.002 ± 0.001	0.001 ± 0.001

Table B.6: The **xF, SP** and hydrodynamic contributions to the total suspension first normal stress difference for the kinetic flocculated regime, $\lambda > 10$. Statistical information is omitted where sampling is insufficient to produce meaningful standard deviations.

λ	Ma	N_1^H	N_1^{BR}	N_1^{XF}	N_1^{ER}
17.0	$2 \cdot 10^{-5}$	-4.63 ± 1.5	18500 ± 635	-34800 ± 3810	23100 ± 1290
	10^{-4}	-6.54 ± 1.7	3840 ± 355	-6850 ± 723	3420 ± 702
	0.0005	-5.06	553	-1420	870
	0.001	-3.92 ± 1.0	259 ± 12.0	-611 ± 38	386 ± 67
	0.005	-4.89 ± 0.5	26.2 ± 2.4	-88.0 ± 1.0	78.2 ± 5.5
	0.05	-0.724 ± 0.438	0.531 ± 0.168	-3.99 ± 1.54	4.77 ± 1.27
	0.5	-0.077 ± 0.303	0.024 ± 0.016	-0.314 ± 0.165	0.310 ± 0.141
	1.0	-0.061 ± 0.31	0.009 ± 0.008	-0.152 ± 0.01	0.140 ± 0.009
83.0	$2 \cdot 10^{-5}$	-11.7 ± 0.75	9200 ± 200	-36400 ± 2760	31700 ± 445
	10^{-4}	-21.9 ± 0.7	1870 ± 75	-6500 ± 200	5370 ± 300
	0.001	-18.4 ± 0.89	145 ± 2	-600 ± 19	510 ± 6
	0.01	-4.89 ± 0.37	2.39 ± 0	-40.1 ± 0.7	45.1 ± 1.4
	0.1	-0.384 ± 0.08	0.04 ± 0.014	-1.67 ± 0	2.18 ± 0.09
	1.0	-0.121 ± 0.218	0.002 ± 0.001	-0.162 ± 0.804	0.142 ± 1.15
830	$2 \cdot 10^{-5}$	-41.4 ± 5.3	3260 ± 757	-32800 ± 1260	33000 ± 3400
	10^{-4}	-53.8 ± 9.7	663 ± 20	-7000 ± 790	6630 ± 170
	0.001	-38.9 ± 0.2	34.5 ± 0.9	-653 ± 5	649 ± 9
	0.01	-8.83 ± 1.48	0.428 ± 0.08	-32.7 ± 1.3	45.2 ± 1.5
	0.1	-0.256 ± 0.372	0.004 ± 0.003	-1.67 ± 0.719	2.25 ± 0.737
	1.0	-0.126 ± 0.008	-0.0002 ± 0	-0.167 ± 0.01	-0.144 ± 0.014
8.3 $\cdot 10^5$	$2 \cdot 10^{-5}$	-71.0 ± 2.5	4.45 ± 0.16	-35100 ± 1780	32400 ± 4210
	10^{-4}	-123 ± 23.5	1.34 ± 0.38	-6596 ± 235	7260 ± 93.9
	0.001	-69.7 ± 12.9	0.06 ± 0.02	-627 ± 32.7	671 ± 21.9
	0.01	-11.5 ± 2.1	0.0004 ± 0	-35.4 ± 3.9	48.5 ± 3.25
	0.1	-0.595 ± 0.331	0 ± 0	-1.69 ± 0.41	2.21 ± 0.51
	1.0	-0.169 ± 0.236	0 ± 0	-0.103 ± 0.049	0.102 ± 0.051
8.3 $\cdot 10^{12}$	$2 \cdot 10^{-5}$	-4050 ± 33	0	-25300 ± 90	22800 ± 4580
	10^{-4}	-680 ± 125	0	-4900 ± 158	5130 ± 175
	0.001	-330 ± 221	0	-483 ± 38	581 ± 28
	0.01	-8.98 ± 4.92	0	-32.8 ± 7.1	42.5 ± 5.0
	0.1	-0.816 ± 0.662	0	-1.82 ± 0.576	1.65 ± 0.876
	1.0	-0.306 ± 0.182	0	-0.132 ± 0.053	-0.098 ± 0.022